Upconversion nanoparticles: Shining a new light for ultrasensitive bioanalytical assays

DISSERTATION ZUR ERLANGUNG DES DOKTORGRADES
DER NATURWISSENSCHAFTEN (DR. RER. NAT.)
AN DER FAKULTÄT FÜR CHEMIE UND PHARMAZIE
DER UNIVERSITÄT REGENSBURG

vorgelegt von

Julian Christian Brandmeier

aus Deggendorf

im Oktober 2024

Promotionsgesuch eingereicht am: 09.10.2024

Die Arbeit entstand in der Zeit von Dezember 2020 bis August 2024 am Institut für Biochemie an der Masaryk Universität in Brünn und dem Institut für Analytische Chemie, Chemo- und Biosensorik an der Universität Regensburg.

Die Arbeit wurde angeleitet von: Assoc. Prof. Dr. Hans-Heiner Gorris

Prüfungsausschuss:

Vorsitzender: Prof. Dr. Oliver Tepner
Erstgutachter: Assoc. Prof. Dr. Hans-Heiner Gorris
Zweitgutachter: Prof. Dr. Joachim Wegener
Drittprüfer: Dr. Thomas Hirsch

Table of contents

1 Abbreviations

AP	alkaline phosphatase
AuNP	gold nanoparticle
BGG	bovine γ-globulin
BSA	bovine serum albumin
CCD	charge-coupled device
CEA	carcinoembryonic antigen
CPS	counts per second
CV	coefficient of variation
DLS	dynamic light scattering
DMF	dimethylformamide
EDC	1-ethyl-3-(3-dimethylaminopropyl)carbodiimide
EDTA	ethylene diamine tetraacetic acid
ELISA	enzyme-linked immunosorbent assay
ESA	excited state absorption
ETU	energy transfer upconversion
Fab	antigen-binding fragment of an antibody
FPIA	fluorescence polarization immunoassay
FRET	Förster resonance energy transfer
HEPES	4-(2-hydroxyethyl)piperazine-1-ethanesulfonic acid
HRP	horseradish peroxidase
Ig	immunoglobulin
LFA	lateral flow assay
LOD	limit of detection
mAb	monoclonal antibody
MES	sodium 2-(*N*-morpholino)ethanesulfonate
MIP	molecularly imprinted polymer
MWCO	molecular weight cut-off

NA	numerical aperture
NHS	*N*-hydroxysuccinimide
NIR	near-infrared
NTA	nanoparticle tracking analysis
pAb	polyclonal antibody
PAA	polyacrylic acid
PBS	phosphate-buffered saline
PCR	polymerase chain reaction
PEG	polyethylene glycol
PSA	prostate-specific antigen
PVA	poly(vinyl alcohol)
QD	quantum dot
QY	quantum yield
RT	room temperature
SA	streptavidin
SB	SuperBlock
SELEX	systematic evolution of ligands by exponential enrichment
SERS	surface-enhanced Raman spectroscopy
Simoa	single-molecule array platform
SPR	surface plasmon resonance
scFv	single-chain fragment variable antibody fragment
TBS	Tris-buffered saline
TEM	transmission electron microscopy
TIRF	total internal reflection microscopy
TMB	tetramethylbenzidine
UCNP	photon-upconversion nanoparticle
ULISA	upconversion-linked immunosorbent assay

2 Declaration of collaborations

According to § 8 Abs. 1 Satz 2 Ziff. 7 of the “Ordnung zum Erwerb des akademischen Grades eines Doktors der Naturwissenschaften (Dr. rer. nat.) an der Universität Regensburg vom 18. Juni 2009”, the following paragraph states the collaborations for the experimental and theoretical results presented in this thesis.

Article I: Effect of particle size and surface chemistry of photon upconversion nanoparticles on analog and digital immunoassays for cardiac troponin

Julian C. Brandmeier, Kirsti Raiko, Zdeněk Farka, Riikka Peltomaa, Matthias J. Mickert, Antonín Hlaváček, Petr Skládal, Tero Soukka, and Hans H. Gorris

J.C. Brandmeier and Dr. K. Raiko contributed equally to the article. The experiments were planned and conducted by J.C. Brandmeier and Dr. K. Raiko under the supervision of Assoc. Prof. Dr. H.-H. Gorris and Prof. Dr. T. Soukka. J.C. Brandmeier conducted the digital and analog readouts, all assays using SA-PEG modified UCNPs and their surface modification. The surface modification of UCNPs with PAA followed by the characterization was done by Dr. K. Raiko. Nanoparticle surface modification with Alkyne-PEG-Neridronate followed by a copper catalyzed click reaction with streptavidin azide was done by J.C. Brandmeier. Data evaluation and immunoassays were done by J.C. Brandmeier, Dr. K. Raiko, Assoc. Prof. Dr. Z. Farka, Dr. R. Peltomaa and, Dr. M.J. Mickert. Nanoparticle synthesis for the further modification with Alk-PEG-Ner was done by Dr. A. Hlaváček. All authors revised the manuscript and illustrations, Assoc. Prof.. Dr. H.-H. Gorris was the corresponding author.

Article II: Digital and analog detection of SARS-CoV-2 nucleocapsid protein via an upconversion-linked immunosorbent assay

Julian C. Brandmeier, Natalia Jurga, Tomasz Grzyb, Antonín Hlaváček, Radka Obořilová, Petr Skládal, Zdeněk Farka, and Hans H. Gorris

J.C. Brandmeier and Dr. N. Jurga contributed equally to the article. The experiments were planned und conducted by J.C. Brandmeier and Dr. N. Jurga under the supervision of Assoc. Prof. Dr. H.-H. Gorris and Prof. Dr. T. Grzyb. The digital readout was done by J.C. Brandmeier. Illustrations were done by J.C. Brandmeier. Upconversion-linked immunosorbent assays were optimized, conducted, and evaluated by J.C. Brandmeier and Dr. N. Jurga. Surface plasmon resonance measurements were done by R. Obořilová at CEITEC MU in Brno. Nanoparticle synthesis was done by Dr. A. Hlaváček. All authors revised the manuscript and Assoc. Prof. Dr. H.-H. Gorris was the corresponding author.

Article III: Upconversion-linked branched DNA hybridization assay for the detection of bacteriophage M13

Julian C. Brandmeier, Saara Kuusinen, Zdeněk Farka, Tero Soukka, Hans H. Gorris

J.C. Brandmeier is the first author of the article. The experiments were planned and designed by J.C. Brandmeier and conducted by J.C. Brandmeier and S. Kuusinen under the supervision of Assoc. Prof. Dr. H.-H. Gorris and Prof. Dr. T. Soukka. The nanoparticle surface modification was done by J.C. Brandmeier, nanoparticle synthesis was done by Dr. A. Hlaváček. Assays were conducted, evaluated, and optimized by J.C. Brandmeier and S. Kuusinen with the help of Assoc. Prof. Dr. Z. Farka. All authors revised the manuscript and Assoc. Prof. Dr. H.-H. Gorris was the corresponding author.

3 Curriculum Vitae

List of publications

1. **Brandmeier, J.C**., Kuusinen, S., Farka Z., Soukka, T., Gorris HH. Upconversion-linked branched DNA hybridization assay for the detection of bacteriophage M13. *Adv. Optical Mater*. **2024**, 2402041.
2. Sklenárová, D., Hlaváček, A., Křivánková, J., **Brandmeier, J.C.**, Weisová, J., Řiháček, M., Gorris, H.H., Skládal, P., Farka, Z. Single-molecule microfluidic assay for prostate-specific antigen based on magnetic beads and upconversion nanoparticles. *Lab Chip.* **2024,** *24*, 3536.
3. Farka, Z., **Brandmeier, J.C**., Mickert, M.J., Pastucha, M., Lacina, K., Skládal, P., Soukka, T., Gorris, H.H. Nanoparticle-Based Bioaffinity Assays: From the Research Laboratory to the Market. *Adv. Mater*. **2024**, *36*, e2307653.
4. Hosseinifard, M., Jurga, N., **Brandmeier, J.C.**, Farka, Z., Hlaváček, A., Gorris, H.H., Grzyb, T., Ekner-Grzyb, A. Influence of surface modification and size of lanthanide-doped upconverting nanoparticles on wheat seedlings. *Chemosphere*. **2024**, *347*, 140629.
5. Drozdowski, A., Jurga, N., Przybylska, D., **Brandmeier, J.C.**, Farka, Z., Gorris, H.H., Grzyb, T. Bright photon upconversion in $LiYbF_4$:Tm^{3+}@$LiYF_4$ nanoparticles and their application for singlet oxygen generation and in immunoassay for SARS-CoV-2 nucleoprotein. *J. Colloid. Interface Sci*. **2023**, *649*, 49.
6. **Brandmeier, J.C.**, Jurga, N., Grzyb, T., Hlaváček, A., Obořilová, R., Skládal, P., Farka, Z., Gorris, H.H. Digital and analog detection of SARS-CoV-2 nucleocapsid protein via an upconversion-linked immunosorbent assay. *Anal. Chem*. **2023**, *95*, 4753.
7. Makhneva, E., Sklenárová, D., **Brandmeier, J.C.**, Hlaváček, A., Gorris, H.H., Skládal, P., Farka, Z. Influence of label and solid support on the performance of heterogeneous immunoassays. *Anal. Chem*. **2022**, *94*, 16376.
8. Shapoval, O., **Brandmeier, J.C.**, Nahorniak, M., Oleksa, V., Makhneva, E., Gorris, H.H., Farka, Z., Horák, D. PMVEMA-coated upconverting nanoparticles for upconversion-linked immunoassay of cardiac troponin. *Talanta*. **2022**, *244*, 123400.Cite Share

9. Hlaváček, A., Farka, Z., Mickert, M.J., Kostiv, U., **Brandmeier, J.C.**, Horák, D., Skládal, P., Foret, F., Gorris, H.H. Bioconjugates of photon-upconversion nanoparticles for cancer biomarker detection and imaging. *Nat. Protoc*. **2022**, *17*, 1028.
10. **Brandmeier, J.C.**, Raiko, K., Farka, Z., Peltomaa, R., Mickert, M.J., Hlaváček, A., Skládal, P., Soukka, T., Gorris, H.H. Effect of particle size and surface chemistry of photon-upconversion nanoparticles on analog and digital immunoassays for cardiac troponin. *Adv. Healthc. Mater*. **2021**, *10*, e2100506.
11. Pořízka, P., Vytisková, K., Obořilová, R., Pastucha, M., Gábriš, I., **Brandmeier, J.C.**, Modlitbová, P., Gorris, H.H., Novotný, K., Skládal, P., Kaiser, J., Farka, Z. Laser-induced breakdown spectroscopy as a readout method for immunocytochemistry with upconversion nanoparticles. *Microchim. Acta*. **2021**, *188*, 147.
12. Peltomaa, R., Farka, Z., Mickert, M.J., **Brandmeier, J.C.**, Pastucha, M., Hlaváček, A., Martínez-Orts, M., Canales, Á., Skládal, P., Benito-Peña, E., Moreno-Bondi, M.C., Gorris, H.H. Competitive upconversion-linked immunoassay using peptide mimetics for the detection of the mycotoxin zearalenone. *Biosens. Bioelectron*. **2020**, *170*, 112683.

List of attended conferences:

1. **Brandmeier, J.C.**, Raiko, K., Farka, Z., Peltomaa, R., Mickert, M. J., Hlaváček, A., Skládal, P., Soukka, T., Gorris, H.H. Highly sensitive immunoassay for human cardiac troponin based on photon-upconversion nanoparticles. Oral presentation at UPCONline 2021.
2. **Brandmeier, J.C.**, Jurga, N., Grzyb, T., Hlaváček, A., Obořilová, R., Skládal, P., Farka, Z., Gorris, H.H. Digital and analog upconversion-linked immunosorbent assay for the detection of SARS-CoV-2. Oral presentation ANAKON conference, Vienna, Austria, 2023.
3. **Brandmeier, J.C.**, Jurga, N., Grzyb, T., Hlaváček, A., Obořilová, R., Skládal, P., Farka, Z., Gorris, H.H. Digital and analog upconversion-linked immunosorbent assay for the detection of SARS-CoV-2. Oral presentation at UPCON conference, Montréal, Canada, 2024.

4 Fundamentals

4.1 Introduction

In the realm of diagnostics, sensitive and specific tests allow the detection of clinically important biomarkers, infections, viruses, bacteria, and many other targets. Since the introduction of immunoassays in the 1950s,[1] these biochemical assays have become one of the foundational tools in modern medicine. The development of diagnostic assays has revolutionized healthcare and other disciplines, such as environmental and food safety, by enabling early detection of analytes at low concentrations in complex sample materials, personalized treatment, and disease control. For example, as the Covid-19 pandemic demonstrated, timely and accurate testing helped to identify and isolate infected individuals, preventing further spreading of the virus.[2]

The variety of immunoassays and other bioanalytical tests is remarkable. The last decades have introduced more and more highly accurate, fast, and specific methods that enable better diagnostics. As the methods have become more sensitive, even minute concentrations of the target can be measured, creating a whole new world for novel biomarkers. Ultrasensitive assays can diagnose diseases earlier, allowing for timely intervention and better outcomes. The first immunoassays relied on radioactive labels, such as iodine 125.[3] However, due to safety and stability issues, other labelling systems soon replaced them. Common alternatives include enzymes, fluorescent dyes, luminescent proteins, and nanoparticles. In particular, nanoparticles, have many attractive properties as optical and catalytic labels in bioanalytical applications. The significant progress in the field has enabled the development of ultrasensitive assays and biosensors.[4–9] Due to their small size and unique optical properties, nanoparticles have been established as an attractive alternative for traditional labels enabling detection of analytes at low concentrations.[10] Compared to other nanoparticles used as optical labels, upconversion nanoparticles (UCNPs) have unorthodox optical properties. They can convert the near-infrared (NIR) excitation light into shorter wavelength emission, which grants these nanoparticles numerous advantages, most notably the lack of interference by autofluorescence.[11]

To date, the development of ultrasensitive immunoassays has gained significant attention in the field. Ultimately, enhancing the sensitivity leads to the emergence of digital assays based on counting single molecules. More and more sophisticated systems have been introduced for the detection of various analytes, including cancer markers and toxins.[12] The aim of this thesis was the development of highly sensitive (immuno)assays exploring different assay formats and readout methods for a variety of analytes while taking advantage of the unique properties of UCNPs as optical labels.

The first part of this work describes the fundamental concepts for developing ultrasensitive immunoassays. First the general definitions of immunoassays and different formats are discussed briefly, followed by setting the particular focus to describe various recognition elements together with different label technologies and readout modes, the cornerstone for creating a highly sensitive assay. The main focus is on immunoassays using antibodies as recognition elements, but it should be noted that many fundamental concepts can be also applied to other types of bioanalytical assays using other biorecognition elements. This thesis is based on three original published papers that describe the use upconversion nanoparticles as labels for ultrasensitive detection.

4.2 Bioaffinity assays

4.2.1 Heterogeneous and homogeneous assays

Bioaffinity assays are biochemical tests that are able to detect or quantify the target analyte in a sample. The detection is based on the exceptional ability of antibodies or other affinity binders to bind specifically their target antigen. Moreover, these assays require a means to transform the target binding to a measurable signal. This is often achieved by labelling one of the assay components, known as the tracer, for example, with an optical label that can be measured and quantified. The label alone cannot indicate whether the recognition element is bound to the analyte or not. Therefore, in heterogeneous immunoassay, one of the assay components is bound to a solid phase so the unbound tracers can be washed away. Traditional heterogeneous immunoassays in sandwich format are based on two antibodies: one of them, known as the capture antibody, is immobilized on, for example, a microtiter plate or magnetic beads, and the second antibody, known as the tracer or detection antibody, is labelled, and can be measured. Thus, the amount of the tracer is directly proportional to the amount of the target analyte in the sample (**Figure 1**). Heterogeneous assays are the most commonly used assay format, but they often suffer from long incubation times, and the antibody binding might be altered when immobilized on the surface.[13]

Conversely, while heterogeneous assays rely on a signal change upon analyte binding based on a washing step, homogeneous assays do not require separation of the unbound label, but the assay is based on tracers that generate a measurable change in the signal when the antibody, or other recognition element, is bound to the analyte (**Figure 1**). Such technologies include, for example, Förster resonance energy transfer (FRET) assay and fluorescence polarization immunoassay (FPIA). Homogeneous assays are usually fast and straightforward to perform since often simple mixing and measuring is sufficient, but they are inherently susceptible to interference from real sample matrix, for example, serum or plasma.[13–15]

4.2.2 Competitive and non-competitive assays

The above-mentioned sandwich immunoassay is a traditional example of a heterogeneous non-competitive assay. Non-competitive assays are often very sensitive and specific to detect the analyte even at very low concentrations. Such a format, however, requires that two antibodies, or other recognition elements, are capable of binding to the target analyte simultaneously, which is often not possible with small analytes that consist of a single epitope.[16] Therefore, assays for small molecules are usually based on the competitive format (**Figure 1**). In the competitive assay, the target analyte, or its analogue, known as the competitor, is labelled or immobilized on the solid surface, followed by a competition between the analyte and the competitor for the binding to the recognition element. If no analyte is present, all binding sites are occupied by the competitor, resulting in high signals. If a high concentration of the analyte is present, low signals are measured since the analyte, rather than the competitor, occupies the binding sites, resulting in low signal. Therefore, the signal in competitive assays is usually conversely proportional to the analyte concentration.[17]

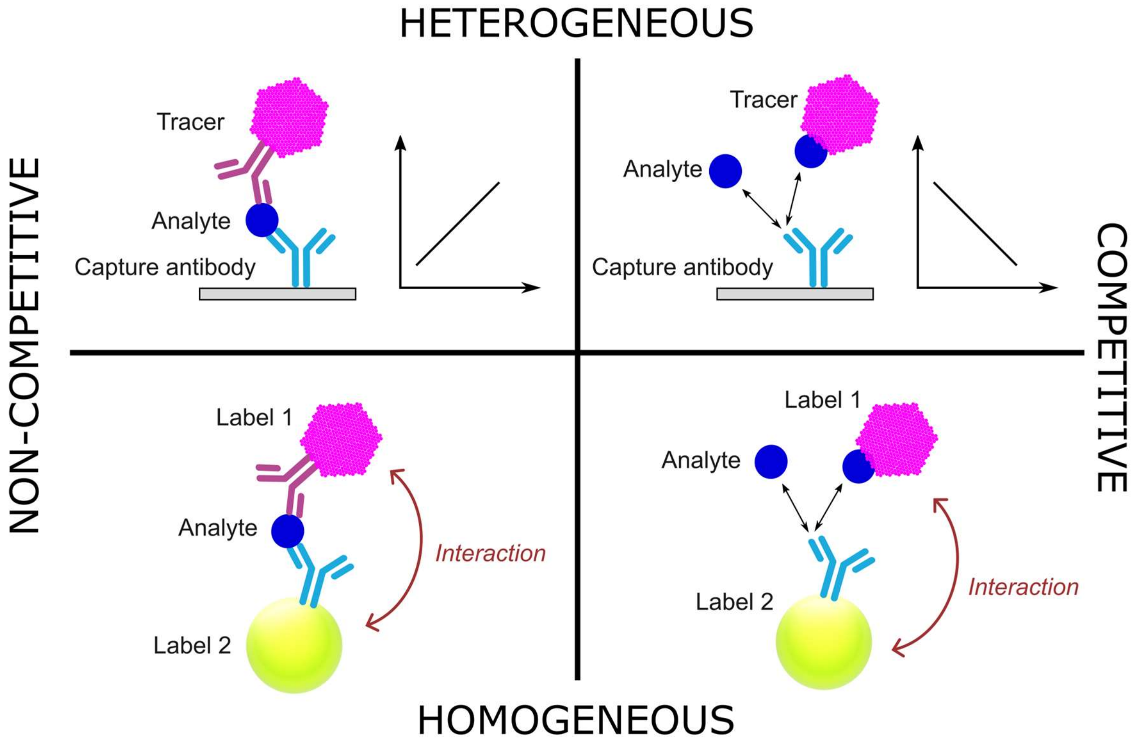

Figure 1. *Scheme of different assay formats. Immunoassays, as well as other bioanalytical assay which might use alternative recognition elements than antibodies, can be classified into heterogeneous and homogeneous assays. On the other hand, the assays can be categorized as competitive or non-competitive depending whether the analyte binding is measured directly or based on competition.*

4.3 Analogue and digital readout formats

4.3.1 Analogue readout

Conventional bioanalytical assays are based on an analogue readout which refers to measuring a continuous signal, such as changes in colour, fluorescence, or luminescence. Typical examples include colorimetric enzyme-linked immunosorbent assays (ELISA) and lateral flow tests, for example, the SARS-CoV-2 antigen tests or pregnancy tests, where the presence of the analyte is based on a colour change that can be observed even by the naked eye. Similarly, in colorimetric ELISAs the colour change caused by the accumulation of the colourful enzymatic product can be seen by the eye.[15] More commonly, especially when a quantitative result is needed, the signal is measured with an appropriate detector. The optical readout can be, for example, a spectrophotometer in the case of colorimetric ELISA or a fluorometer when the assay uses fluorescent dyes. These detectors measure the total signal of the assay, that is absorbance or fluorescence of the microtiter plate wells where the assay is performed, therefore they use an analogue readout (**Figure 2A**). [18]

The sensitivity of the analogue readout method is strongly limited by the signal intensity as well as the amount of background signal or noise of the measurement method or the device. Especially the background and the noise can only be reduced to a certain point which comes often at the expense of an increased complexity but can never be eliminated completely. Analogue assays are usually performed in relatively large reaction volumes to achieve the necessary sensitivity and signal intensity for their respective readouts.[19,20]

4.3.2 Digital readout

A digital readout, on the other hand, is usually performed in such a way that the detection occurs in a large quantity of reaction chambers, each of extremely small volume. Additionally, the reactants, usually the target analyte and the label, are highly diluted. With this combination of a high amount of small-volume reaction chambers and highly diluted samples, each chamber contains either no analyte molecules ("0") or exactly one analyte molecule ("1"), resulting in a binary outcome, hence the term “digital readout” (**Figure 2B**). This is often achieved through techniques such as single molecule counting or digital ELISA. In these methods, single target molecules are isolated and individually analysed, significantly reducing background noise and enhancing signal clarity. By counting the proportion of positive outcomes and combining them with the Poisson distribution, the absolute concentration of target molecules can be obtained.[21]

In the digital ELISA, individual target molecules are captured on magnetic beads or within a microfluidic chamber, followed by labelling them with specific antibodies conjugated to signal-generating enzymes. Each binding event produces a discrete countable signal, such as a fluorescent or chemiluminescent spot, which can be detected and quantified using high-resolution imaging systems or digital counters. This method can massively improve the analytical sensitivity, allowing the detection of low-abundance biomarkers that are often undetectable with traditional analogue assays. The benefits of digital immunoassays include exceptional analytical sensitivity, improved signal-to-background ratio, and the ability to perform absolute quantification without the need for calibration curves. Furthermore, the digital nature of the data facilitates straightforward statistical analysis and reproducibility. By isolating and analysing single molecules, digital assays reduce the impact of sample variability and heterogeneity resulting in more reliable and accurate results. These attributes make digital assays particularly advantageous for applications in clinical diagnostics, biomarker discovery, and personalized medicine, where precise quantification and early detection are paramount. A further benefit is the reduced reagent consumption and smaller sample volumes, aligning with the principles of cost-effectiveness and sustainability in laboratory practices.[22][21][18][23][24]

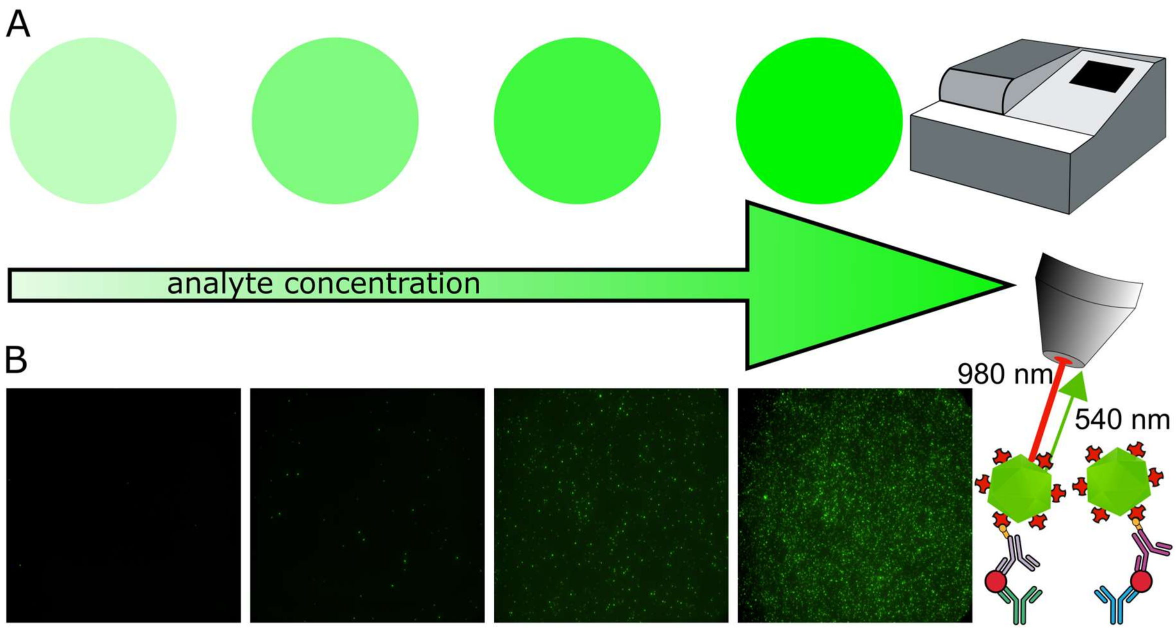

***Figure 2**. Scheme of analogue and digital readouts. (A) In the analogue readout, the measurement is based on an integrated signal over a specific area using, for example, common microplate readers. In contrast, (B) the digital readout is based on detection individual binding events, such as a fluorescent spot, which can be measured using high-resolution imaging systems.*

The most popular and widely adopted digital immunoassay is the digital ELISA based on the single-molecule array platform (Simoa), developed by the David Walt research group and commercialized by Quanterix company.[25] In this method, magnetic beads conjugated with antibodies specific to the target analyte are added to the sample, where they bind the target. Subsequently, detection antibodies labelled with an enzyme are added, forming a sandwich complex comprising of magnetic bead antibody conjugate, the target analyte, and the labelled detection antibody (**Figure 3**). The concentration ratios of magnetic beads to analyte and detection antibody to analyte are adjusted to ensure that each magnetic bead contains either a single sandwich immune complex or none. The sandwich immune complexes are then loaded into an array of femtoliter-sized wells (Simoa disc), each well having a diameter and volume large enough to accommodate exactly one magnetic bead sandwich complex. For the signal generation, the enzyme substrate is added and the femtoliter-sized wells are sealed. The enzyme then converts the substrate into a fluorescent product while the sealing prevents the product from leaking into neighbouring wells. Due to the enzymatic signal amplification, a high local concentration of fluorescent product is generated in each well containing an immune complex. A highly sensitive charge-coupled device (CCD) camera integrated with a microscope setup is required to detect the fluorescent signals. This method allows for remarkable signal amplification, enabling the detection of extremely low analyte concentrations with high sensitivity.[26] [27] [28] [29]

The constant need for ultrasensitive detection has also lead to the development of many other digital detection technologies, such as digital polymerase chain reaction (dPCR), nanostring or nanowire field effect transistor (NW-FET), solid-state nanopores,[30,31] as well as photonic crystal-based biosensors.[22,32] At the heart of such digital assays lies the ability to detect the signal resulting from a single analyte molecule with high precision and therefore sensitive imaging platforms are needed.

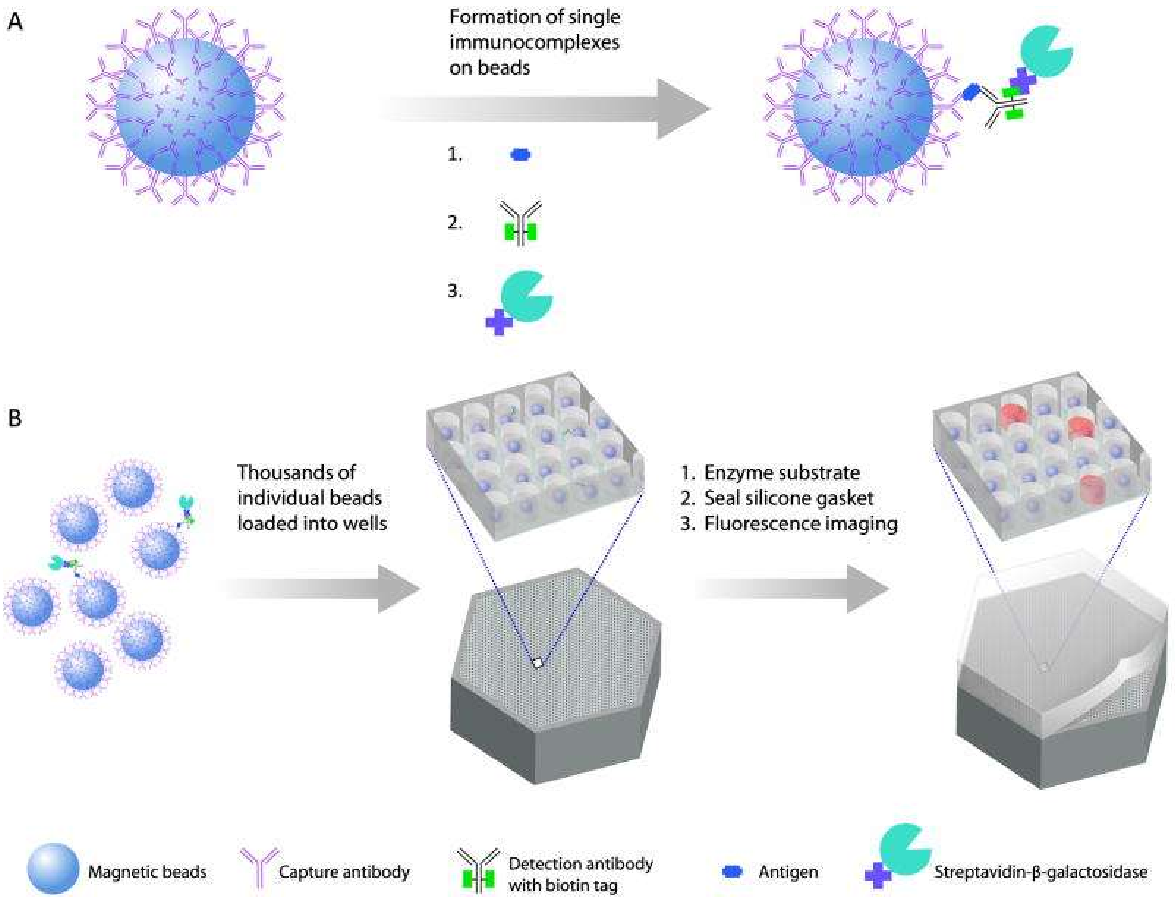

Figure 3. *Principle of the SIMOA assay. (A) Immune complexes are formed on the beads which are then loaded into (b) the femtoliter wells. After adding the substrate and sealing the wells, individual positive and negative beads are detected by fluorescence imaging. Reprinted with permission from Rissin et al. 2010.[33] Copyright 2010 Springer Nature.*

4.3.3 Microscopy imaging for digital readout

The resolution of an imaging device is defined by its ability to reproduce object details, specifically to distinguish two individual objects as separate entities. Essentially, resolution is the smallest distance between two points that can still be distinguished from one another. Two main factors limiting the resolution in microscopy, one is the numerical aperture (NA) of the objective lens and the diffraction limit of light. The *NA* of an objective lens is defined as:

$$NA = n \cdot sin(\theta)$$

where *n* represents the refractive index of the medium between the objective and the sample (e.g., air, water, oil) and θ is the half-angle of the maximum cone of light entering the lens. In contrast to the numerical aperture of the objective, which is limited by the available hardware, the diffraction limit is the theoretical boundary for the resolution of any optical system. Ernst Abbe defined the resolution *d* as:

$$d = \lambda/2 \cdot NA$$

with λ being the wavelength of the used light and *NA* the numerical aperture of the objective lens.[34]

Due to those two limits, traditional methods to increase the imaging resolution are to use shorter wavelength light and high NA objective lenses. Both options come with a clear drawback. Shorter wavelength light, particularly in the UV region leads to potential sample damage and increased autofluorescence. High NA objectives, while effective, are also extremely costly. Another common method to increase the resolution involves the use of immersion objectives. Here a medium with a higher refractive index (usually oil or water) is placed between the lens and the sample, therefore increasing the resolution.

However, even with these methods, the diffraction limit imposes a fundamental restriction on resolution. To overcome the resolution limit, super resolution microscopy techniques have been developed. Nevertheless, simpler methods to enhance the spatial resolution and sensitivity without the complexity of super resolution methods exist. One such method is total internal reflection fluorescence (TIRF) microscopy.[35]

TIRF microscopy is an optical technique enabling the excitation of fluorophores in a thin vertical region, which eliminates background fluorescence from outside the focal plane and therefore drastically increases the signal-to-background ratio. This enhancement of signal-to-background ratio significantly increases the spatial resolution of the detected features. TIRF leverages the phenomenon of total internal reflection, which generates an evanescent wave at the interface between two media with different refractive indices. The evanescent wave is created in a limited spatial region adjacent to the interface between two media, typically a coverslip (transparent solid) with the sample in solution (liquid). The wavelength of the evanescent field is equivalent to the wavelength used for its generation. Due to the exponential decay and adjusted excitation wavelength and the NA of the objective the penetration depth of the evanescent wave can be controlled to be less than 100 nm. Thus, only fluorescent molecules in close proximity to the surface are excited, effectively reducing background signal and eliminating autofluorescence.[36,37] The light path within an objective using TIRF excitation in comparison to epiluminescence excitation is shown in **Figure 4**.[38]

The principle of TIRF is based on Snell's law, which relates the angles of incidence and refraction for light traveling between two media with different refractive indices:[39]

$$n_1 \sin\theta_1 = n_2 \sin\theta_2$$

$$\frac{\sin\theta_1}{\sin\theta_2} = \frac{n_2}{n_1}$$

with n_1 and n_2 being the refractive indices of the two media and θ_1 and θ_2 the angles of incidence and refraction respectively.

The intensity of the evanescent field decreases exponentially with distance from the surface, and the intensity $I(z)$ at a depth z is given by:

$$I(z) = I_0 exp\left(-\frac{z}{d}\right)$$

where I_0 is the initial intensity at the surface, and d is the depth of penetration defined as:[39]

$$d = \frac{\lambda}{4\pi} \frac{1}{\sqrt{n_1^2 \sin \theta_1^2 - n_2^2}}$$

Through precise control of these parameters, TIRF microscopy offers an effective tool of improving spatial resolution, particularly in applications that require high sensitivity and minimal background interference.[40]

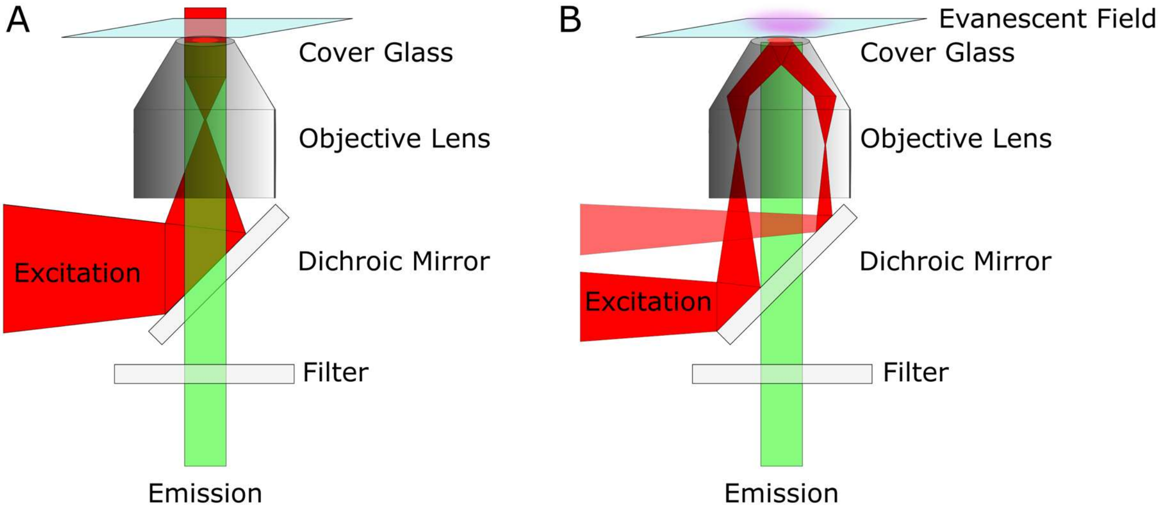

Figure 4. *Light path within an objective lens for (A) Epi fluorescence microscopy and (B) TIRF microscopy. Adapted from Park et al. 2015.*[38]

4.4 Recognition elements

4.4.1 Antibodies

The majority of bioanalytical assays are not performed in well-defined matrices such as buffers that have been perfectly optimized for every assay step to ensure optimal performance. Most target analytes are present in difficult and complex environments or matrices, where the target analyte is present only in small quantities.[10] Therefore, sensitive detection of analytes with high specificity demands the use of highly selective recognition elements, such as antibodies, molecularly imprinted polymers, aptamers, or nucleic acids. Each of these affinity binders comes with distinct advantages and drawbacks (**Table 1**), and no single solution is universally optimal for all assay types. Therefore, the selection and optimization of affinity binders is crucial to achieve the highest sensitivity for the specific analyte and assay platform. This process may involve cross-checking different options based on the target analyte, assay requirements, design, scalability, manufacturing and development costs, and adaptability to other target analytes within the same assay platform.

Immunoglobulins (Ig), more commonly known as antibodies, are specialized glycoproteins produced by B cells as a crucial part of the immune response.[41] There are five main immunoglobulin isotypes in mammals (**Figure 5**): 1) IgD, present in blood in small amounts, plays a crucial role in initiating B cell activation. 2) IgE, responsible for allergic reactions and protection against parasitic infections, mediates the release of histamine from mast cells and basophils. 3) IgA, plays a crucial role in mucosal immunity and therefore is mainly found on mucosal surfaces, such as the gut, respiratory and urogenital tract, and in secretions like salvia and breast milk. 4) IgM, first isotype produced in response to an infection, is highly effective in forming antigen–antibody complexes and activating the complement system, and 5) IgG, the most abundant isotype in blood and extracellular fluid, crucial for opsonization, neutralization of toxins and viruses, and activation of complement system.[42,43]

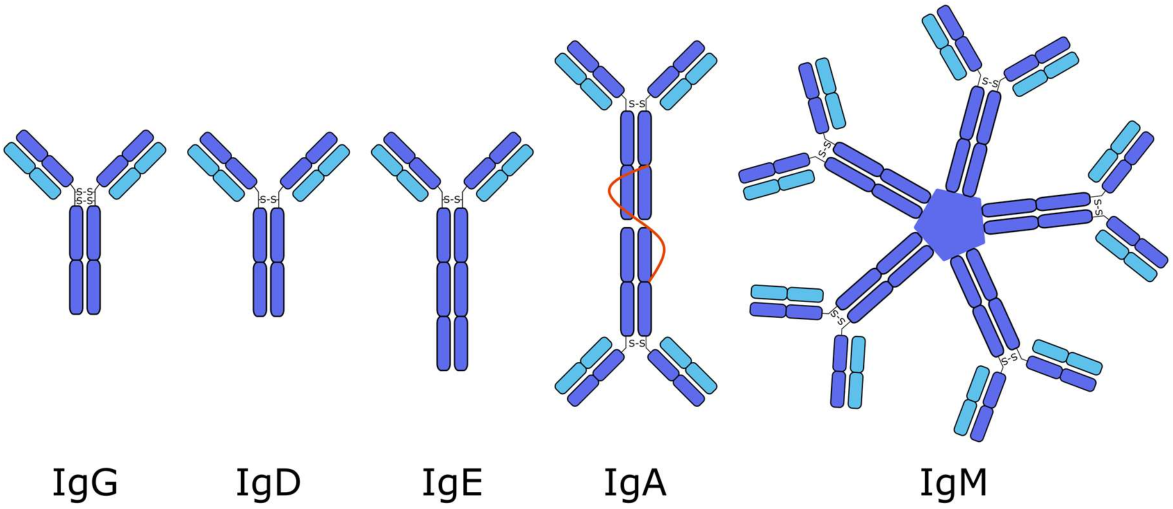

Figure 5. *Schematic of the main immunoglobulin isotypes, IgG, IgD, IgE, IgA and IgM. Each isotype is depicted with its characteristic heavy (blue) and light chains (light blue).*

The most commonly used antibody isotype in immunoassays is IgG. It consists of two identical heavy chains, with a molecular weight of around 50 kDa, and two identical light chains, with a molecular weight of around 20−25 kDa, connected *via* disulfide bonds, creating the widely known Y-shape with the overall molecular weight of around 150 kDa (**Figure 6**).[44] The antigen binding region of an antibody is extremely variable, allowing for the precise recognition of a vast number of antigens and targets. The antigen binding site is formed by the variable (V) regions of the light and heavy chains.[45] This high specificity and large binding constants paired with the easy manipulation of antigen binding sites and the relatively low cost due to the large-scale production is why antibody-based assays make up the majority of all bioanalytical assays.[13]

Based on their production, antibodies can be classified into polyclonal, monoclonal, or recombinant ones. Polyclonal antibodies are produced by injecting an organism, most often mouse or rabbit, with the target antigen. As a result of the animal's immune response, several plasma cell clones produce antibodies specifically targeting different epitopes of the antigen.[46] Polyclonal antibodies have been used as the recognition element in combination with UCNPs, for example, for the detection of the honeybee pathogen *Melissococcus plutonius,*[47] α-fetoprotein,[48] and olaquindox.[49] The process of obtaining polyclonal antibodies is relatively straight forward, but several purification steps are necessary, and their yield and the production capacity is limited. Another drawback is the wide range of affinities the polyclonal antibodies possess towards the epitopes they are specific against, which has limited their use for high-sensitivity applications and commercial platforms.[50]

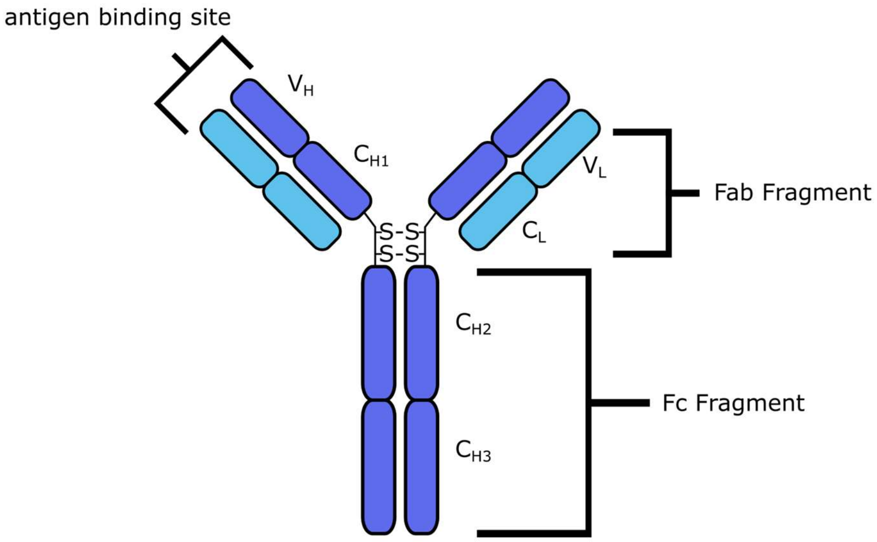

***Figure 6**. The most commonly used antibody, immunoglobulin G (IgG). IgG consist of the Fc fragment and the Fab fragment with the later containing the antigen binding site. The antigen binding site is formed of the variable heavy (V_H) and variable light (V_L) domain, responsible for the target binding and specificity.*

Monoclonal antibodies, on the other hand, can offer high specificity towards their target antigen and are often the preferred type. Monoclonal antibodies are produced by the hybridoma technology, based on fusing B-lymphocytes with immortal myeloma cells. Here, the antibodies are derived from a single plasma cell clone and are, therefore, specific against a single epitope.[51] Consequently, monoclonal antibodies show a higher specificity against a particular epitope compared to polyclonal ones, with far lower batch-to-batch variations. Monoclonal antibodies have been widely used in immunoassays due to their superior binding properties. UCNP-based immunoassays using monoclonal antibodies include, for example, the detection of PSA,[52,53] hepatitis B,[54] and human serum albumin.[53] Nevertheless, monoclonal antibodies are inherently dependent on animal immunization and can be tedious, time-consuming, and expensive to produce.[10]

Recombinant antibodies offer the advantage of easy and low-cost production in comparison with monoclonal and polyclonal antibodies.[55] Recombinant antibody technologies and display systems, most notably phage display[56], have the potential to bypass the immune system and create new antibodies significantly faster.[57] In phage display, recombinant antibody fragments , usually scFv (single-chain fragment variable) or Fab (fragment antigen binding) fragments, are expressed on the surface of a bacteriophage – mainly filamentous phages like M13.[58]

After a wide variety of antibody variants is constructed (antibody library) in a process known as panning, iterative rounds of selection with the target antigen are followed by selective enrichment of high-affinity antibodies. The process of selection and amplification leads to the identification of antibody clones with the desired affinity and specificity towards the target antigen.[59] Individual clones can be further isolated and cloned into full-length IgG format if desired. Phage display not only accelerates the discovery process of antibodies against certain targets but also allows for the fine-tuning of their characteristics, making it an invaluable tool in therapeutic antibody development and biomedical research. Albeit monoclonal antibodies still continue to be the most used antibody format, recombinant antibodies have risen as an interesting alternative with many possibilities.[60] For example, recombinant Fab antibody fragment for 17β-estradiol was employed in a homogeneous upconversion Förster resonance energy transfer (FRET) immunoassay[61], and UCNP-conjugated anti-GFP nanobody was used to study protein interactions inside living cells using FRET.[45,62]

4.4.2 Aptamers

Aptamers are synthetic single-stranded nucleic acid (DNA or RNA) molecules that bind specifically to their target analyte (**Figure 7**). As affinity binders, aptamers have several advantages compared to antibodies. They can be selected *in vitro*, in theory, for any given target independent of the target size (small molecules to cells). Aptamers possess high chemical stability and can be easily synthesized with high reproducibility and purity once the sequence is known. In addition, since aptamers undergo conformational changes during the binding step, a high degree of flexibility in design is given.[63]

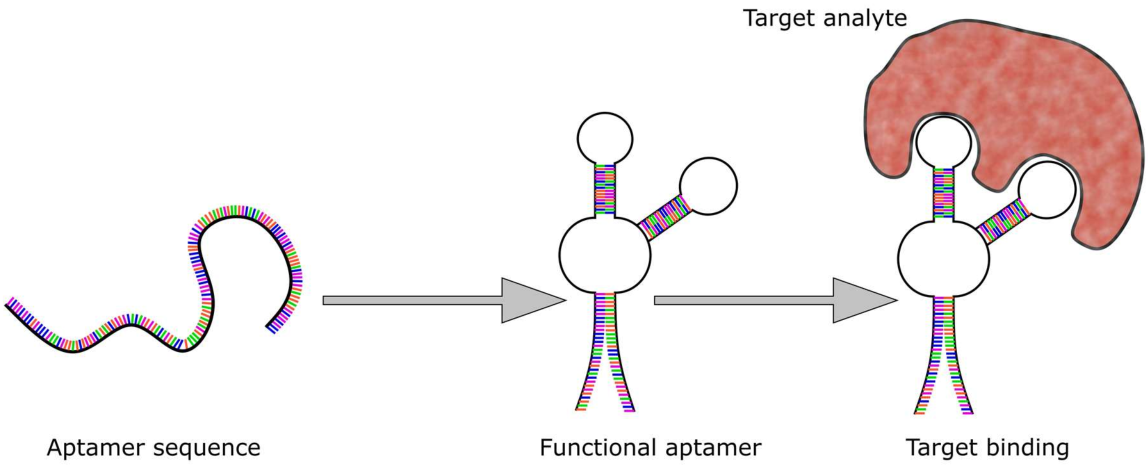

***Figure 7**. Scheme of aptamers that are short single-stranded DNA or RNA molecules that fold and form a three-dimensional structure that enables them to bind specifically to their target.*

Aptamers are developed through an iterative process known as the systematic evolution of ligands by exponential enrichment (SELEX).[64] Here, a large library of up to 10^{16} random oligonucleotides, all having a random region for target binding flanked by two known sequences for primer binding, is first generated. All oligonucleotides in the library then undergo repeated rounds of the following steps: 1) The target analyte is added to the library and all nucleic acids binding to the target are separated from non-binding nucleotides. The separation of binders and non-binders is a critical step, and over time, several different strategies evolved to either simplify the process or increase its efficiency and accuracy.[64] Most commonly, affinity chromatography, membrane filtration, and centrifugation are used. 2) Amplification of the binders using either PCR for DNA aptamers or RT-PCR for RNA aptamers, followed by sequencing. The amplified pool of nucleic acids undergoes multiple times the binding, elution, and amplification step to enrich the pool of high affinity binders until meeting the selected requirements (**Figure 8**).[64–66]

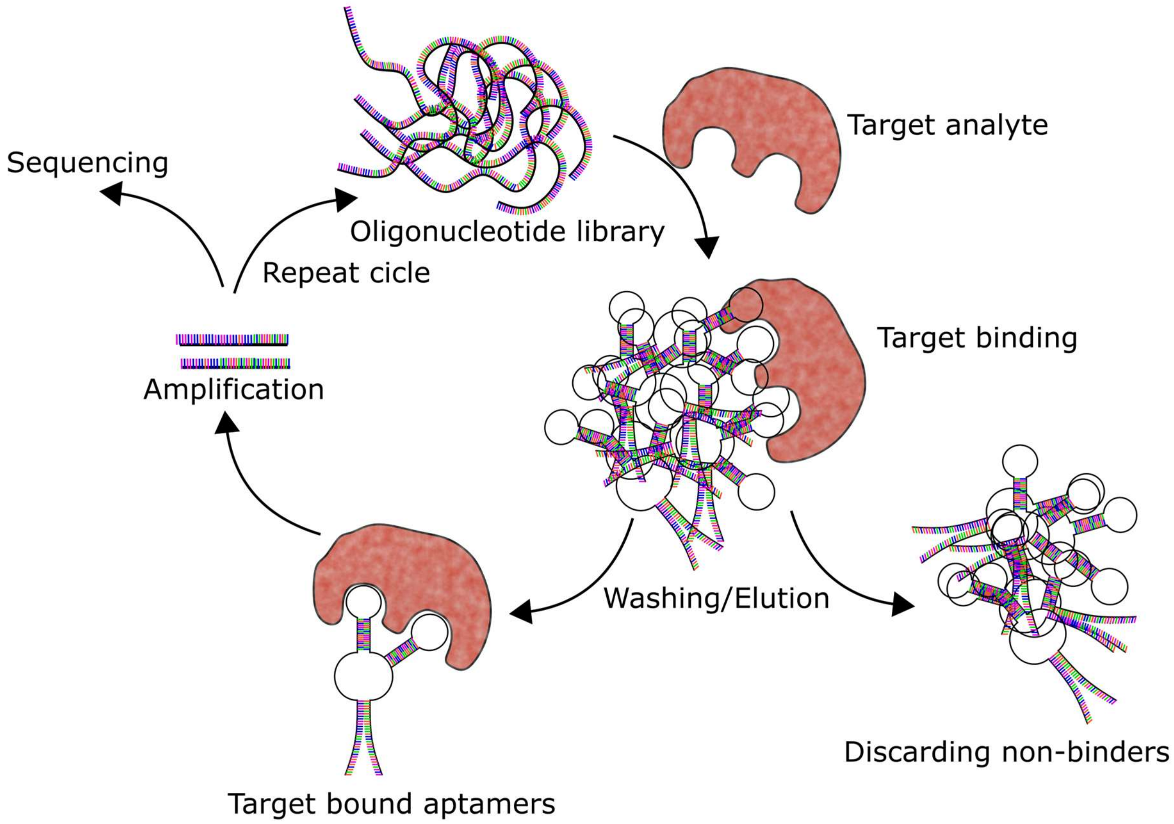

Figure 8*. Aptamer selection process using SELEX. The systematic evolution of ligands by exponential enrichment (SELEX) method typically includes multiple iterative selection rounds performed to enrich and isolate high-affinity aptamers from a diverse oligonucleotide library.*

Even though RNA aptamers have their unique use cases, DNA aptamers are more commonly used due to their higher chemical and biological stability, making the selection and application easier. Additionally, being faster and cheaper, since DNA is easier to synthesize, possesses higher stability regarding storage, and no additional reverse transcription is needed during the amplification step.[67,68]

Aptamers are a popular replacement for antibodies due to all their advantages; however, the success rate the SELEX procedure is low compared to producing new antibodies, probably because of the smaller size and less complex structure of the aptamers.[64] Furthermore, SELEX is rather costly and very time-consuming, with a turnover rate of several months. Also, the use case of the aptamer must be known during the planning step to incorporate certain but needed modifications. For example, unmodified aptamers are prone to degradation caused by serum nucleases, which should be taken into account already during the selection if such matrix will be used.[68] Even though SELEX process for identifying new aptamers is expensive and time-consuming, the large-scale synthesis of the aptamers with a known sequence is very fast and cost-effective. Furthermore, aptamers can be selected for nearly any analyte and their affinity, even though costly, can be improved by increasing the number of SELEX repetition rounds. In addition, their small size compared to conventional antibodies decreases steric hindrances, enabling a higher degree of surface coatings which then leads to increased assay sensitivity. Another benefit of aptamers over antibodies is their resistance towards elevated temperatures, solvents, and extreme pH. Finally, their ability to regain the conformation after denaturation (*e.g.*, *via* heat) makes them the optimal choice for assays and biosensors where regeneration is needed.[63,68–73]

There are numerous articles proving the successful application of aptamers for the detection of various analytes using UCNP labels.[74] For example, Wang *et al*.[75] developed a homogeneous aptasensor based on FRET where in the presence of the analyte, carcinoembryonic antigen (CEA), the conformational change of CEA aptamer separated the aptamer-conjugated UCNPs from graphene oxide. The dissociation of UCNPs from the graphene oxide surface stops the quenching of the luminescence of the UCNP.

4.4.3 Nucleic acid hybridization

Nucleic acids play crucial roles in molecular recognition. Hybridization of nucleic acids by exceptionally strong base pairing with their complementary strand makes them ideal for many types of DNA- or RNA-based assays and sensors. DNA is a very stable molecule, and the synthesis of short oligonucleotide probes has been established as a straight-forward and low-cost process.[76] Moreover, reactive groups or labels can be directly included in the synthesized sequences, nucleic acids offer a particular advantage compared to antibodies. On the other hand, RNA is less stable and prone to RNAses, requiring particular caution and making RNA a less favourable recognition element. [77]

The target analytes for assays using nucleic acids as the recognition element include, for example, disease-specific genes,[78] point mutations,[79] and infectious or harmful bacteria and viruses. [80,81] Nucleic acid hybridization probes can be meticulously engineered to achieve extreme sensitivity and specificity, allowing them to detect individual mutations within the target genome.[79] Even though nucleic acid assays are often simple in design, their application requires the lysis of the host cell to detect the analyte. Moreover, the very high sensitivity and selectivity can also be a drawback, as the slightest mutations in the target sequence may significantly hinder the analyte recognition.[82]

Nucleic acids as target analyte and recognition element are extensively utilized, especially in nucleic acid amplification assays. PCR and other amplification methods offer a high sensitivity owing to the powerful target amplification.[83,84] Direct detection of nucleic acids is less used since the target is often present at low copy numbers. Moreover, similar to PCR primers even subtle changes in salt content can alter the binding behaviour. Therefore, handling nucleic acids in various mediums (buffers, serum, saliva, etc.) demands careful attention to maintain their integrity.[85]

4.4.4 Molecularly imprinted polymers

Molecularly imprinted polymers (MIPs) are synthetic materials mimicking the natural antibody–antigen interaction, selectively binding the molecule used as a template during production.[86] MIPs are generated by polymerizing functional monomers and cross-linkers in the presence of a target molecule, which serves as the template (**Figure 9**). After the imprinting and removing the template, the MIP consists of specific cavities printed on a three-dimensional structure that is complementary in shape, size, and arrangement to the target molecule.[10] The three main MIP preparation methods include, 1) synthesis from monomers in the presence of the template, 2) phase inversion and polymer precipitation by the addition of solvent or by the evaporation of the solvent from a networked solution of polymer, and 3) soft lithography or surface stamping.[86] However, the later ones rarely provide MIPs with the specificity needed for biosensing.

MIPs have also been used as the recognition element in upconversion assays and biosensors. For example, biomimetic upconversion sensors using MIPs enabled the detection of pesticides carbendazim,[87] octopamine,[88] and acetamiprid.[89] In these applications, UCNPs were encapsulated with MIPs using functional monomers, such as methylacrylic acid or APTES, together with different cross-linking agents, and binding of the target analyte to the MIP receptor could be observed as a change in the upconversion emission.

MIPs are usually unable to compete with antibodies in terms of affinity or specificity, but they have the significant advantage of resistance towards harsh conditions under which antibodies or other biomolecules denature. Such conditions include high temperatures, high solvent concentrations, acidic or alkaline environments, and UV irradiation. Furthermore, compared to (monoclonal) antibodies, MIPs are cheap in production and can be easily tailored for a wide variety of target analytes ranging from small molecules to larger biological species, such as immunoglobulins or viruses.[90]

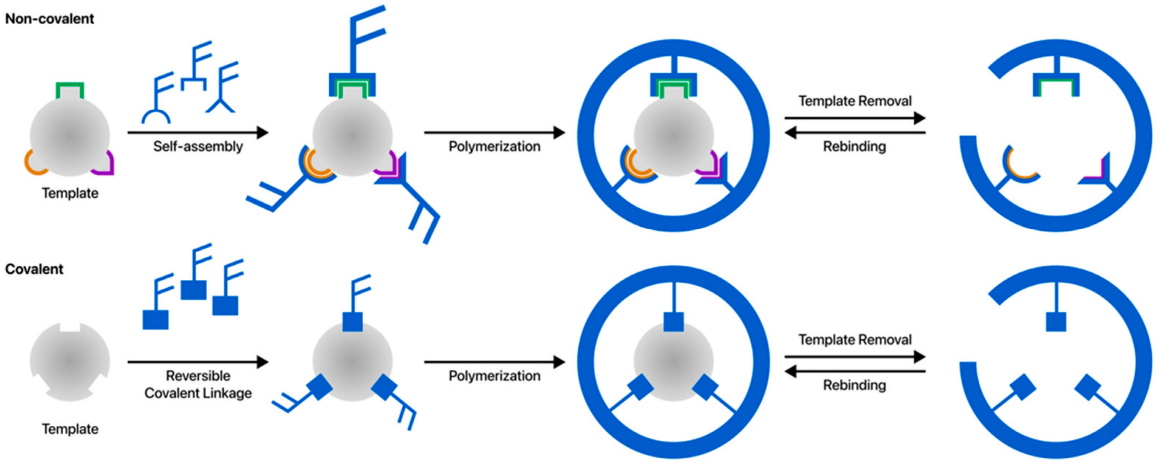

Figure 9. *Scheme of MIP procedure using non-covalent or covalent approach for the printing. After forming the complex, where the template molecule is covalently or non-covalently linked to functional monomers, the cavities are formed during the polymerization. Finally, once the template is removed from the polymer, specific binding sites are former specific to the template molecule. Reprinted with permission from Akgönüllü et al. (2023).*[91] *Copyright Elsevier 2023.*

***Table 1** . Comparison of different recognition elements summarizing the advantages and disadvantages of various recognition elements, including antibodies, aptamers, molecularly imprinted polymers (MIPs), and nucleic acids, highlighting their unique properties for biosensing applications.*

Recognition element	**Advantages**	**Disadvantages**
Antibodies Polyclonal (pAb) Monoclonal (mAb) Recombinant (rAb)	• High specificity and affinity • Low production cost (pAb, rAb) • Various epitopes, robust detection (pAb)	• Batch-to-batch variation (pAb) • Dependent on animal immunization (pAb, mAb) • High cost (especially mAb) • Sometimes unstable • Some haptens are difficult targets.
Molecularly imprinted polymers	• Low cost • High physical and chemical resistance (*e.g.*, temperature, pH)	• Limited specificity • Compatibility with aqueous solutions.
Aptamers	• Small size and low-cost large-scale production • Stable, simple to produce once the sequence is known • Easy to prepare and modify. • Good stability	• Strict to hybridization conditions • Long-term SELEX process • May require additional complex steps
Nucleic acid hybridization	• High specificity • Simple to produce. • Stable	• Restricted to complementary nucleic acid detection. • Strict to hybridization conditions

4.5 Optical label technologies

4.5.1 Enzymes

Enzymes are considered the gold standard detection label in immunoassays. For example, the well-known enzyme-linked immunosorbent assays (ELISA) was introduced in the 1970s, leveraging the catalytic ability of enzymes to generate a chromogenic, fluorogenic, or luminescent signal upon the addition of the suitable substrate.[92,93] Optimizing an ELISA involves selecting the optimal enzyme for the specific application to achieve the maximum performance. Key factors in the selection include the available substrates with their corresponding readout methods, the enzyme turnover rates, and whether any assay components might interfere with the enzymatic reaction.[94] Commonly used enzymes, such as horseradish peroxidase (HRP) and alkaline phosphatase (AP), are popular due to their robust activity and compatibility with various substrates.[95] Enzyme-based labels are particularly advantageous since the enzymatic reaction can be finely tuned to optimize signal intensity and duration. Furthermore, due to the high turnover rates of these enzymes, producing a large amount of detectable product by a single enzyme molecule, even trace amounts of target can be detected, improving the assay sensitivity dramatically.[96]

On the other hand, enzymes are susceptible to matrix interferences, often requiring high sample dilution factors. ELISAs often suffer from a narrow dynamic range due to the nature of the signal amplification. Nevertheless, their simplicity and wide spread of compatible readers make ELISA one of the most widely adapted bioanalytical methods.[97]

In addition, when ultrasensitive detection is needed, enzymatic detection can be combined with digital readout methods. The most popular example is the single-molecule array, where single enzymes are loaded into femtoliter-sized wells, which enables single-molecule detection.[98]

4.5.2 Gold nanoparticles

Gold nanoparticles (AuNPs) are widely used as labels in bioanalytical assays due to their versatile optical, chemical, and electrical properties, which all can be fine-tuned by adjusting the size and shape of the nanoparticles during their synthesis. There are two kinds of approaches to synthesizing AuNPs: physical and chemical methods. Physical methods include microwave irradiation, UV radiation, laser ablation, and photochemical processes.[99] Chemical synthesis methods are more commonly used, with the Turkevich method, later optimized by Frens, being the most popular. In this method, an aqueous solution of gold salts or chloroauric acid ($HAuCl_4$) is mixed with a reducing agent, typically citrate, under continuous stirring.[100,101] The size and monodispersity of the AuNPs are controlled by adjusting the pH and temperature of the system, producing nanoparticles in the range of 5–150 nm.[102] After the synthesis, the AuNPs are usually stabilized by a coating consisting of citrate groups.[103]

Most assays taking advantage of AuNPs employ particles conjugates with the recognition elements. A straightforward method for surface modification is the passive adsorption of biomolecules onto the nanoparticle surface. Even though this technique is straightforward, it is used less commonly due to the several significant drawbacks; The passive adsorption offers only a limited control over the orientation of the attached recognition elements, and furthermore, it results in weaker binding interactions that can lead to dissociation of the recognition element, therefore, generally producing less stable conjugates.[104] Another common strategy exploits the strong Au-S bond, allowing stable binding of the target biomolecule to the nanoparticle surface through simple modification with sulfhydryl groups.[105]

The popularity of AuNPs in bioanalytical assays is connected with their numerous advantages. AuNPs are non-toxic and have a high biocompatibility, and produce a significant colour change after aggregation, making them an excellent label for colorimetric and lateral flow assays.[106] In addition, their ability to act as a quencher for fluorescence, together with the ability to easily modify their surface, makes them an ideal solution for FRET-based biosensors. [10,104,107]

4.5.3 Quantum dots

Quantum dots are semiconductor nanoparticles usually consisting of group 2‒6 (CdS, CdTe, CdSe, ZnS and ZnSe) and 3‒5 (InP) semiconductors showing a quantum confinement effect depending on their size. Quantum dots are one of the most frequently used labels due to their small size (1‒10 nm in diameter) and their easy tuning of their emission and excitation wavelength from the UV to the NIR range (380‒2000 nm).

The synthesis of QDs is crucial as their optical properties strongly depend on the particle size. Typically, a coordinating solvent, usually trioctylphosphine oxide (TOPO), is used to dissolve the precursors in organic solvents. The synthesis of all CdE (E=S, Se, Te) includes heating the mixture of CdO and TOPO to around 300 °C, then injecting either TOPSe or TOPTe into the hot mixture under stirring.[108,109] By adjusting the temperatures and growth times the size and shape of QDs can be precisely controlled. To greatly reduce the toxicity and enhance the otherwise low photoluminescence and quantum yield, QDs are mainly used in core‒shell structures, where the CdE core is passivated by a thin layer of ZnS (sometimes even CdS). When designing the core shell structure, it must be kept in mind, that the shell must have a larger energy band gap than the core, leading to a confinement of the excitons in the core, increasing the photoluminescent properties.[110,111]

After synthesis QDs are usually coated with organic ligands such as TOPO, which needs to be either removed or modified to render the nanoparticles water dispersible. Furthermore, QDs need to be stable in aqueous solutions over a broad pH and ionic strength range while the surface coating should prevent luminescence quenching while enabling further surface modification for their specific use case.[112] Similar to other nanoparticle surface chemistry, rendering QDs hydrophilic can be achieved in three different methods. First, removing the hydrophobic coating and replacing it with water soluble molecules which coordinate to the QD surface with high affinity while leaving functional groups for further modification. This is often achieved using polymers that are highly biocompatible, low cost, and easy to synthesize and custom modify with appropriate groups.[112] Another strategy to render QDs hydrophilic while protecting them from water is their encapsulation with silica. The advantage is silica coating is its common use and therefore a huge repertoire of existing protocols. Furthermore, the silica shell is inert, non-toxic and give all other advantages an extra shell on NP surface can provide. For commercial use, the silanization might be very interesting since the surface coating also prevents leaching of QD components into the matrix, especially the toxic Cd.[112]

QDs are remarkably interesting label for bioanalytical applications. Having a broad absorption spectra enables the use of QDs as optimal donors or acceptors for FRET applications and furthermore make it easy to excite with a high amount of photons so low excitation power densities are needed and the excitation of several QDs with the same excitation source of different sized (colour) QDs enables easy multiplexing with nearly no spectral crosstalk.[113] Furthermore, the long fluorescent lifetimes enable lifetime measurements and time-resolved measurements which lower background signal caused by background fluorescence thus possibly increasing assay sensitivity. In contrast to organic dyes, inorganic QDs possess high photostability, show no bleaching and therefore enable easier handling since it does not have to be under complete darkness making the readout more simple.[108,110]

Nevertheless, the use of QDs is limited as the toxic Cd can leach. The toxicity can be reduced drastically with an extra shell, of either ZnS or silica, a small percentage of Cd might still leak and therefore be a health risk. Even though QDs can be synthesized with at a relatively small size of a few nanometres, when adding a second shell and surface coating hydrodynamic diameters of 10–60 nm are more common. This makes QDs as labels usually too large to enter cells. From synthesis, surface modification until application it must be ensured that the QDs do not aggregate in sometimes complex media with high ionic strengths. This not only increases the need for optimal surface modification methods but also the necessary workload and therefore the costs since after each step, from synthesis to application, the homogeneity of the particles must be ensured, and eventual aggregates need to be removed. Compared to molecular labels such as fluorophores or lanthanide chelates, nanoparticle labels always come with the drawback of steric hindrance which might affect the binding efficiency of the chosen affinity binder. Finally, their intermittent emission (“blinking”) makes QDs unsuitable for the use in single particle tracking or counting due to the repeated loss of signal.[111,112,114,115]

4.5.4 Photon-upconversion nanoparticles

4.5.4.1 Upconversion mechanism

UCNPs are inorganic lanthanide-doped nanoparticles with special optical properties. Due to the close proximity of the energy levels of the used lanthanide ions and the long lifetimes of their excited states, high excitation states can be achieved by absorbing two or more photons in the NIR range. The upconversion process is enabled by Ln^{3+} ions and their luminescence properties, such as narrow emission bands, well-defined multiple excited states, and long luminescent lifetimes.[116] To achieve upconversion, one lanthanide ion, specifically Yb^{3+} ions are crucial as a co-dopant. Yb^{3+} ions act as sensitizer, since it possesses only a single excited state, it has a higher extinction coefficient compared to other Ln^{3+}. This, together with having resonant electronic energy states with other co-dopants such as Pr, Nd, Dy, Ho, Er, and Tm ions transferring the absorbed energy to those co-dopants, enhancing the upconversion efficiency.[117]

Excitation and relaxation from high-energy excited states occur most commonly through one of the three different pathways, all resulting in the emission of a photon of higher energy in the VIS to the UV range, the so-called anti-Stokes shift or anti-Stokes emission (**Figure 10**). The first of those three pathways is excited state absorption (ESA), the second pathway is energy transfer upconversion (ETU), and the last one being a relatively recent discovery of photon avalanche (PA).[118]

In ESA, an electron is excited *via* a photon from the ground state (G) to an intermediate metastable excited state (E1), called ground state absorption (GSA). While the electron is still in the long-lived excited state, the subsequent absorption of one or several additional photons excites the electron to the second excited state (E2). The relaxation from this higher energy level then leads, apart from nonradiative losses, to the emission of a higher-energy photon.[118,119]

ETU, on the other hand, involves interactions between two nearby ions. One ion (sensitizer), in an excited state, transferrs its energy non-radiatively to a neighbouring ion (activator), also in an excited state. The activator is, therefore, lifted to the second excited state, leading again to the emission of a higher-energy photon.[120] The most recently discovered pathway in nanoparticles, known as photon avalanche (PA), is based on a feedback loop, where the emitted photons can further excite other sensitizer ions, sustaining and amplifying the avalanche effect.[121,122] This feedback mechanism is responsible for the rapid and dramatic increase in luminescence intensity once the excitation power threshold is exceeded. The hallmark of PA is this critical power threshold; below it, the upconversion luminescence is weak and linear with respect to excitation power. Once crossed, the luminescence intensity increases exponentially with further increases in excitation power, showcasing the nonlinear nature of the process.[123–129]

These upconversion processes are heavily influenced by the host matrix, dopant ion concentrations, the spatial distribution of the dopant ions, and the energy differences between the ground state, first and second excited state.[119] Compared to fluorescence, upconversion luminescence exhibits far lower quantum yields (QY), usually in a range of 0.9%[130] compared to up to 90% for fluorophores.[131] The low QY is caused by several factors, primarily because photon-upconversion is a multiple-photon process, it can never exceed 50%. As lanthanides exhibit low absorption cross sections, high excitation power densities are needed to enable ESA. The drawback of the low absorption cross section can be bypassed *via* the ETU process utilizing sensitizers with higher absorption cross sections. In recent years, the upconversion efficiency increased severely due to the better design of upconversion materials.[121,122] Another limitation of the upconversion process is the nonlinearity with the luminescence intensity, depending on the *n*-th power of the excitation intensity where *n* denotes the number of absorbed photons per one emitted photon. PA exploits this nonlinearity, resulting in a dramatic increase in luminescence when the excitation power surpasses a certain threshold. This process begins when UCNPs are irradiated with NIR light, typically in the range of 800–1000 nm. Sensitizer ions, often rare earth ions like erbium (Er^{3+}) or thulium (Tm^{3+}), absorb the NIR photons, promoting the sensitizer ions from their ground state to an intermediate excited state.

Following this initial excitation, the excited sensitizer ions can absorb additional NIR photons, which promotes them to even higher excited states through the ESA process. At a specific excitation power threshold, a population inversion occurs, where the population of ions in the excited state exceeds that in the ground state. This population inversion is crucial for PA as it leads to a rapid and exponential increase in the probability of subsequent photon absorptions, initiating the avalanche effect.[132]

The highly excited sensitizer ions then transfer their energy to neighbouring activator ions, typically Ytterbium (Yb^{3+}) or another rare earth ion, through the ETU process. This energy transfer process can be repeated multiple times, resulting in the activator ions reaching very high energy states. These highly excited activator ions then relax back to lower energy levels by emitting photons, often in the visible range despite the initial NIR excitation. This results in the characteristic upconversion luminescence, where the luminescence intensity is disproportionately high compared to the increase in excitation power due to the nonlinear nature of the photon avalanche.[116,121,133]

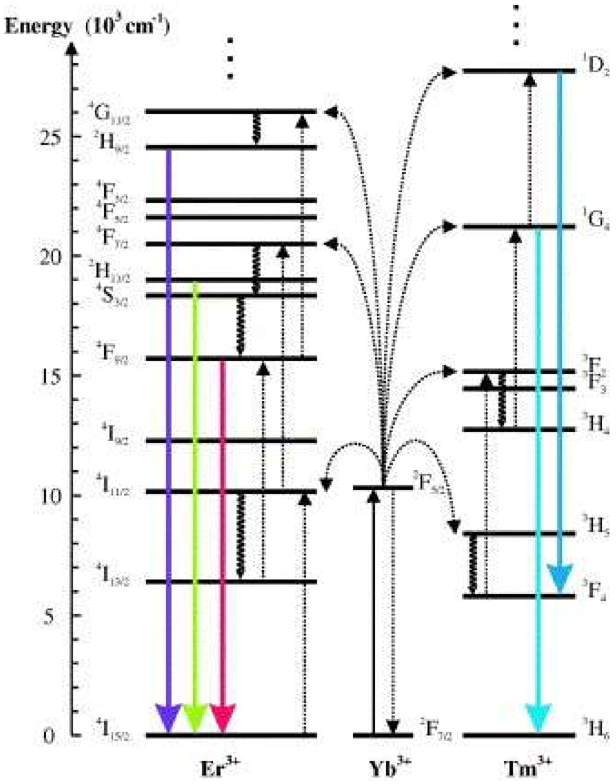

***Figure 10**. Energy diagram of energy transfer processes (ETU) involved in Yb^{3+} and Er^{3+} doped UCNPs.*

4.5.4.2 Synthesis of UCNPs

There are two general methods to obtain nanoparticles, the “top-down” approach, involving grinding or milling bulk material to nanometer scales, and the “bottom-up” approach synthesizing nanoparticles from molecular precursors.[134] The latter one offers superior control and freedom over the nanoparticle architecture, allowing for the synthesis of highly homogeneous NPs with customizable features, such as varying dopant ratios, compositions, and shell sizes.[11,135] Consequently, this section of the thesis will focus on the “bottom-up” approach.

The synthesis of UCNPs commonly utilize precursors based on metal organic compounds of rare earth elements, such as trifluoroacetates, oleates, and acetates.[136] The selection of synthesis route, precursor and host material plays a crucial role to obtain high quality nanoparticles. To date, the most efficient host material for upconversion is based on sodium yttrium tetrafluoride ($NaYF_4$), due to the low phonon energy and larger band gap which minimizes non-radiative losses and increases upconversion efficiency.[137] UCNPs based on $NaYF_4$ exist in two different crystal structures, cubic (α-) phase and hexagonal (β-) phase, with the later showing far superior luminescent properties.[138]

In the thermal decomposition approach, lanthanide precursors and host matrix components, typically in the form of metal salts or complexes, such as fluorides, chlorides, and acetates, are dissolved in a mixture of solvents. The selection of solvents and their ratios is crucial not only to facilitate the control of particle size and morphology but also to influence the luminescent properties. The typically used mixture consists of oleic acid or oleylamine which serve as capping ligands and reduce particle growth and aggregation, and 1-octadecene which provides the necessary environment for the precursor decomposition.[139,140] During the synthesis, the precursors undergo controlled thermal decomposition at elevated temperatures ranging from 150 °C to 350 °C under an inert gas atmosphere. In the presence of coordinating ligands and surfactants, this leads to the formation of uniform nanoparticles with precise control over size and morphology. During the heating process, the metal precursors decompose, and the resulting metal oxide or oxysulfide species nucleate and grow to form crystalline UCNPs.[141]

In the coprecipitation approach, lanthanide dopants are introduced into the host matrix through simultaneous precipitation of lanthanide ions and host matrix components at high temperatures. Here, lanthanide salts are dissolved along with precursors of the host matrix, such as metal oxides or hydroxides. The solution is then subjected to elevated temperatures, typically above 300 °C, to induce coprecipitation of lanthanide ions with the host matrix components. This process allows for the incorporation of lanthanide dopants directly into the crystal lattice of the host matrix, ensuring homogeneous distribution and minimizing defects. The resulting UCNPs exhibit enhanced stability and upconversion efficiency compared to physically mixed systems.[142,143] Both methods yield highly monodisperse nanoparticles with narrow size distributions and control over their crystal structure *via* the adjustment of reaction time, temperature, precursor, and solvent.

4.5.4.3 UCNP surface modification

After the synthesis, UCNPs are commonly capped with a hydrophobic layer (usually oleic acid) and dispersed in organic solvents, such as (cyclo)hexane, chloroform, or toluene.[119] To take advantage of the special optical properties of UCNPs in bioassays, it is important to render them dispersible in aqueous media. This is most commonly achieved in either a two-step approach, removal of the oleic acid followed by coating of the NP surface with a hydrophilic moiety or by covering the oleic acid layer with an additional layer *via* bilayer formation or encapsulation (**Figure 11**).[135,144,145] Furthermore, the surface modification of UCNPs also aims to decrease non-specific binding of and can enable easy and very specific further modifications with biomarker-specific ligands.[146]

Especially UCNP encapsulation by silica coating is a popular method to render UCNPs water-dispersible with a high degree of freedom for further surface modification utilizing EDC/NHS chemistry. The silica shell of UCNPs is prone to nonspecific adsorption of proteins, and therefore blocking of the surface with, for example, proteins such as BSA, followed by modification of those proteins is recommended. This is particularly important when the UCNPs are used in matrixes or applications in combination with biomolecules.[147] Several groups used silica-coated UCNP conjugates with biorecognition molecules, such as antibodies, aptamers, or streptavidin for the detection of biomarkers.[148–151]

Moreover, silica-coated UCNPs for targeted drug delivery is gaining popularity. This is achieved by encapsulating the UCNP surface with a mesoporous silica shell, followed by incorporating the desired drug. For example, loading silica-coated UCNPs with rose Bengal to generate reactive oxygen species makes such conjugates an ideal alternative for photodynamic therapy.[147]

As an alternative to the coating of the UCNP surface with a silica shell, modification *via* ligand exchange can also be used. There are two main ligand exchange approaches, the direct substitution of the surface coating with a new ligand and a two-step procedure of ligand removal *via* strong acids such as $NOBF_4$ or HCl to render ligand-free UCNPs, followed by coating with a new ligand.[144,152] Especially the modification with polymers, such as polyacrylic acid (PAA) and polyethylene glycol (PEG) enables an enormous potential for further applications or the improvement of already existing ones.[135,152,153] The modification with polymers brings a wide variety of advantages. Many polymers can either be commercially obtained or easily custom synthesised with specific reactive groups.

Carboxyl groups show a high binding affinity to the lanthanide ions of UCNPs, making the surface coating of UCNPs with PAA very simple. A study by Himmelstoß *et al*.[154] showed that the use of PAA provides dense surface coverage of the UCNPs, forming a thin layer around the nanoparticle. The pH sensitivity of PAA can be exploited for controlled drug release or specific bioanalytical applications involving pH changes. The dense surface coating is a significant advantage. Further surface modification *via* EDC/NHS chemistry enables the coupling of a wide variety of different biomolecules to the UCNP surface. Furthermore, the coating with PAA introduces a negative surface charge to the nanoparticle, which improves the electrostatic stability in aqueous media and prevents aggregation.[155] Therefore, many biosensors and immunoassays use PAA coating. For instance, Lahtinen et al.[155] optimized the surface modification of UCNPs with PAA, coupling it with antibodies or nucleic acids for the detection of human cardiac troponin and PSA, respectively. With fine adjustments of the coating thickness, they achieved detection limits of 0.13 pg/mL for the detection of troponin[156] and 1.3 nM for the detection of miR-20a micro RNA.[157] The main limitation of this method is that the anchoring PAA to the UCNP surface *via* carboxyl groups is weaker compared to the coordination of phosphonate groups.[154] Additionally, the coupling with antibodies and other biomolecules *via* EDC/NHS chemistry is not site-specific. Furthermore, it has been demonstrated that the surface modification with PAA exhibits higher toxic effects on certain species compared to other polymers, especially PEG.[158]

Unlike PAA, PEG stabilizes the nanoparticles in aqueous dispersions through steric repulsion rather than electrostatic repulsion, as it does not impart any surface charge. Therefore, dense surface coating is needed to ensure long-term stability and prevent aggregation. The surface modification with PEG offers several advantages over PAA. Notably, due to its hydrophilic nature, PEG significantly reduces the protein corona formation due to nonspecific protein adsorption around the nanoparticle. This minimizes background signals caused by nonspecific binding and reduces agglomeration and steric hindrances caused by the protein corona.[159]

While PAA also reduces nonspecific binding to some extent, it is less effective than PEG in this regard.[160,161]

Moreover, several studies on the cytotoxicity of UCNPs have shown that PEGylation of UCNPs significantly decreases cytotoxicity compared to PAA and other polymers, which is crucial for *in vivo* bioanalytical applications.[158] Due to the lack of surface charge and the increased hydrophilicity, PEG-coated nanoparticles exhibit prolonged circulation time in the bloodstream. The hydrophilic barrier around the nanoparticle prevents the recognition and clearance by the mononuclear phagocyte system, making it particularly useful in diagnostic and therapeutic applications requiring extended nanoparticle presence.[160,162,163] A crucial advantage of PEG surface coating is the flexibility for further functionalization. The modification of PEG chains with various reactive groups is simple, opening endless possibilities for the conjugation of targeting ligands, drugs, or imaging compounds. Numerous PEG modifications are commercially available with reactive groups on both ends, enabling easy custom modification of PEG as a spacer or building block to create unique surface functionality.[162,164]

Consequently, throughout the course of this work, the surface of UCNPs was modified using a special bifunctional PEG. NHS-PEG-alkyne was used as a commercially available precursor, with the NHS ester coupling the PEG to the amino group of neridronate.[165]

This linker offers several advantages over conventional or mono-functionalized PEG derivatives. 1) The bisphosphonate group of neridronate strongly coordinates to the trivalent lanthanide ions on the UCNP surface, ensuring robust binding without the risk of linker dissociation from the surface. 2) Depending on the length, PEG reduces surface quenching of the upconversion luminescence by water, as PEG acts as a crowding agent. 3) UCNPs modified with PEG are hydrophilic and highly stable in aqueous media; due to the steric repulsion also long-term storage without aggregation can be ensured. 4) Most importantly, the alkyne group enables highly specific, precise, and rapid conjugation with biomolecules carrying an azide group.[166–169] This capability opens up numerous possibilities for further modifications *via* bioorthogonal click reactions, provided that the biomolecule either already possesses an accessible azide group or it can be modified with a terminal azide group. Many biomolecules used in immunoassays can easily be modified with an terminal azide group using NHS-R-azide (R= (polymer-)spacer) or *via* the incorporation of unnatural amino acids carrying one of the click reaction partners.[170] The length and composition of the spacer between the reactive NHS ester and the azide can be varied to meet specific demands, offering many possibilities. For example, PEG molecules of different lengths are commonly used to avoid steric hindrance during the click reaction and to render the reactive biomolecule water-soluble.[162,166,171–173]

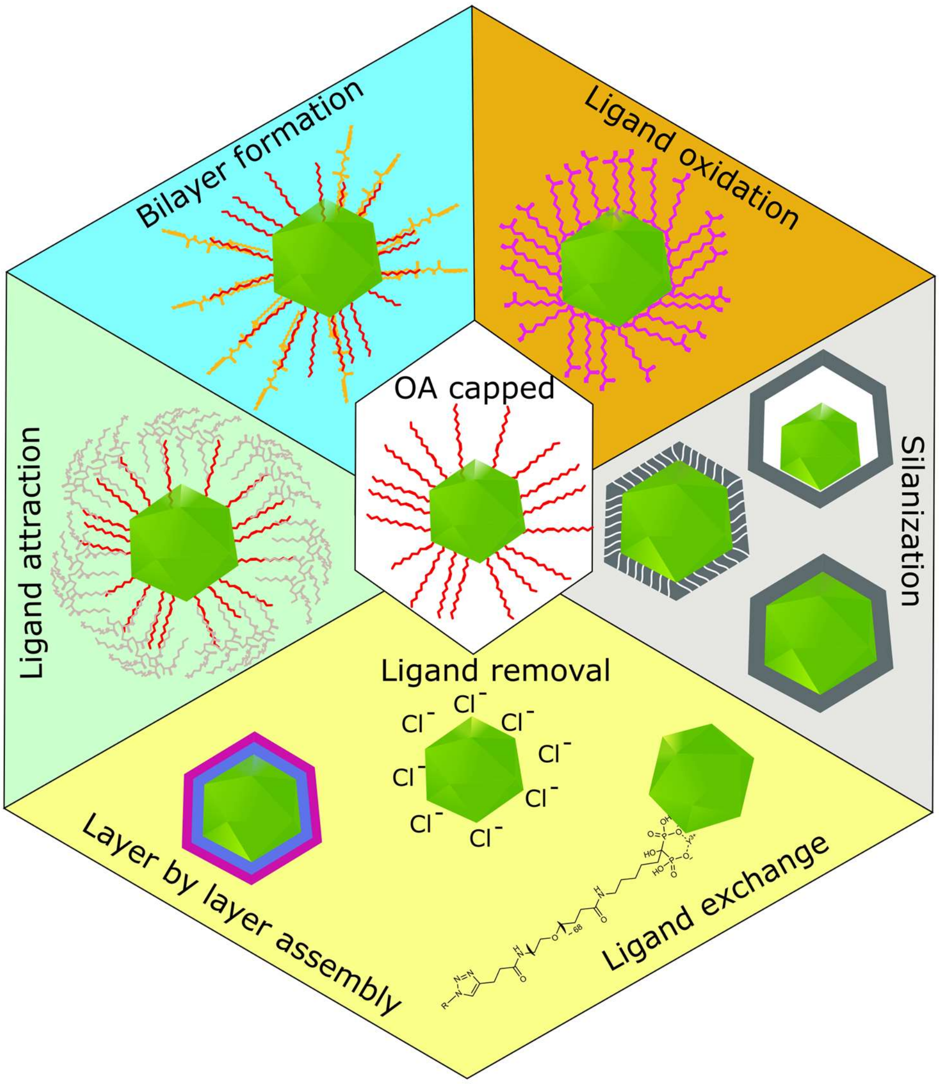

***Figure 11**. Overview of methods for the surface modification of UCNPs. Modified from Li et al. 2022.*[118]

5 References

[1] R. S. Yalow, S. A. Berson, *Nature* **1959**, *184*, 1648.

[2] F. J. Pérez-Reche, K. J. Forbes, N. J. C. Strachan, *Sci. Rep.* **2021**, *11*, 20728.

[3] A. H. B. Wu, *Clin. Chim. Acta* **2006**, *369*, 119.

[4] P. D. Howes, R. Chandrawati, M. M. Stevens, Science. **2014**, *346*, 1247390.

[5] M. Holzinger, A. Le Goff, S. Cosnier, *Front. Chem.* **2014**, *2*, 63.

[6] M. De, P. S. Ghosh, V. M. Rotello, *Adv. Mater.* **2008**, *20*, 4225.

[7] J. Lei, H. Ju, *Chem. Soc. Rev.* **2012**, *41*, 2122.

[8] D. Tang, Y. Cui, G. Chen, *Analyst* **2013**, *138*, 981.

[9] H. Kang, L. Wang, M. O'Donoghue, Y. C. Cao, W. Tan, in *Optical biosensors: Today or tomorrow* (Eds.: F. S. Ligler, C. A. R. Taitt), Elsevier. Amsterdam, Oxford **2008**, p. 583.

[10] Z. Farka, J. C. Brandmeier, M. J. Mickert, M. Pastucha, K. Lacina, P. Skládal, T. Soukka, H. H. Gorris, *Adv. Mater.* **2024**, *36*, e2307653.

[11] H. H. Gorris, U. Resch-Genger, *Anal. Bioanal. Chem.* **2017**, *409*, 5875.

[12] Y. Wu, Y. Fu, J. Guo, J. Guo, *Talanta* **2023**, *265*, 124903.

[13] D. Wild, *The immunoassay handbook: Theory and applications of ligand binding, ELISA and related techniques*, Elsevier, Amsterdam **2013**.

[14] C. P. Price, *Principles and Practice of Immunoassay*, Palgrave Macmillan UK, London **1991**.

[15] I. A. Darwish, *Int. J. Biomed. Sci.* **2006**, *2*, 217.

[16] S. Zhou, L. Xu, H. Kuang, J. Xiao, C. Xu, *Analyst* **2020**, *145*, 7088.

[17] Y. Xiong, Y. Leng, X. Li, X. Huang, Y. Xiong, *TrAC Trends Anal. Chem.* **2020**, *126*, 115861.

[18] Z. Farka, M. J. Mickert, M. Pastucha, Z. Mikušová, P. Skládal, H. H. Gorris, *Angew. Chem. Int. Ed.* **2020**, *59*, 10746.

[19] D. M. Rissin, D. R. Fournier, T. Piech, C. W. Kan, T. G. Campbell, L. Song, L. Chang, A. J. Rivnak, P. P. Patel, G. K. Provuncher, E. P. Ferrell, S. C. Howes, B. A. Pink, K. A. Minnehan, D. H. Wilson, D. C. Duffy, *Anal. Chem.* **2011**, *83*, 2279.

[20] T. Huynh, B. Sun, L. Li, K. P. Nichols, J. L. Koyner, R. F. Ismagilov, *J. Am. Chem. Soc.* **2013**, *135*, 14775.

[21] F. Gong, Z. Tan, X. Shan, Y. Yang, S. Tian, F. Zhou, X. Ji, Z. He, *Anal. Chem.* **2024**, *96*, 3517.

[22] Y. Zhang, H. Noji, *Anal. Chem.* **2017**, *89*, 92.

[23] H. Liu, Y. Lei, *Biosens. Bioelectron.* **2021**, *177*, 112901.

[24] H. H. Gorris, T. Soukka, *Anal. Chem.* **2022**, *94*, 6073.

[25] Quanterix, *Simoa® Technology | Quanterix* **2023**, https://www.quanterix.com/simoa-technology/ (Accessed June 2024).

[26] H. Liu, Y. Lei, *Biosens. Bioelectron.* **2021**, *177*, 112901.

[27] X. Wang, D. R. Walt, *Chem. Sci.* **2020**, *11*, 7896.

[28] D. Chen, X. Zhang, L. Zhu, C. Liu, Z. Li, *Chem. Sci.* **2022**, *13*, 3501.

[29] D. H. Wilson, D. W. Hanlon, G. K. Provuncher, L. Chang, L. Song, P. P. Patel, E. P. Ferrell, H. Lepor, A. W. Partin, D. W. Chan, L. J. Sokoll, C. D. Cheli, R. P. Thiel, D. R. Fournier, D. C. Duffy, *Clin. Chem.* **2011**, *57*, 1712.

[30] L. He, D. R. Tessier, K. Briggs, M. Tsangaris, M. Charron, E. M. McConnell, D. Lomovtsev, V. Tabard-Cossa, *Nat. Commun.* **2021**, *12*, 5348.

[31] Y. Zhang, H. Gu, H. Xu, *Sens. Diagn.* **2024**, *3*, 9.

[32] B. Zhao, C. Che, W. Wang, N. Li, B. T. Cunningham, *Talanta* **2021**, *225*, 122004.

[33] D. M. Rissin, C. W. Kan, T. G. Campbell, S. C. Howes, D. R. Fournier, L. Song, T. Piech, P. P. Patel, L. Chang, A. J. Rivnak, E. P. Ferrell, J. D. Randall, G. K. Provuncher, D. R. Walt, D. C. Duffy, *Nat. Biotechnol.* **2010**, *28*, 595.

[34] Nikon’s MicroscopyU, *Resolution* **2024**, https://www.microscopyu.com/microscopy-basics/resolution. (Accessed June 2024).

[35] E. J. AMBROSE, *Nature* **1956**, *178*, 1194.

[36] Nikon’s MicroscopyU, *Total Internal Reflection Fluorescence (TIRF) Microscopy* **2024**, https://www.microscopyu.com/techniques/fluorescence/total-internal-reflection-fluorescence-tirf-microscopy. (Accessed June 2024)

[37] A. L. Stout, D. Axelrod, *Appl. Opt.* **1989**, *28*, 5237.

[38] Y. I. Park, K. T. Lee, Y. D. Suh, T. Hyeon, *Chem. Soc. Rev.* **2015**, *44*, 1302.

[39] A. Trache, G. A. Meininger, *Curr. Protoc. Microbiol.* **2008**, *Chapter 2*, Unit 2A.2.1–2A.2.22.

[40] K. N. Fish, *Curr. Protoc.* **2022**, *2*, e517.

[41] Janeway, C. A.; Travers, P.; Walport, M.; Shlomchik, M. J. *Immunobiology 5 the immune system in health and disease: The immune system in health and disease*, Garland Pub, New York, USA. **2001**.

[42] B. Gorovits, *The AAPS journal* **2020**, *22*, 144.

[43] H. L. Spiegelberg, *Int. Arch. Allergy Appl. Immunol.* **1989**, *90 Suppl 1*, 22.

[44] M. Reth, *Nat. Immunol.* **2013**, *14*, 765.

[45] W. Wang, S. Singh, D. L. Zeng, K. King, S. Nema, *J. Pharm. Sci.* **2007**, *96*, 1.

[46] H. M. Cooper, Y. Paterson, *Current Protocols in Neuroscience* **2009**, *Chapter 5*, Unit 5.5.

[47] V. Poláchová, M. Pastucha, Z. Mikušová, M. J. Mickert, A. Hlaváček, H. H. Gorris, P. Skládal, Z. Farka, *Nanoscale* **2019**, *11*, 8343.

[48] Z. Luo, Q. Qi, L. Zhang, R. Zeng, L. Su, D. Tang, *Anal. Chem.* **2019**, *91*, 4149.

[49] Z. Wen, X. Hu, R. Yan, W. Wang, H. Meng, Y. Song, S. Wang, X. Wang, Y. Tang, *Food Chem.* **2023**, *406*, 135081.

[50] C. A. Ascoli, B. Aggeler, *BioTechniques* **2018**, *65*, 127.

[51] Y. Gao, X. Huang, Y. Zhu, Z. Lv, *J. Immunoassay Immunochem.* **2018**, *39*, 351.

[52] H. Päkkilä, M. Ylihärsilä, S. Lahtinen, L. Hattara, N. Salminen, R. Arppe, M. Lastusaari, P. Saviranta, T. Soukka, *Anal. Chem.* **2012**, *84*, 8628.

[53] J. Máčala, E. Makhneva, A. Hlaváček, M. Kopecký, H. H. Gorris, P. Skládal, Z. Farka, *Anal. Chem.* **2024**, *96*, 10237.

[54] I. Martiskainen, S. M. Talha, K. Vuorenpää, T. Salminen, E. Juntunen, S. Chattopadhyay, D. Kumar, T. Vuorinen, K. Pettersson, N. Khanna, G. Batra, *Anal. Bioanal. Chem.* **2021**, *413*, 967.

[55] P. Holliger, P. J. Hudson, *Nat Biotechnol* **2005**, *23*, 1126.

[56] G. P. Smith, *Science.* **1985**, *228*, 1315.

[57] K. A. Charlton, *Methods in molecular biology (Clifton, N.J.)* **2004**, *248*, 245.

[58] S. S. Sidhu, *Phage Display In Biotechnology and Drug Discovery, Second Edition*, Taylor and Francis, Hoboken **2015**.

[59] H. R. Hoogenboom, *Nat. Biotechnol.* **2005**, *23*, 1105.

[60] K. Basu, E. M. Green, Y. Cheng, C. S. Craik, *Curr. Opin. Biotechnol.* **2019**, *60*, 153.

[61] K. Kuningas, T. Ukonaho, H. Päkkilä, T. Rantanen, J. Rosenberg, T. Lövgren, T. Soukka, *Anal. Chem.* **2006**, *78*, 4690.

[62] C. Drees, A. N. Raj, R. Kurre, K. B. Busch, M. Haase, J. Piehler, *Angew. Chem. Int. Ed.* **2016**, *55*, 11668.

[63] S. Song, L. Wang, J. Li, C. Fan, J. Zhao, *TrAC Trends in Analytical Chemistry* **2008**, *27*, 108.

[64] M. Kohlberger, G. Gadermaier, *Biotechnol. Appl. Biochem.* **2022**, *69*, 1771.

[65] H. Kaur, *Biochim. Biophys. Acta* **2018**, *1862*, 2323.

[66] H. Jo, C. Ban, *Exp. Mol. Med.* **2016**, *48*, e230.

[67] T. Wang, C. Chen, L. M. Larcher, R. A. Barrero, R. N. Veedu, *Biotechnol. Adv.* **2019**, *37*, 28.

[68] V. Crivianu-Gaita, M. Thompson, *Biosens. Bioelectron.* **2016**, *85*, 32.

[69] J. Yan, H. Xiong, S. Cai, N. Wen, Q. He, Y. Liu, D. Peng, Z. Liu, *Talanta* **2019**, *200*, 124.

[70] L. A. Stanciu, Q. Wei, A. K. Barui, N. Mohammad, *Annu. Rev. Biomed. Eng/* **2021**, *23*, 433.

[71] A. B. Iliuk, L. Hu, W. A. Tao, *Anal. Chem.* **2011**, *83*, 4440.

[72] A. Chen, S. Yang, *Biosens. Bioelectron.* **2015**, *71*, 230.

[73] S. Y. Toh, M. Citartan, S. C. B. Gopinath, T.-H. Tang, *Biosens. Bioelectron.* **2015**, *64*, 392.

[74] W. Xiang, Q. Lv, H. Shi, B. Xie, L. Gao, *Talanta* **2020**, *214*, 120716.

[75] Y. Wang, Z. Wei, X. Luo, Q. Wan, R. Qiu, S. Wang, *Talanta* **2019**, *195*, 33.

[76] A. Ebrahimi, H. Ravan, S. Khajouei, *TrAC Trends Anal. Chem.* **2019**, *114*, 126.

[77] V. G. Metelev, T. S. Oretskaya, *Russ. J. Bioorg. Chem.* **2021**, *47*, 339.

[78] Z. Wang, P. Wei, *Front. Immunol.* **2023**, *14*, 1331981.

[79] J. Wang, Y. Qin, S.-W. Jiang, L. Liu, Y. Lu, J. Li, L. Qiu, P. Jiang, *Sens. Actuators B: Chem.* **2016**, *237*, 106.

[80] X. Wang, D. Yang, M. Liu, D. Cao, N. He, Z. Wang, *Biosens. Bioelectron.* **2019**, *137*, 110.

[81] A. Samanta, I. L. Medintz, *Nanoscale* **2016**, *8*, 9037.

[82] M. Thaler, P. B. Luppa, *Anal. Bioanal. Chem.* **2019**, *411*, 7623.

[83] C. Zheng, K. Wang, W. Zheng, Y. Cheng, T. Li, B. Cao, Q. Jin, D. Cui, *Analyst* **2021**, *146*, 1514.

[84] P. Sang, Z. Hu, Y. Cheng, H. Yu, Y. Xie, W. Yao, Y. Guo, H. Qian, *J. Agric. Food Chem.* **2021**, *69*, 5783.

[85] K. L. Wong, J. Liu, *Biotechnol. J.* **2021**, *16*, e2000338.

[86] J. J. BelBruno, *Chem. Rev.* **2019**, *119*, 94.

[87] L. Wang, W. Ahmad, J. Wu, X. Wang, Q. Chen, Q. Ouyang, *Spectrochim. Acta. A, Mol. Biomol. Spectrosc.* **2023**, *284*, 121457.

[88] Y. Cao, X. Hu, T. Zhao, Y. Mao, G. Fang, S. Wang, *Sens. Actuators B: Chem.* **2021**, *326*, 128838.

[89] Q. Yu, C. He, Q. Li, Y. Zhou, N. Duan, S. Wu, *Microchim. Acta* **2020**, *187*, 222.

[90] J. Wackerlig, R. Schirhagl, *Anal. Chem.* **2016**, *88*, 250.

[91] S. Akgönüllü, S. Kılıç, C. Esen, A. Denizli, *Polymers* **2023**, *15*, 629.

[92] P. J. Tighe, R. R. Ryder, I. Todd, L. C. Fairclough, *Proteom. Clin. Appl.* **2015**, *9*, 406.

[93] R. M. Lequin, *Clin. Chem.* **2005**, *51*, 2415.

[94] S. Sakamoto, W. Putalun, S. Vimolmangkang, W. Phoolcharoen, Y. Shoyama, H. Tanaka, S. Morimoto, *J. Nat. Med.* **2018**, *72*, 32.

[95] *Overview of ELISA | Thermo Fisher Scientific* **2024**, https://www.thermofisher.com/de/de/home/life-science/protein-biology/protein-biology-learning-center/protein-biology-resource-library/pierce-protein-methods/overview-elisa.html#6. (Accessed September 2024)

[96] R. S. Matson, *Antibody Engineering* **2023**, *2612*, 225.

[97] J. R. Crowther, *The ELISA guidebook*, Humana Press, Totowa, NJ **2009**.

[98] T. Hasegawa, S. Shibayama, Y. Osumi, H. Sentsui, M. Kato, *Anal. Bioanal. Chem.* **2023**, *415*, 1897.

[99] N. Elahi, M. Kamali, M. H. Baghersad, *Talanta* **2018**, *184*, 537.

[100] J. Turkevich, P. C. Stevenson, J. Hillier, *Discuss. Faraday Soc.* **1951**, *11*, 55.

[101] G. FRENS, *Nat. Phys.* **1973**, *241*, 20.

[102] P. Zhao, N. Li, D. Astruc, *Coord. Chem. Rev.* **2013**, *257*, 638.

[103] W. Zhao, M. A. Brook, Y. Li, *Chembiochem* **2008**, *9*, 2363.

[104] L. Zhang, Y. Mazouzi, M. Salmain, B. Liedberg, S. Boujday, *Biosens. Bioelectron.* **2020**, *165*, 112370.

[105] M. S. Tabatabaei, R. Islam, M. Ahmed, *Anal. Chim. Acta* **2021**, *1143*, 250.

[106] R. J. Kadhim, E. H. Karsh, Z. J. Taqi, M. S. Jabir, *Mater. Today. Proc.* **2021**, *42*, 3041.

[107] N. Huang, W. Sheng, D. Bai, M. Sun, L. Ren, S. Wang, W. Zhang, Z. Jin, *Food Control* **2023**, *150*, 109759.

[108] R. E. Galian, M. d. La Guardia, *TrAC Trends Anal. Chem.* **2009**, *28*, 279.

[109] C. B. Murray, D. J. Norris, M. G. Bawendi, *J. Am. Chem. Soc.* **1993**, *115*, 8706.

[110] K. D. Wegner, N. Hildebrandt, *Chem. Soc. Rev.* **2015**, *44*, 4792.

[111] W. R. Algar, A. J. Tavares, U. J. Krull, *Anal. Chim. Acta* **2010**, *673*, 1.

[112] A. Foubert, N. V. Beloglazova, A. Rajkovic, B. Sas, A. Madder, I. Y. Goryacheva, S. de Saeger, *TrAC Trends Anal. Chem.* **2016**, *83*, 31.

[113] E. R. Goldman, I. L. Medintz, H. Mattoussi, *Anal. Bioanal. Chem.* **2006**, *384*, 560.

[114] A. M. Smith, S. Nie, *Acc. Chem. Res.* **2010**, *43*, 190.

[115] C. H. R, J. D. Schiffman, R. G. Balakrishna, *Sens. Actuators B: Chem.* **2018**, *258*, 1191.

[116] N. Jurga, D. Przybylska, P. Kamiński, A. Tymiński, B. F. Grześkowiak, T. Grzyb, *J. Colloid Interface Sci.* **2022**, *606*, 1421.

[117] C. Yan, H. Zhao, D. F. Perepichka, F. Rosei, *Small* **2016**, *12*, 3888.

[118] Y. Li, C. Chen, F. Liu, J. Liu, *Microchim. Acta* **2022**, *189*, 109.

[119] X. Chen, D. Peng, Q. Ju, F. Wang, *Chem. Soc. Rev.* **2015**, *44*, 1318.

[120] X. Zheng, R. K. Kankala, C.-G. Liu, S.-B. Wang, A.-Z. Chen, Y. Zhang, *Coord. Chem. Rev.* **2021**, *438*, 213870.

[121] J. F. Suyver, A. Aebischer, D. Biner, P. Gerner, J. Grimm, S. Heer, K. W. Krämer, C. Reinhard, H. U. Güdel, *Opt. Mater.* **2005**, *27*, 1111.

[122] F. Auzel, *Chem. Rev.* **2004**, *104*, 139.

[123] A. K. Singh, K. Kumar, A. C. Pandey, O. Parkash, S. B. Rai, D. Kumar, *Appl. Phys. B* **2011**, *104*, 1035.

[124] A. Skripka, M. Lee, X. Qi, J.-A. Pan, H. Yang, C. Lee, P. J. Schuck, B. E. Cohen, D. Jaque, E. M. Chan, *Nano Lett.* **2023**, *23*, 7100.

[125] M.-F. Joubert, S. Guy, B. Jacquier, C. Linarés, *Opt. Mater.* **1994**, *4*, 43.

[126] J. Huang, L. Yan, S. Liu, L. Tao, B. Zhou, *Mater. Horiz.* **2022**, *9*, 1167.

[127] Y. Liang, Z. Zhu, S. Qiao, X. Guo, R. Pu, H. Tang, H. Liu, H. Dong, T. Peng, L.-D. Sun, J. Widengren, Q. Zhan, *Nat. Nanotechnol.* **2022**, *17*, 524.

[128] H. Qian, T. Zhang, X. Jiang, H. Wang, W. Yang, C. Li, *J Mater Sci: Mater Electron* **2022**, *33*, 22718.

[129] M. J. V. Bell, D. F. de Sousa, S. L. de Oliveira, R. Lebullenger, A. C. Hernandes, L. A. O. Nunes, *J. Phys.: Condens. Matter* **2002**, *14*, 5651.

[130] C. Homann, L. Krukewitt, F. Frenzel, B. Grauel, C. Würth, U. Resch-Genger, M. Haase, *Angew. Chem. Int. Ed.* **2018**, *57*, 8765.

[131] *Fluorescence quantum yields (QY) and lifetimes (τ) for Alexa Fluor dyes—Table 1.5 | Thermo Fisher Scientific - DE* **2024**, https://www.thermofisher.com/de/de/home/references/molecular-probes-the-handbook/tables/fluorescence-quantum-yields-and-lifetimes-for-alexa-fluor-dyes.html. (Accessed September 2024).

[132] J. Huang, G. Wei, H. Wei, B. Zhou, *ACS Appl. Opt. Mater.* **2024**, *2*, 1841.

[133] C. Lee, E. Z. Xu, Y. Liu, A. Teitelboim, K. Yao, A. Fernandez-Bravo, A. M. Kotulska, S. H. Nam, Y. D. Suh, A. Bednarkiewicz, B. E. Cohen, E. M. Chan, P. J. Schuck, *Nature* **2021**, *589*, 230.

[134] D. N. Karimov, P. A. Demina, A. V. Koshelev, V. V. Rocheva, A. V. Sokovikov, A. N. Generalova, V. P. Zubov, E. V. Khaydukov, M. V. Koval'chuk, V. Y. Panchenko, *Nanotechnol. Russia* **2020**, *15*, 655.

[135] A. Sedlmeier, H. H. Gorris, *Chem. Soc. Rev.* **2015**, *44*, 1526.

[136] X. Zhu, J. Zhang, J. Liu, Y. Zhang, *Adv. Sci.* **2019**, *6*, 1901358.

[137] E. Hong, L. Liu, L. Bai, C. Xia, L. Gao, L. Zhang, B. Wang, *Mater. Sci. Eng. C, Mater. Biol. Appl.* **2019**, *105*, 110097.

[138] K. W. Krämer, D. Biner, G. Frei, H. U. Güdel, M. P. Hehlen, S. R. Lüthi, *Chem. Mater.* **2004**, *16*, 1244.

[139] S. Radunz, A. Schavkan, S. Wahl, C. Würth, H. R. Tschiche, M. Krumrey, U. Resch-Genger, *J. Phys. Chem. C* **2018**, *122*, 28958.

[140] Y. Jiao, C. Ling, J.-X. Wang, H. Amanico, J. Saczek, H. Wang, S. Sridhar, B. B. Xu, S. Wang, D. Wang, *Part & Part Syst Charact* **2020**, *37*.

[141] J.-C. Boyer, F. Vetrone, L. A. Cuccia, J. A. Capobianco, *J. Am. Chem. Soc.* **2006**, *128*, 7444.

[142] H. Li, X. Shi, X. Li, L. Zong, *Opt. Mater.* **2020**, *108*, 110144.

[143] M. S. Arai, A. S. S. de Camargo, *Nanoscale Adv.* **2021**, *3*, 5135.

[144] W. Kong, T. Sun, B. Chen, X. Chen, F. Ai, X. Zhu, M. Li, W. Zhang, G. Zhu, F. Wang, *Inorg. Chem.* **2017**, *56*, 872.

[145] A. Schroter, C. Del Arnau Valle, M. J. Marín, T. Hirsch, *Angew. Chem. Int. Ed.* **2023**, *62*, e202305165.

[146] Z. Zhang, S. Shikha, J. Liu, J. Zhang, Q. Mei, Y. Zhang, *Anal. Chem.* **2019**, *91*, 548.

[147] A. Drozdowski, N. Jurga, D. Przybylska, J. C. Brandmeier, Z. Farka, H. H. Gorris, T. Grzyb, *J. Colloid Interface Sci.* **2023**, *649*, 49.

[148] S. Zhang, T. Yao, S. Wang, R. Feng, L. Chen, V. Zhu, G. Hu, H. Zhang, G. Yang, *Spectrochim. Acta A Mol. Biomol. Spectrosc.* **2019**, *214*, 302.

[149] A. Hlaváček, Z. Farka, M. Hübner, V. Horňáková, D. Němeček, R. Niessner, P. Skládal, D. Knopp, H. H. Gorris, *Anal. Chem.* **2016**, *88*, 6011.

[150] S. Wu, N. Duan, Z. Wang, H. Wang, *Analyst* **2011**, *136*, 2306.

[151] S. Wu, H. Zhang, Z. Shi, N. Duan, C. Fang, S. Dai, Z. Wang, *Food Control* **2015**, *50*, 597.

[152] V. Muhr, S. Wilhelm, T. Hirsch, O. S. Wolfbeis, *Acc. Chem. Res.* **2014**, *47*, 3481.

[153] S. Wilhelm, M. Kaiser, C. Würth, J. Heiland, C. Carrillo-Carrion, V. Muhr, O. S. Wolfbeis, W. J. Parak, U. Resch-Genger, T. Hirsch, *Nanoscale* **2015**, *7*, 1403.

[154] S. F. Himmelstoß, T. Hirsch, *Part & Part Syst Charact* **2019**, *36*.

[155] S. Lahtinen, A. Lyytikäinen, N. Sirkka, H. Päkkilä, T. Soukka, *Microchim. Acta* **2018**, *185*, 220.

[156] K. Raiko, A. Lyytikäinen, M. Ekman, A. Nokelainen, S. Lahtinen, T. Soukka, *Clin. Chim. Acta.* **2021**, *523*, 380.

[157] S. Bhuckory, S. Lahtinen, N. Höysniemi, J. Guo, X. Qiu, T. Soukka, N. Hildebrandt, *Nano Lett.* **2023**, *23*, 2253.

[158] M. Hosseinifard, N. Jurga, J. C. Brandmeier, Z. Farka, A. Hlaváček, H. H. Gorris, T. Grzyb, A. Ekner-Grzyb, *Chemosphere* **2024**, *347*, 140629.

[159] L. Huang, J. Wang, S. Huang, F. Siaw-Debrah, M. Nyanzu, Q. Zhuge, *Biochem. Biophys. Res. Commun.* **2019**, *516*, 565.

[160] F. Zhang, E. Lees, F. Amin, P. Rivera Gil, F. Yang, P. Mulvaney, W. J. Parak, *Small* **2011**, *7*, 3113.

[161] B. Rezaei, A. Harun, X. Wu, P. R. Iyer, S. Mostufa, S. Ciannella, I. H. Karampelas, J. Chalmers, I. Srivastava, J. Gómez-Pastora, K. Wu, *Adv. Healthc. Mater.* **2024**.

[162] L. Shi, J. Zhang, M. Zhao, S. Tang, X. Cheng, W. Zhang, W. Li, X. Liu, H. Peng, Q. Wang, *Nanoscale* **2021**, *13*, 10748.

[163] A. N. Generalova, V. V. Rocheva, A. V. Nechaev, D. A. Khochenkov, N. V. Sholina, V. A. Semchishen, V. P. Zubov, A. V. Koroleva, B. N. Chichkov, E. V. Khaydukov, *RSC Adv.* **2016**, *6*, 30089.

[164] B. Pelaz, P. del Pino, P. Maffre, R. Hartmann, M. Gallego, S. Rivera-Fernández, J. M. de La Fuente, G. U. Nienhaus, W. J. Parak, *ACS Nano* **2015**, *9*, 6996.

[165] A. Hlaváček, Z. Farka, M. J. Mickert, U. Kostiv, J. C. Brandmeier, D. Horák, P. Skládal, F. Foret, H. H. Gorris, *Nat. Protoc.* **2022**, *17*, 1028.

[166] Y. Que, C. Feng, G. Lu, X. Huang, *ACS Appl. Mater. Interfaces.* **2017**, *9*, 14647.

[167] K. Malhotra, R. Fuku, B. Kumar, D. Hrovat, J. van Houten, P. A. E. Piunno, P. T. Gunning, U. J. Krull, *Nano Lett.* **2022**, *22*, 7285.

[168] A. Nsubuga, M. Sgarzi, K. Zarschler, M. Kubeil, R. Hübner, R. Steudtner, B. Graham, T. Joshi, H. Stephan, *Dalton Trans.* **2018**, *47*, 8595.

[169] U. Kostiv, Z. Farka, M. J. Mickert, H. H. Gorris, N. Velychkivska, O. Pop-Georgievski, M. Pastucha, E. Odstrčilíková, P. Skládal, D. Horák, *Biomacromolecules* **2020**, *21*, 4502.

[170] B. Stump, *Chembiochem.* **2022**, *23*, e202200016.

[171] D. Lisjak, M. Vozlič, U. Kostiv, D. Horák, B. Majaron, S. Kralj, I. Zajc, L. Žiberna, M. Ponikvar-Svet, *Methods Appl. Fluoresc.* **2021**, *10*.

[172] S. P. Pujari, L. Scheres, A. T. M. Marcelis, H. Zuilhof, *Angew. Chem. Int. Ed.* **2014**, *53*, 6322.

[173] Z. Meng, Y. Wu, J. Ren, X. Li, S. Zhang, S. Wu, *ACS Appl. Mater. Interfaces*. **2022**, *14*, 12562.

6 Article I

Effect of particle size and surface chemistry of photon upconversion nanoparticles on analog and digital immunoassays for cardiac troponin

Julian C. Brandmeier, Kirsti Raiko, Zdeněk Farka, Riikka Peltomaa,
Matthias J. Mickert, Antonín Hlaváček, Petr Skládal, Tero Soukka, Hans H. Gorris

Reproduced with permission from:
Advanced Healthcare Materials **2021**,*10*, e2100506.

6.1 Abstract

Sensitive immunoassays are required for troponin, a low-abundance cardiac biomarker in blood. In contrast to conventional (analog) assays that measure the integrated signal of thousands of molecules, digital assays are based on counting individual biomarker molecules. Photon-upconversion nanoparticles (UCNP) are an excellent nanomaterial for labeling and detecting single biomarker molecules because their unique anti-Stokes emission avoids optical interference, and single nanoparticles can be reliably distinguished from the background signal. Here, the effect of the surface architecture and size of UCNP labels on the performance of upconversion-linked immunosorbent assays (ULISA) is critically assessed. The size, brightness, and surface architecture of UCNP labels are more important for measuring low troponin concentrations in human plasma than changing from an analog to a digital detection mode. Both detection modes result approximately in the same assay sensitivity, reaching a limit of detection (LOD) of 10 pg mL^{-1} in plasma, which is in the range of troponin concentrations found in the blood of healthy individuals.

6.2 Introduction

Heart diseases such as acute myocardial infarction (AMI) are the leading cause of death worldwide.[1] Since there is only a limited time available from the onset of the symptoms to lifesaving treatment, fast and reliable diagnostic tests are essential. In healthy individuals, cardiac troponin (cTn) is located exclusively in myocardial tissue. Therefore, several clinical tests have been employed to measure elevated levels of cTn—the recommended biomarker for AMI—in blood for the early diagnosis of AMI.[2] cTn is a heterotrimeric complex consisting of cTnI, cTnT, and TnC.[3,4] The subunits cTnI and cTnT exist as unique, recognizable isoforms only in the heart muscle (myocardium) and are released into the blood during AMI.[5,6] Highly sensitive, precise, and specific troponin tests are required to discriminate between low cTnI levels in blood and background noise.[7] Commercial chemiluminescence, electrochemical, or fluorescence assays in clinical use[8] reach limits of detection (LOD) in the range of 0.08–2.7 pg mL^{-1}.[9] According to the European Society of Cardiology and the American College of Cardiology, increased cTnI or cTnT levels in blood are defined as the value above the 99th percentile concentration of a healthy reference population, which varies typically between 8.67 and 60.4 pg mL^{-1}.[10,11]

Nevertheless, cTnI is a challenging analyte for immunochemical detection, and quantitative measurements can be influenced by several factors, such as the availability of epitopes for antibody binding. Due to the proteolytic susceptibility of the N- and C-terminal parts of cTnI,[12] antibodies for cTnI assays are often selected to recognize epitopes in the stable central part.[13,14] Furthermore, since cTnI in the blood is mainly present as a binary cTnI–TnC complex,[8] the antibodies should recognize both the free and complexed forms of cTnI. Moreover, phosphorylation or blocking of the epitopes by autoantibodies or heterophile antibodies may hinder the antibody recognition.[15] As it is unlikely that a single antibody pair is not affected by some kind of cTnI modifications or interferences,[16] many cTnI assays use a combination of two capture or two detection antibodies.[9] Furthermore, troponin assays often suffer not only from a low working range but also from rather poor precision at concentrations below the 99th percentile.[17] The choice of signal-generating labels is of a paramount importance to improve the assay reliability and performance.

Photon-upconversion nanoparticles (UCNP) represent lanthanide-doped luminescent labels emitting shorter-wavelength light under near-infrared excitation (anti-Stokes emission), which strongly reduces background interference because of autofluorescence and light scattering.[18,19] Due to these remarkable optical properties, UCNPs are excellent labels for upconversion-linked immunosorbent assays (ULISA).[20–22] The hydrophobic layer of oleic acid on pristine UCNPs needs to be replaced by a hydrophilic coating to render the UCNPs dispersible in aqueous media and allow further bioconjugation. Alkyne-poly(ethylene glycol) (PEG) conjugated to neridronate, a bisphosphonate, has been shown to strongly coordinate to surface lanthanide ions of UCNPs. The alkyne group reacts with azide-modified streptavidin *via* click-chemistry.[23,24] Alternatively, surface coating with hydrophilic poly(acrylic acid) (PAA) yields water-dispersible nanoparticles with excellent colloidal stability and high density of surface carboxyl groups for bioconjugation via EDC/NHS activation.[25]

Furthermore, the absence of optical background interferences enables the detection and counting of individual UCNP labels using wide-field optical microscopy.[19,26] This has led to the development of single-molecule (digital) immunoassays,[27] as opposed to analog immunoassays where the integrated signal generated by thousands of labels is measured. It is essential that the UCNP labels have the right size and are bright enough to be reliably detectable (and countable) at the single-nanoparticle level. If this condition is met, the digital assay is essentially independent of varying particle brightness, particle aggregation, and the instrumental background. With high-affinity detection antibodies, the LOD is limited by (1) the standard deviation of the nonspecifically bound labels in the control sample without analyte, and (2) counting statistics, as the precision of the measurement depends on the number of counted events (Poisson noise).

We previously developed a digital ULISA with PEG-neridronate-based UCNP labels for the detection of prostate-specific antigen (PSA).[19,26] The digital readout yielded an LOD of 0.023 pg mL^{-1}, which was 20-fold more sensitive than the analog readout. In another study, we applied PAA-coated UCNPs to the detection of cTnI in the analog mode, which resulted in an LOD of 0.48 pg mL^{-1}.[28,29] Here, we employ both surface modification strategies for UCNPs and critically assess the effect of the UCNP label size on the performance of the analog and digital immunoassay for cTnI. The schemes of the sandwich ULISAs using either type of label are shown in Figure 1.

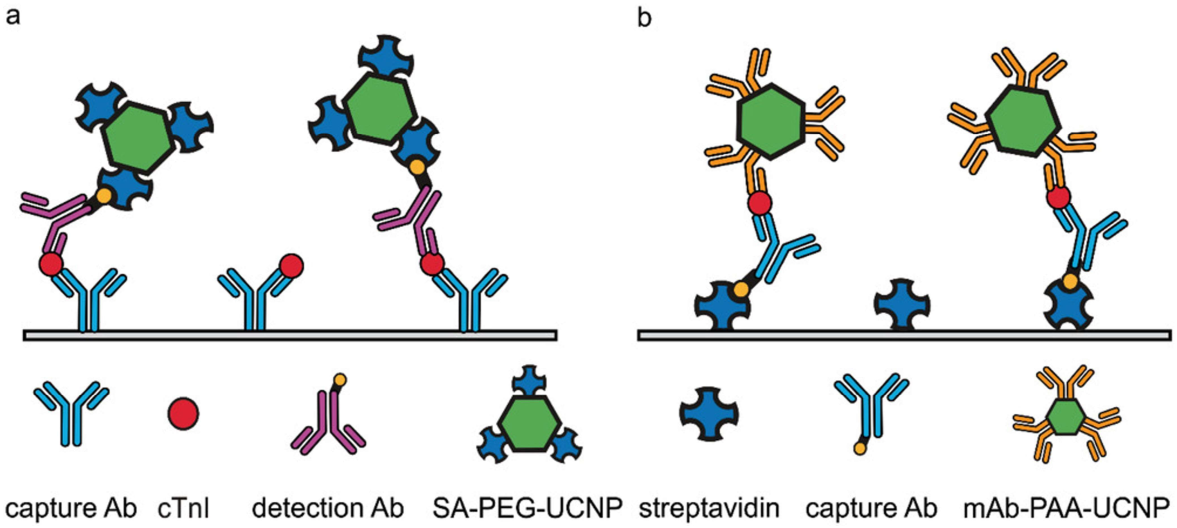

Figure 1*. ULISA configurations for the detection of cardiac troponin (cTnI). a) SA-PEG-UCNP label: A microtiter well is coated with monoclonal mouse anti-cTnI antibodies to capture cTnI. The biotinylated anti-cTnI antibody binds to cTnI and forms a sandwich immunocomplex, which is detected using SA-PEG-UCNP labels. b) mAb-PAA-UCNP label: A microtiter well is coated with streptavidin to immobilize biotinylated anti-cTnI antibodies, which capture cTnI. Finally, mAb-UCNP conjugates bind to cTnI and form a sandwich immunocomplex.*

6.3 Experimental section

6.3.1 Chemicals and reagents

A complete list of chemicals and the preparation of alkyne-PEG-neridronate (Alkyne-PEG-Ner) and the streptavidin-azide are provided in the Supporting Information. The cTn I-T-C complex, and monoclonal anti-cTnI-antibody (mAb) clones 19C7cc, MF4cc, 560cc, and 625cc were purchased from Hytest (Turku, Finland). The mAbs 560cc and 625cc were biotinylated as described in the Supporting Information and mAb 19C7 as previously published.[30] The recombinant anti-cTnI F_{ab} fragment 9707 was cloned from a hybridoma cell line of Medix Biochemica (Espoo, Finland) and produced and site-specifically biotinylated as described previously.[31] Blood for the plasma pool from five anonymized healthy volunteers was collected in lithium-heparin vacuum tubes (BD Vacutainer 10 mL, Plymouth, UK). Volunteers provided written informed consent regarding the use of collected plasma samples according to the principles expressed in the Declaration of Helsinki. Plasma was stored at −20 °C, and the aliquots were freshly thawed and centrifuged for 5 min at 1000 *g* before each experiment. The STAT troponin I test (Abbot, Chicago, IL, USA) was used to determine the intrinsic cTnI concentration in plasma.

The buffers were prepared using double-distilled water and filtered through a 0.22-μm membrane (Magna Nylon, GVS, USA). The buffers for the dilution of reagents included phosphate buffer (PB; 50×10^{-3} M NaH_2PO_4/Na_2HPO_4, pH 7.4), phosphate-buffered saline (PBS; PB with 150×10^{-3} M NaCl), Tris-buffered saline (TBS; 50×10^{-3} M Tris, 150×10^{-3} M NaCl, pH 7.5). Coating buffer consisted of 50×10^{-3} M $NaHCO_3/Na_2CO_3$, 0.05% NaN_3, pH 9.6. Two types of washing buffers were employed: Kaivogen-washing buffer and Tris-washing buffer (50×10^{-3} M Tris, 5×10^{-3} M $CaCl_2$, 0.05% Tween 20, pH 7.5). Several assay buffer combinations were investigated: (1) SuperBlock buffer (10% SuperBlock in TBS, 1×10^{-3} M KF, 0.05% Tween 20, 0.05% PEG, and 0.05% NaN_3, pH 7.5), (2) SuperBlock buffer with 5×10^{-3} M $CaCl_2$ (SuperBlock-Ca), (3) Kaivogen assay buffer, (4) modified Kaivogen assay buffer (assay buffer including 0.05% PAA (M_W 1200 Da), 1×10^{-3} M KF, 0.2% milk powder, 0.08% native mouse IgG, 0.005% denatured mouse IgG, pH 8.0), (5) BSA/BGG buffer (37.5×10^{-3} M Tris, 513×10^{-3} M NaCl, 5% D-trehalose, 2.5% BSA, 0.06% BGG, 0.04% NaN_3, pH 8.6), and (6) BSA/BGG/IgG buffer (37.5×10^{-3} M Tris, 500×10^{-3} M NaCl, 5% D-trehalose, 2.5% BSA, 0.06% BGG, 0.08% native mouse IgG, 0.005% denatured mouse IgG, 0.2% casein, 37.5 U mL^{-1} heparin, 0.0375% NaN_3, pH 7.75). Calibrator dilutions were prepared in 7.5% BSA/TSA (50×10^{-3} M Tris, pH 7.75, 150×10^{-3} M NaCl and 0.05% NaN_3, with 7.5% BSA).

6.3.2 Preparation of and characterization of UCNP labels

6.3.2.1 SA-PEG-UCNP conjugates

For the preparation of SA-PEG-UCNP labels, UCNPs ($NaYF_4$:Yb,Er, 63 nm in diameter) were synthesized as described in the Supporting Information. The UCNPs (10 mg, 311 μL) dispersed in cyclohexane were mixed with an equal volume of 200×10^{-3} M HCl and incubated for 30 min at 38 °C under shaking and an additional 15 min of sonication to remove the oleic acid from the UCNP surface and mediate a phase transfer from cyclohexane to water. The lower HCl phase was added to an excess of acetone and centrifuged (1000 *g*, 20 min) to precipitate the UCNPs. The UCNP pellet was redispersed in 500 µL of water, sonicated for 5 min, and 2 mg of the Alkyne-PEG-Ner linker dissolved in 500 µL of water were added and incubated overnight at 38 °C under shaking. The Alkyne-PEG-Ner-UCNP conjugates were dialyzed for 72 h in a Float-A-Lyzer G2 dialysis device (100 kDa M_W cut-off; Fisher Scientific) at 4 °C against 4 L of 1×10^{-3} M KF in water, which was exchanged nine times.

For the functionalization with streptavidin, 100 µL of Tris-HCl (375×10^{-3} M, pH 7.5) and an aqueous solution of sodium ascorbate (20 µL, 100×10^{-3} M) were added to 10 mg of Alkyne-PEG-Ner-UCNPs in 1.4 mL of water. After purging the mixture for 45 min with argon, 100 µL of streptavidin-azide (1 mg mL^{-1} in water) were added, and the mixture was purged for another 10 min. Adding 10 µL of an aqueous solution of 25×10^{-3} M $CuSO_4$ initiated the click reaction. The suspension was purged for 40 min with argon and then dialyzed in a Float-A-Lyzer G2 dialysis device (100 kDa M_W cut-off) against 4 L of dialysis buffer (50×10^{-3} M Tris, 0.05% NaN_3, 1×10^{-3} M KF, pH 7.5 at 4 °C for 72 h), which was exchanged nine times.[32]

6.3.2.2 *mAb-PAA-UCNP conjugates*

For the preparation of mAb-PAA-UCNP labels, oleic acid-capped UCNPs ($NaYF_4$:Yb,Er; 40, 48, 56, 64, and 80 nm in diameter) were obtained from Kaivogen. The oleic acid was removed and replaced with PAA in a two-step ligand exchange with $NOBF_4$, as described previously.[33] The UCNPs (25 mg) dispersed in cyclohexane were mixed with an equal volume of dimethylformamide (DMF). The suspension was sonicated for 1 min, added to 25 mg of $NOBF_4$ and vortexed vigorously. During the following 60 min under shaking (1200 rpm), oleic acid on the nanoparticle surface was replaced by BF_4^-, which mediated a phase transfer from cyclohexane to DMF. The UCNP dispersion was split into two aliquots and the particles were precipitated by adding a fourfold volume excess of chloroform to the dispersion in DMF. The UCNPs were washed four times by alternating precipitation with chloroform and centrifugation (11 000 *g*, 5 min) followed by redispersion in 200 µL of DMF. The UCNP pellet was resuspended in 150 µL DMF, centrifuged (2500 *g*, 3 min) to remove possible larger aggregates, and the supernatant was transferred to a fresh tube. The yield of UCNPs coated with BF_4^- was determined by comparing the luminescence of the solution to that of 10 mg mL^{-1} UCNP standard, both diluted 200 times in 10 × 10^{-3} M $B_4Na_2O_7$, pH 8 with 0.1% Tween-20).

The DMF dispersion of BF_4^--coated UCNPs was mixed with a 10% solution of poly(acrylic acid) (PAA, M_w 2000) in water (adjusted to pH 9 by NaOH) such that a twofold mass excess of PAA compared to UCNPs was obtained. The mixture was further diluted with DMF to yield a PAA concentration of 3.3% and incubated for 24 h at 60 °C under shaking (1400 rpm). The PAA-coated UCNPs were washed three times by centrifugation (20 000 *g*, 15 min) and resuspended twice in 1 mL of water and finally in 1 mL of sodium borate buffer (50 × 10^{-3} M H_3BO_3 with NaOH, pH 8.0). This suspension was centrifuged once more at lower speed (2500 *g*, 3 min) to sediment possible larger aggregates. The supernatant was carefully collected and stored at room temperature (RT) until further use.

The conjugation of mAb 625cc and mAb 560cc was adapted from a previously published protocol[28] and all steps were performed at RT. A dispersion of 250 μL of PAA-coated UCNPs (2 mg) in 20 × 10^{-3} M aqueous MES buffer (pH 6.1) was activated using 20 × 10^{-3} M EDC and 30 × 10^{-3} M sulfo-NHS for 45 min under shaking. The UCNPs were washed by two centrifugation steps (20 000 *g*, 7 min), the initial one followed by resuspension in 335 μL and the second in 210 μL of 20 × 10^{-3} M MES buffer. 40 μL of mAbs solution in 0.9% NaCl was added to yield a final antibody concentration of 0.33 mg mL^{-1} in a total volume of 250 μL. After 2.5 h under rotation, an aqueous solution of 2 M 2-amino-*N*,*N*-dimethylacetamide (ADMA) in water (pH 11) was added to yield a final ADMA concentration of 50 × 10^{-3} M. The mixture was rotated for 30 min to terminate the conjugation reaction and block the nanoparticle surface. After washing twice by centrifugation (20 000 *g*, 10 min) and resuspension in 500 μL of Tris-buffer (10 × 10^{-3} M Tris, 0.1% Tween 20, pH 8), the antibody-conjugated UCNPs (mAb-PAA-UCNPs) were resuspended in 5 × 10^{-3} M Tris, pH 8.5, 0.05% Tween 85, 0.5% BSA, 0.05% NaN_3, pH 8.5, and stored at 4 ℃.

6.3.2.3 Characterization of UCNP labels

The UCNPs and their conjugates were characterized using transmission electron microscopy (TEM), dynamic light scattering (DLS), and upconversion emission spectroscopy as described in Figures S1–S3 in the Supporting Information.

6.3.3 ULISA

6.3.3.1 SA-PEG-UCNP labels

A high-binding 96-well microtiter plate (µClear with 190-µm-thick bottom foil for microscope detection, Greiner, Austria) was coated with 60 µL of two monoclonal anti-cTnI antibodies (19C7cc and MF4cc, each 50 ng/well) in coating buffer overnight at 4 °C. The following steps were carried out at RT. The plate was washed twice with 250 µL of Tris-washing buffer and blocked for 1 h with 175 µL of SuperBlock buffer. After two washing steps, the cTn I-T-C complex was serially diluted in 60 µL of either BSA/BGG buffer alone, or 20% human plasma in BSA/BGG buffer and incubated for 1 h. The microtiter plate was washed twice and incubated for 1 h with 60 µL of a mixture containing biotinylated anti-cTnI antibodies (560cc and 625cc; each 0.5 µg mL^{-1}) in SuperBlock-Ca buffer. After two washing steps, the plate was incubated with 60 µL of SA-PEG-UCNPs (6.5 µg mL^{-1}) for 1 h in SuperBlock-Ca buffer. After two washing steps, the plate was left to dry on air.

6.3.3.2 mAb-PAA-UCNP labels

All steps were carried out at RT. The mAb-PAA-UCNP labels were diluted 30 min before starting the assay in modified Kaivogen assay buffer to a final concentration of either 4 µg mL^{-1} of mAb625-PAA-UCNP alone, or 2 µg mL^{-1} of each label in a mixture of mAb625-PAA-UCNP and mAb560cc-PAA-UCNP.

A high-binding 96-well microtiter plate (µClear with 190-µm-thick bottom foil for microscope detection, Greiner) was coated with streptavidin as described earlier.[34] The plates were first washed with Kaivogen washing buffer. Then, 50 µL of biotinylated mAb 19C7cc (150 ng/well) and F_{ab} 9707 (50 ng/well) in Kaivogen assay buffer were added and incubated for 30 min under shaking. After one washing step, the cTn I-T-C complex was serially diluted in 50 µL/well in 7.5% BSA/TSA or human plasma, respectively, followed by further dilution to 20% in BSA/BGG/IgG buffer, and incubated for 30 min. After one washing step, the mAb-PAA-UCNP labels prepared prior to the assay were sonicated 3× for 0.5 s with 100% amplitude using a VialTweeter (Hielscher Ultrasonics, Teltow, Germany) and added to the microtiter plate (50 µL/well). After 15 min, the microtiter plate was washed four times and left to dry on air.

6.3.4 Signal acquisition and statistical analysis

6.3.4.1 Analog readout

A modified upconversion microtiter plate reader (Chameleon, Hidex, Turku, Finland) equipped with a 980-nm laser excitation source[35] was used for measuring the integrated emission of Er-doped UCNPs at 540 nm. (1) In the case of SA-PEG-UCNP labels, 64 points were scanned in each well with a distance of 100 µm and a signal integration time 1 s. Afterwards, the 16 highest and 16 lowest values were discarded, and the mean value was calculated, providing the truncated average of the intensity in a single well. (2) In the case of mAb-PAA-UCNP labels, the bottom surface of the microtiter plate wells was scanned using a 3 × 3 raster with 1.5 mm step size and an exposure time of 2 s and the average intensity per well was calculated. The plotted averages and standard deviations (mean ± SD) were determined from three independent wells. The data was fitted by a four-parameter logistic function using the software Origin 2020 (OriginLab, USA). The LODs were obtained by adding three times the standard deviation of the background to the baseline values of the regression curve.[26]

6.3.4.2 Digital readout

An inverted wide-field epifluorescence microscope (Eclipse Ti, Nikon, Japan) was connected to a continuous-wave 980-nm laser diode (4 W, Wavespectrum, China) via a multimode optical fiber (105 µm fiber core, 0.22 NA, Wavespectrum) and a motorized TIRF/Epifluorescence illuminator unit (Eclipse Ti-E, Nikon, Japan). The filter cube for the detection of Er^{3+}-doped UCNPs consisted of a long-pass excitation filter ($\lambda_{\text{cut-on}}$ = 830 nm, Schott, Germany), a dichroic mirror ($\lambda_{\text{cut-on}}$ = 875 nm, AHF Analysentechnik, Germany), and a band-pass filter (λ = 535 ± 70 nm, $OD_{980} \approx 6$, Chroma, USA). The images were acquired on an sCMOS camera (5.5 megapixel, Neo, Andor Technology, UK) and a 100× objective (1.49 NA, CFI HP Apochromat TIRF, Nikon), which resulted in a power density of 640 W cm^{-2}.

The dry microtiter plate wells were filled with 80 µL of glycerol for heat dissipation of the NIR laser beam. The software NIS Elements 4.5 (Nikon) was used for the acquisition of 9 wide-field images per well with an imaging area of 166 × 144 µm^2 and exposure times between 10 and 30 s (depending on the size—and thus brightness—of the UCNPs)[19] and for the counting of individual UCNPs. The total number of UCNPs per well (*n* = 3) was analyzed using a four-parameter logistic function in Origin 2020. The LODs were obtained by adding three times the standard deviation of the background to the baseline values of the regression curve.[26]

6.4 Results and discussion

6.4.1 Optimization of antibody combination and ULISA configuration

cTnI is a very fragile analyte prone to proteolytic degradation, phosphorylation, or complexing with other proteins and autoantibodies.[16,36–38] As these factors are not relevant when cTnI is present in well-defined buffers, it is necessary to assess the detectability of cTnI in its physiological environment, where many different enzymes, troponins, and other proteins are present in varying concentrations. Therefore, we prepared a plasma pool from five healthy volunteers and determined the intrinsic cTnI concentration using a commercial test (28.8 pg mL^{-1}) to distinguish it from spiked troponin concentrations.

The immunoassay performance further depends on the careful selection of antibodies and the assay configuration. We first coated the capture antibodies mAb 19C7cc and MF4cc directly on the microtiter plate surface (**Figure 1a**). cTnI was then detected using biotinylated detection antibodies and SA-PEG-UCNP labels. When comparing the biotinylated detection antibodies mAb 560cc, mAb 625cc, and a combination of both, mAb 625cc alone was sufficient to achieve the highest sensitivity (Figure S4a, Supporting Information). **Figure 2** shows the calibration curves of cTnI either prepared in BSA/BGG buffer or in 20% plasma and then diluted in BSA/BGG buffer. The LODs of the assay were 41 pg mL^{-1} in BSA/BGG buffer (corresponding to 120 pg mL^{-1} in undiluted sample) and 30 pg mL^{-1} in 20% human plasma (corresponding to 80 pg mL^{-1} in undiluted sample). The only difference between the calibration curves is the slightly lower background (bg) signal as a result of blocking effects of serum proteins, which has a positive effect on the LOD measured in plasma samples. The assay, however, shows no cross-reactivity towards other proteins in plasma, which would have increased the background signal.

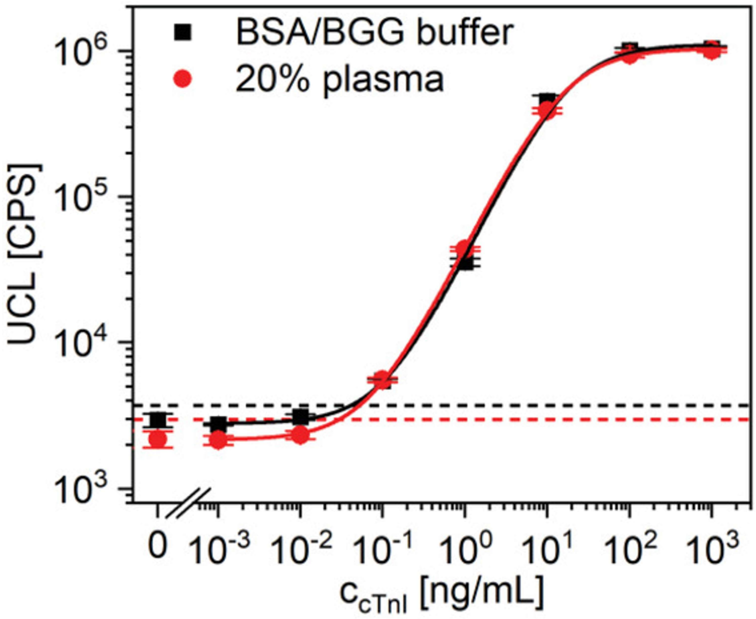

Figure 2. *Calibration curves of the analog ULISA using biotinylated mAb 560cc and SA-PEG-UCNP labels. cTnI was serially diluted in either BSA/BGG buffer (LOD: 41 pg mL^{-1}; bg: 3000 CPS), or first in 20% plasma and then in BSA/BGG buffer (LOD: 30 pg mL^{-1}; bg: 2200 CPS). The error bars show the standard deviation of three replicate measurements (mean ± SD, n = 3). The hatched lines indicate the LODs.*

Calibration curves of the analog ULISA using biotinylated mAb 560cc and SA-PEG-UCNP labels. cTnI was serially diluted in either BSA/BGG buffer (LOD: 41 pg mL^{-1}; bg: 3000 CPS), or first in 20% plasma and then in BSA/BGG buffer (LOD: 30 pg mL^{-1}; bg: 2200 CPS). The error bars show the standard deviation of three replicate measurements (mean ± SD, *n* = 3). The hatched lines indicate the LODs.

In the second assay configuration (**Figure 1b**), we used streptavidin for coating the microtiter plate surface. Independent of a partial denaturation during the adsorption-based surface attachment, at least one of the four high-affinity binding sites of streptavidin is usually available for binding of biotin. At the same time, the streptavidin layer affords the right orientation of the biotinylated antibody. This is especially important for binding of small biotinylated F_{ab} fragments, which may lose their activity through denaturation after direct adsorption-based surface attachment. In this configuration, we employed a combination of biotinylated F_{ab} 9707 and biotinylated mAb 19C7cc. The smaller size of the F_{ab} fragment enhanced the epitope availability for the detection antibody.[12] On the detection side, two types of mAb-PAA-UCNP labels were compared, one carrying mAb 560cc on the nanoparticle surface and the other mAb 625cc. A combination of both antibody conjugates was also investigated. The LOD was rather independent of the label type in the buffer (**Figure S4**, Supporting Information), but mAb 625cc-PAA-UCNP resulted in a higher sensitivity in plasma (data not shown) and thus was used for further experiments.

6.4.2 Effect of UCNP label size

The size of the UCNP-based detection label is another important parameter influencing the immunoassay performance. On the one hand, the size should be small to (1) obtain stable nanoparticle dispersions, (2) reduce nonspecific binding, and (3) minimize their influence on the antibody–antigen interaction. On the other hand, a larger size of UCNPs strongly increases their brightness such that they can be more easily detected. The brightness is particularly important for the detection of the labels at the single-nanoparticle level. Therefore, we conjugated UCNPs of 40, 48, 56, 64, and 80 nm in diameter to mAb 625cc and used them as labels for the detection of cTnI in buffer (**Figure 3a**) and in human plasma (**Figure 3b**).

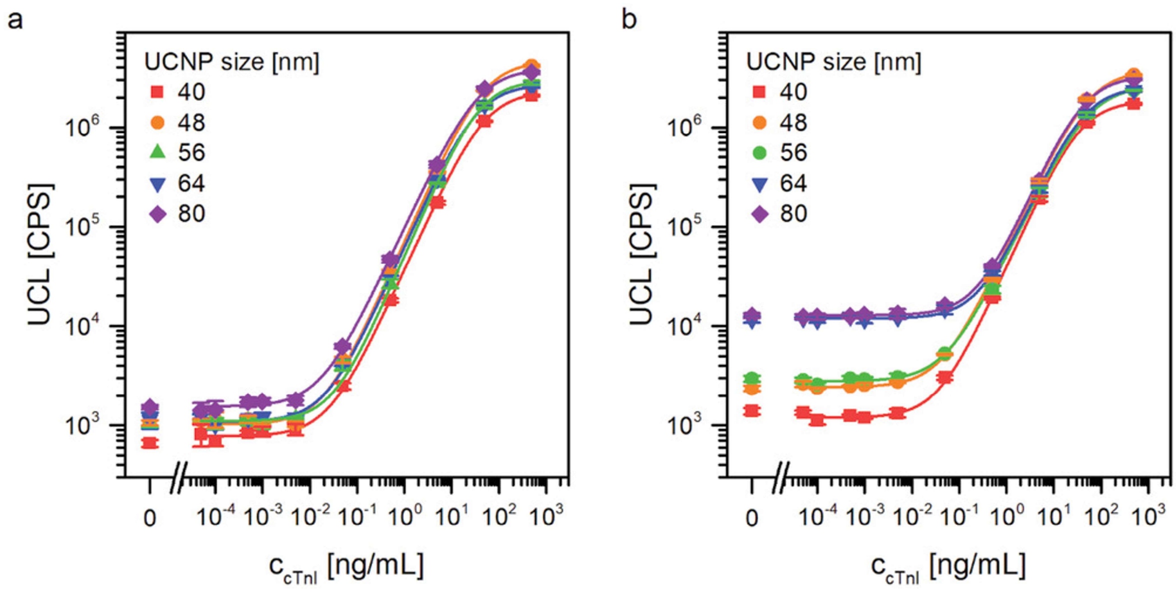

Figure 3. *Analog ULISA for the detection of cTnI using different sizes of UCNP-PAA conjugated to mAb 625cc in a) buffer and b) 20% plasma. The error bars show standard deviations of replicate measurements in three wells (mean ± SD, n = 3).*

While the background signal of mAb-PAA-UCNP labels in BSA/BGG/IgG buffer was in general lower (<2000 CPS) than for the SA-PEG-UCNP labels in buffer and only increased slightly with the label size (see **Table 1** for a detailed comparison), the use of plasma resulted in a ten times higher background signal when the label size increased from 40 to 80 nm. Also, a comparison among the same label sizes showed that the background was 2–20 times higher in plasma than in the buffer. Therefore, the higher background signal of larger UCNP labels cannot be simply explained by a higher brightness of larger UCNPs, but is rather a consequence of plasma components leading to a higher level of nonspecific binding of the larger particles to the microtiter plate. The higher LOD of the ULISA with larger UCNP labels in plasma can be attributed to the higher background signal. The origin of the increased tendency to nonspecific binding of the larger UCNPs may be related to the larger contact area (affected also by the shape of the nanoparticles) with the surface, which may lead a larger number of simultaneous weak interactions.

***Table 1**. Summary of the analog and digital detection of cTnI in buffer and in human plasma using mAb-PAA-UCNP labels.*

Detection of cTnI	**in buffer**				**in plasma**			
	analog		digital		analog		digital	
UCNP size[a] [nm]	background signal (CPS)	LOD [pg mL^{-1}]	number of UCNPs[b]	LOD [pg mL^{-1}]	background signal (CPS)	LOD [pg mL^{-1}]	number of UCNPs[b]	LOD [pg mL^{-1}]
40	658	6.0	*n.d.*[c]	*n.d.*[c]	1387	11.9	*n.d.*[c]	*n.d.*[c]
48	1055	3.8	33	3.3	2622	8.6	105	9.8
56	1038	8.3	21	7.0	2958	11.8	74	65.2
64	1129	13.3	15	17.4	11 211	57.2	209	17.2
80	1517	2.9	15	4.7	12 716	44.9	153	160.0

[a] *Average UCNP diameter determined by TEM (**Figure S1**, Supporting Information);*

[b] *Number of luminescent spots in the background images (0.2 mm^2). Average of 3 wells calculated from the sum of 9 images per well;*

[c] *Not determinable because smaller UCNPs are not bright enough for single-nanoparticle detection.*

6.4.3 Performance of digital assays

In our previous work on PSA,[26] we observed that counting single immunocomplexes (digital mode, LOD: 0.02 pg mL^{-1}) resulted in a 20-fold higher sensitivity than the analog mode (LOD: 0.4 pg mL^{-1}) using SA-PEG-UCNP detection labels in the same configuration as shown in **Figure 1a**. We explained the higher sensitivity of the digital mode by the reduced influence of label aggregation in the digital mode, where each aggregate—independent of its size—is counted only as a single binding event. In the analog mode, by contrast, an aggregate bound nonspecifically to the microtiter plate surface can strongly increase the background signal depending on the number of UCNPs in the aggregate.

In our current work, the same microtiter plates prepared for the analog detection of troponin were used for counting individual cTnI immunocomplexes under the upconversion microscope to determine the concentration in the digital mode. **Figure 4** shows microscope images of single immune complexes labeled with mAb-PAA-UCNPs (56 nm; images of other mAb-PAA-UCNP sizes and SA-PEG-UCNPs are shown in **Figures S5** and **S6** in the Supporting Information). A minimal size of 48 nm was required for a reliable detection at the single-nanoparticle level. In both buffer and plasma, the distribution of the label brightness was relatively uniform among different types and sizes of labels (**Table S1**, Supporting Information), indicating that the number of aggregates present in the label samples was relatively small.

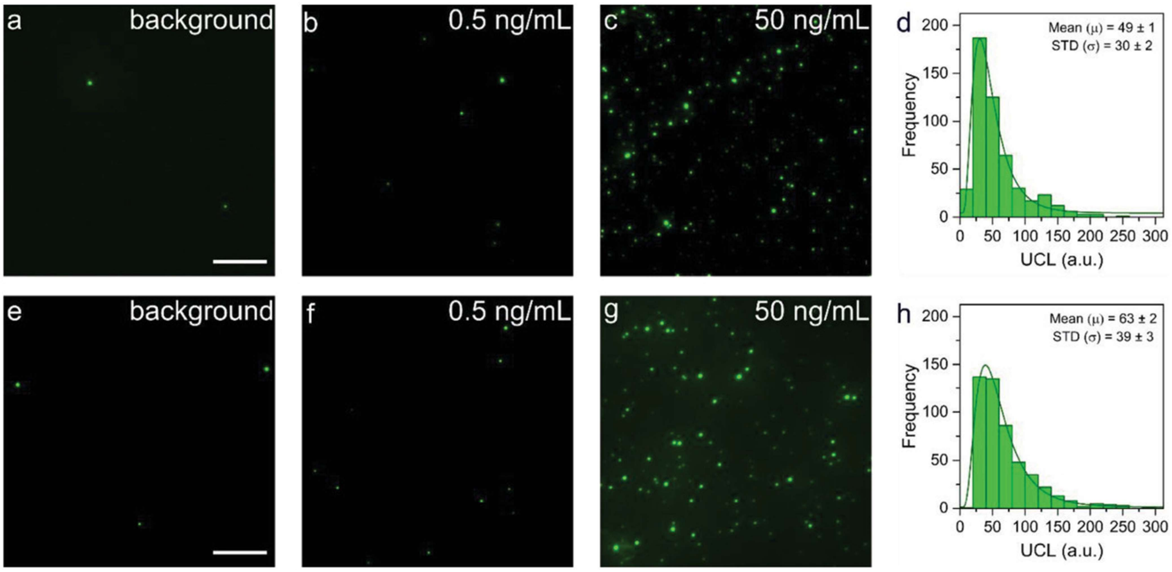

***Figure 4**. Digital ULISA for the detection of troponin using mAb-PAA-UCNP labels (56 nm in diameter). a–c) Wide-field upconversion microscopy images corresponding to serial dilutions of cTnI in BSA/BGG/IgG buffer. d) Brightness distribution histogram of 500 diffraction-limited spots recorded at 50 ng mL^{-1} of cTnI. e–g) Wide-field upconversion microscopy images corresponding to serial cTnI dilutions in plasma. d) Brightness distribution histogram of 500 diffraction-limited spots recorded at 50 ng mL^{-1} of cTnI in plasma. Scale bar: 10 µm.*

The calibration curves of the digital assays are summarized in **Figure 5**. In contrast to the analog readout (**Figure 3**), the number of nonspecifically bound labels was relatively independent of the label size in BSA/BGG/IgG buffer and in plasma (**Figure 5**, **Table 1**). While most of the increased background is a result of more nonspecific binding events in plasma, it should be noted that in the case of small nanoparticles, also the average brightness per diffraction-limited spot increased, which indicates that the plasma has an indirect effect on the label aggregation (**Table S1**, Supporting Information). As the background mainly determines the assay sensitivity, the sensitivity of the digital detection in buffer was relatively similar among the different label sizes. By contrast, the assay sensitivity decreased in plasma when using larger labels, with exception of the 64-nm conjugates.

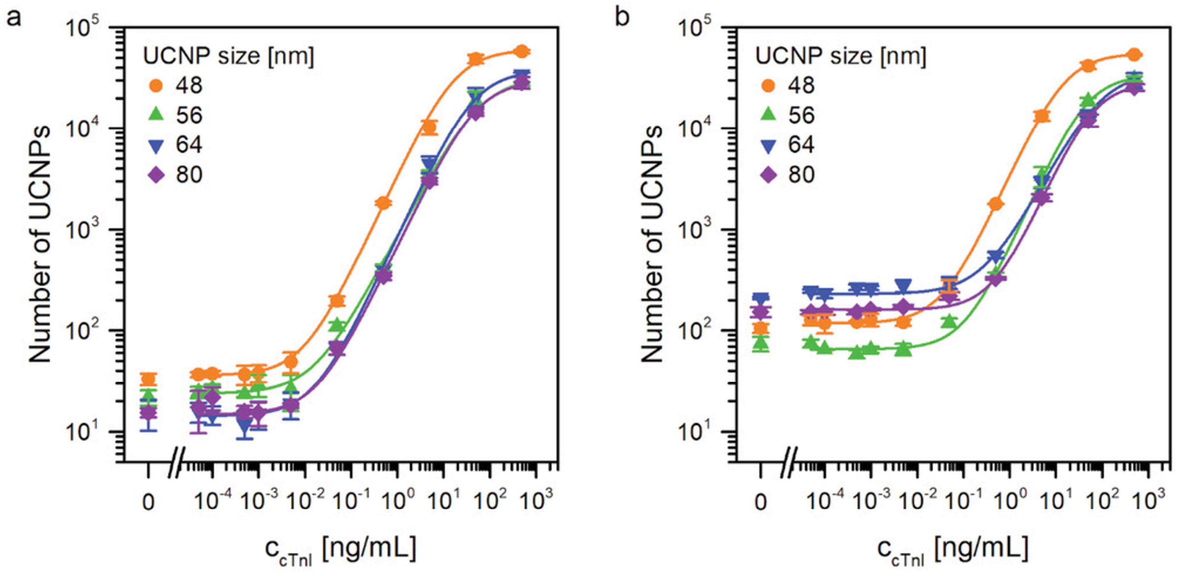

Figure 5. *Digital ULISA for the detection of troponin using different sizes of mAb 625cc-PAA-UCNP labels in a) BSA/BGG/IgG buffer and b) 20% plasma. The error bars show the standard deviation of replicate measurements in three wells (mean ± SD, n = 3).*

We also compared the assay performance in the digital mode using SA-PEG-UCNP labels (**Figure S7**, Supporting Information), but these labels did not improve the LOD compared to the analog readout (**Figure 2**), either. Therefore, independent of the assay configuration and the type and size of the label, the analog and digital readout resulted in similar LODs. The number of nonspecifically bound mAb-PAA-UCNP labels in the background image of the blank sample (**Figure 5a**) was about ten times lower than the number of nonspecifically bound SA-PEG-UCNP labels (**Figure S7**, Supporting Information), which was consistent with our earlier PSA experiments using SA-PEG-UCNP labels.[26] The lower number of counting events (n) increased the Poisson noise (n/n) and affected the accuracy of the digital readout. For example, in the case of 64-nm UCNPs and 80-nm UCNP, the nonspecific binding was so low that only 15 diffraction-limited spots were detectable in the imaging area. A count of 15, however, results in a relatively high Poisson noise of 26%. In **Figure 5a**, the lowest baselines show the highest fluctuations, due to the Poisson noise.

An explanation why the digital readout improved the LOD of the PSA assay but not the LOD of the troponin assay may be that the label preparation was more uniform than in our previous PSA assay. Also, the differences in the particular antibody–antigen interactions may explain why the digital assay confers a higher sensitivity only for some analytes. In the analog mode, the PSA assay was ten times more sensitive than the troponin assay. In the digital mode, the PSA assay was even 200 times more sensitive although the number of nonspecifically bound SA-PEG-UCNP labels was ten times higher than the number of mAb-PAA-UCNP labels. Therefore, it seems to be the first requirement that the affinity of the antibody for the analyte is already very high before the sensitivity can be further improved by the digital readout. Compared to commercial cTnI assays and literature reports, however, the ULISA results in a similar or even better assay performance (**Table 2**).

***Table 2**. Assay platforms for the detection of cTnI.*

	Detection label	**LOD [pg mL^{-1}]**	**linear range [ng mL^{-1}]**	**Company/reference**
Commercial assays	Alkaline phosphatase	20	0.00–50.0	Abbott i-STAT[39]
	Alkaline phosphatase	10	0.01–100	Beckman Access 2[40]
	Alkaline phosphatase	10		Beckman Coulter DxI[41]
	Alkaline phosphatase	2.5	0.0023–27000	Beckman Coulter Access hs-cTnI[42]
	Horseradish peroxidase	12		Ortho-Clinical Diagnostics Vitros[43]
	Horseradish peroxidase	100	0.125–8.0	Invitrogen: Human Troponin I (TNNI3) ELISA[44]
Literature reports	5′-6-FAM-modified aptamer	70	0.1–6.0	[45]
	SERS using graphene oxide/gold NP	5	0.01–1000	[46]
	Cyclovoltammetry using whiskered nanofibers	40	0.5–100	[47]
	48-nm UCNP (analog/digital readout)	10	0.04–38 (analog readout)	This work

6.5 Conclusions

For the detection of troponin (cTnI), the advantages conferred by optimizing the assay configuration and the size, brightness, and surface chemistry of UCNP labels were more important than changing from an analog to a digital detection mode. In both cases, an LOD of 10 pg mL^{-1} in human plasma was obtained using mAb-PAA-UCNPs (48 nm in diameter). In contrast to conventional analog measurements, the digital readout allowed for distinguishing between the number of nonspecific binding events (observable as the number of diffraction-limited spots) and the degree of label aggregation (observable as an increase in the brightness of individual diffraction-limited spots). In particular, measurements in human plasma were strongly affected by the size of the UCNP labels. While the number of nonspecific binding events strongly increased with the label size, smaller labels led to slightly more aggregated UCNPs. The digital readout also showed that a low background signal is important to achieve a high sensitivity, but ultimately, the digital assay is limited by the counting noise. When comparing different analytes (troponin and PSA) measured under similar experimental conditions, the particular antibody–analyte interaction had a stronger effect on the assay sensitivity than the degree of nonspecific binding.

Acknowledgements

J.C.B. and K.R. contributed equally to this work. This study was supported by the German Research Foundation (DFG GO 1968/6-2 and Heisenberg Program GO 1968/7-1). Z.F. and P.S. acknowledge financial support from the Ministry of Education, Youth and Sports of the Czech Republic (MEYS CR) under the projects CEITEC 2020 (LQ1601) and INTER-ACTION (LTAB19011). Z.F., A.H., and P.S. acknowledge grant 21-03156S from the Czech Science Foundation. A.H. acknowledges institutional support RVO 68081715 from the Institute of Analytical Chemistry of the Czech Academy of Sciences. K.R. and T.S. acknowledge the funding from Business Finland. CIISB research infrastructure project LM2018127 funded by MEYS CR is acknowledged for the financial support of the measurements at the CF Cryo-electron Microscopy and Tomography, and CF Nanobiotechnology. The authors thank Vít Vykoukal for taking the TEM images and Jaana Rosenberg (Department of Biotechnology, University of Turku) for providing biotin-isothiocyanate.

Open access funding enabled and organized by Projekt DEAL.

Conflict of Interest

The authors declare no conflict of interest.

6.6 References

1. WHO, www.who.int/data/gho/data/themes/mortality-and-global-health-estimates (accessed: July 2021).

2. K. Thygesen, J. S. Alpert, A. S. Jaffe, M. L. Simoons, B. R. Chaitman, H. D. White, E. S. C. A. A. H. A. W. H. F. T. F. f. t. U. D. o. M. I. Joint, H. A. Katus, B. Lindahl, D. A. Morrow, P. M. Clemmensen, P. Johanson, H. Hod, R. Underwood, J. J. Bax, R. O. Bonow, F. Pinto, R. J. Gibbons, K. A. Fox, D. Atar, L. K. Newby, M. Galvani, C. W. Hamm, B. F. Uretsky, P. G. Steg, W. Wijns, J. P. Bassand, P. Menasche, J. Ravkilde, E. M. Ohman, E. M. Antman, L. C. Wallentin, P. W. Armstrong, M. L. Simoons, J. L. Januzzi, M. S. Nieminen, M. Gheorghiade, G. Filippatos, R. V. Luepker, S. P. Fortmann, W. D. Rosamond, D. Levy, D. Wood, S. C. Smith, D. Hu, J. L. Lopez-Sendon, R. M. Robertson, D. Weaver, M. Tendera, A. A. Bove, A. N. Parkhomenko, E. J. Vasilieva, S. Mendis, *Circulation* 2012, **126**, 2020.

3. S. Takeda, A. Yamashita, K. Maeda, Y. Maeda, *Nature* 2003, **424**, 35.

4. I. A. Katrukha, *Biochemistry (Moscow)* 2013, **78**, 1447.

5. A. S. Jaffe, J. Ravkilde, R. Roberts, U. Naslund, F. S. Apple, M. Galvani, H. Katus, *Circulation* 2000, **102**, 1216.

6. K. Thygesen, J. Mair, H. Katus, M. Plebani, P. Venge, P. Collinson, B. Lindahl, E. Giannitsis, Y. Hasin, M. Galvani, M. Tubaro, J. S. Alpert, L. M. Biasucci, W. Koenig, C. Mueller, K. Huber, C. Hamm, A. S. Jaffe, *Eur. Heart J.* 2010, **31**, 2197.

7. D. Westermann, J. T. Neumann, N. A. Sorensen, S. Blankenberg, *Nat. Rev. Cardiol.* 2017, **14**, 472.

8. F. S. Apple, Y. Sandoval, A. S. Jaffe, J. Ordonez-Llanos, *Clin. Chem.* 2017, **63**, 73.

9. IFCC, https://www.ifcc.org/media/478592/high-sensitivity-cardiac-troponin-i-and-t-assay-analytical-characteristics-designated-by-manufacturer-v072020.pdf (accessed: July 2021).

10. E. Antman, J. P. Bassand, W. Klein, M. Ohman, J. L. Sendon, L. Rydén, M. L. Simoons, M. Tendera, *J. Am. Coll. Cardiol.* 2000, **36**, 959.

11. F. S. Apple, C. A. Parvin, K. F. Buechler, R. H. Christenson, A. H. Wu, A. S. Jaffe, *Clin. Chem.* 2005, **51**, 2198.

12. A. G. Katrukha, A. V. Bereznikova, V. L. Filatov, T. V. Esakova, O. V. Kolosova, K. Pettersson, T. Lovgren, T. V. Bulargina, I. R. Trifonov, N. A. Gratsiansky, K. Pulkki, L. M. Voipio-Pulkki, N. B. Gusev, *Clin. Chem.* 1998, **44**, 2433.

13. M. Panteghini, W. Gerhardt, F. S. Apple, F. Dati, J. Ravkilde, A. H. Wu, *Clin. Chem. Lab. Med.* 2001, **39**, 175.

14. M. Panteghini, *Clin. Chim. Acta* 2009, **402**, 88.

15. D. S. Herman, P. A. Kavsak, D. N. Greene, *Am. J. Clin. Pathol.* 2017, **148**, 281.

16. F. S. Apple, P. O. Collinson, I. T. F. o. C. A. o. C. Biomarkers, *Clin. Chem.* 2012, **58**, 54.

17. C. Chenevier-Gobeaux, E. Bonnefoy-Cudraz, S. Charpentier, M. Dehoux, G. Lefevre, C. Meune, P. Ray, S. F. C. S. T. w. Sfbc, *Arch. Cardiovasc. Dis.* 2015, **108**, 132.

18. Z. Farka, T. Jurik, D. Kovar, L. Trnkova, P. Skladal, *Chem. Rev.* 2017, **117**, 9973.

19. Z. Farka, M. J. Mickert, A. Hlavacek, P. Skladal, H. H. Gorris, *Anal. Chem.* 2017, **89**, 11825.

20. A. Hlavacek, Z. Farka, M. Hubner, V. Hornakova, D. Nemecek, R. Niessner, P. Skladal, D. Knopp, H. H. Gorris, *Anal. Chem.* 2016, **88**, 6011.

21. V. Polachova, M. Pastucha, Z. Mikusova, M. J. Mickert, A. Hlavacek, H. H. Gorris, P. Skladal, Z. Farka, *Nanoscale* 2019, **11**, 8343.

22. R. Peltomaa, Z. Farka, M. J. Mickert, J. C. Brandmeier, M. Pastucha, A. Hlavacek, M. Martinez-Orts, A. Canales, P. Skladal, E. Benito-Pena, M. C. Moreno-Bondi, H. H. Gorris, *Biosens. Bioelectron.* 2020, **170**, 112683.

23. U. Kostiv, V. Lobaz, J. Kucka, P. Svec, O. Sedlacek, M. Hruby, O. Janouskova, P. Francova, V. Kolarova, L. Sefc, D. Horak, *Nanoscale* 2017, **9**, 16680.

24. Z. Farka, M. J. Mickert, Z. Mikusova, A. Hlavacek, P. Bouchalova, W. Xu, P. Bouchal, P. Skladal, H. H. Gorris, *Nanoscale* 2020, **12**, 8303.

25. L. Xiong, T. Yang, Y. Yang, C. Xu, F. Li, *Biomaterials* 2010, **31**, 7078.
26. M. J. Mickert, Z. Farka, U. Kostiv, A. Hlavacek, D. Horak, P. Skladal, H. H. Gorris, *Anal. Chem.* 2019, **91**, 9435.
27. Z. Farka, M. J. Mickert, M. Pastucha, Z. Mikusova, P. Skladal, H. H. Gorris, *Angew. Chem., Int. Ed. Engl.* 2020, **59**, 10746.
28. S. Lahtinen, A. Lyytikainen, N. Sirkka, H. Pakkila, T. Soukka, *Mikrochim. Acta* 2018, **185**, 220.
29. N. Sirkka, A. Lyytikainen, T. Savukoski, T. Soukka, *Anal. Chim. Acta* 2016, **925**, 82.
30. S. Eriksson, M. Junikka, P. Laitinen, K. Majamaa-Voltti, H. Alfthan, K. Pettersson, *Clin. Chem.* 2003, **49**, 1095.
31. J. Ylikotila, J. L. Hellstrom, S. Eriksson, M. Vehniainen, L. Valimaa, H. Takalo, A. Bereznikova, K. Pettersson, *Clin. Biochem.* 2006, **39**, 843.
32. M. Pastucha, E. Odstrcilikova, A. Hlavacek, J. C. Brandmeier, V. Vykoukal, J. Weisova, H. H. Gorris, P. Skladal, Z. Farka, *IEEE J. Sel. Top. Quantum Electron.* 2021, **27**, 1.
33. S. Lahtinen, M. Baldtzer Liisberg, K. Raikko, S. Krause, T. Soukka, T. Vosch, *ACS Appl. Nano Mater.* 2021, **4**, 432.
34. L. Välimaa, K. Pettersson, M. Vehniäinen, M. Karp, T. Lövgren, *Bioconjug. Chem.* 2003, **14**, 103.
35. A. Sedlmeier, A. Hlavacek, L. Birner, M. J. Mickert, V. Muhr, T. Hirsch, P. L. Corstjens, H. J. Tanke, T. Soukka, H. H. Gorris, *Anal. Chem.* 2016, **88**, 1835.
36. T. Savukoski, J. Jacobino, P. Laitinen, B. Lindahl, P. Venge, N. Ristiniemi, S. Wittfooth, K. Pettersson, *Clin. Chem. Lab. Med.* 2014, **52**, 1041.
37. T. Savukoski, A. Twarda, S. Hellberg, N. Ristiniemi, S. Wittfooth, J. Sinisalo, K. Pettersson, *Clin. Chem.* 2013, **59**, 512.
38. A. G. Katrukha, in *Cardiac Markers* (Ed.: A. H. B. Wu), 2nd Ed., Humana Press, Totowa, NJ 2002, pp. 173.
39. G. Bozkaya, A. R. Sisman, *Ann. Transl. Med.* 2020, **8**, 1237.
40. F. S. Apple, Y. Sandoval, A. S. Jaffe, J. Ordonez-Llanos, *Clin. Chem.* 2017, **63**, 73,.
41. F. S. Apple, M. M. Murakami, *Clin. Chem.* 2007, **53**, 1558.
42. S. Kim, S. J. Yoo, J. Kim, *Clin. Biochem.* 2020, **79**, 48.
43. F. S. Apple, R. Ler, A. Y. Chung, M. J. Berger, M. M. Murakami, *Clin. Chem.* 2006, **52**, 322.
44. https://www.thermofisher.com/elisa/product/Cardiac-Troponin-I-TNNI3-Human-ELISA-Kit/EHTNNI3 (accessed: July 2021).
45. D. Liu, X. Lu, Y. Yang, Y. Zhai, J. Zhang, L. Li, *Anal. Bioanal. Chem.* 2018, **410**, 4285.
46. X. L. Fu, Y. Q. Wang, Y. M. Liu, H. T. Liu, L. W. Fu, J. H. Wen, J. W. Li, P. H. Wei, L. X. Chen, *Analyst* 2019, **144**, 1582.
47. B. Rezaei, A. M. Shoushtari, M. Rabiee, L. Uzun, W. C. Mak, A. P. F. Turner, *Talanta* 2018, **182**, 178.

6.7 Supporting information

6.7.1 Chemicals and reagents

The following chemicals were obtained from Merck / Sigma-Aldrich (St. Louis, MO, USA):

- anhydrous *N,N*-dimethylformamide (DMF)
- biotinylated bovine serum albumin (BSA-biotin)
- $Na_2B_4O_7$
- bovine γ-globulin (BGG)
- copper(II) sulfate pentahydrate
- D-sorbitol
- D-(+)-trehalose
- heparin sodium salt from procine intestinal mucosa (≥ 180 USP units/mg)
- nitrosyl tetrafluoroborate ($NOBF_4$)
- N-(3-dimethylaminopropyl)-N′-ethylcarbodiimide (EDC)
- N-hydroxysulfosuccinimide sodium salt (sulfo-NHS)
- NHS-LC-biotin
- NHS-dPEG8-azide
- 2-(N-morpholino)ethanesulfonic acid monohydrate (MES)
- poly(acrylic acid) (PAA, MW 2000 Da, 50 % (w/v) solution in H2O)
- poly(acrylic acid) sodium salt (PAA, MW 1200 Da, 45 % (w/v) in H2O)
- sodium borate decahydrate
- Tris(hydroxymethyl)aminomethane (Tris)
- Tween 20
- Tween 85 (with NaN_3)
- $YCl_3 \times 6\ H_2O$ (99.99%)
- Y_2O_3 (99.99%)
- $YbCl_3 \times 6\ H_2O$ (99.998%)
- Yb_2O_3 (99.99%)
- $ErCl_3 \times 6\ H_2O$ (99.99%)
- Er_2O_3 (99.99%)
- NH_4F (>98%)
- octadec-1-ene (technical grade, 90%)
- oleic acid (technical grade, 90%)
- trifluoroacetic acid (99%)

The following chemicals were obtained from Penta (Prague, Czech Republic):

- cyclohexane (p.a.)
- methanol (p.a.)
- $NaHCO_3$
- NaOH (p.a.)
- propan-2-ol (p.a.)

Further chemicals:

- 2-amino-N,N-dimethylacetamide (ADMA, Combi-Blocks, San Diego, CA, USA)

- bovine casein (Calbiochem, La Jolla, CA, USA)
- bovine serum albumin (BSA, Bioreba, Reinach, Switzerland)
- fat-free bovine milk powder (Valio, Helsinki, Finland)
- α-N-hydroxysuccinimide-ω-alkyne poly(ethylene glycol) (NHS-PEG-Alkyne, MW 3000, Iris Biotech, Marktredwitz, Germany)
- IgG, mouse, purified on protein A (9–13 mg/mL, 500 mg NaN_3, Meridian Life Science, Memphis, TE, USA). Denatured mouse IgG was prepared by heat denaturation at 63 °C for 30 min.
- poly(vinyl alcohol) (PVA, MW 6000 Da, Polysciences, Warrington, PA, USA)
- streptavidin (Thermo Fisher Scientific)
- streptavidin-azide (7 Bioscience, Neuenburg, Germany) - SuperBlock (TBS) blocking buffer (Thermo Fisher Scientific)
- wash solution and colourless buffer solution (Kaivogen, Turku, Finland)

6.7.2 Biotinylation of antibodies mAb560 and mAb625

The biotinylation reaction was carried out at room temperature. First, 30 µL of mAb560 or mAb625 (3.18 mg/mL in PBS) were mixed with 1.15 µL of NHS-LC-biotin (5 mg/mL in dry DMF). After 10 min under shaking, another 1.15 µL of NHS-LC-biotin was added and the mixture shaken for 2 h. The biotinylated antibodies were purified via 6 times centrifugation (14,000 g, 20 min) using Amicon ultra centrifugal filters (MW cut-off 100 kDa, Merck, Darmstadt, Germany), transferred to PBS, and stored at 4 °C in the concentration of 1 mg/mL.

6.7.3 Synthesis of UCNPs for the preparation of UCNP-PEG-SA labels

6.7.3.1 Synthesis of Seed UCNPs

$YCl_3 \times 6\ H_2O$ (1165 mg, 4.8 mmol), $YbCl_3 \times 6\ H_2O$ (335 mg, 0.864 mmol) and $ErCl_3 \times 6\ H_2O$ (36.8 mg, 0.096 mmol) were dissolved in methanol (30 mL) and added into a 250-mL three-neck round-bottom flask containing oleic acid (32.3 g, 36 mL) and 1-octadecene (19.7 g, 84 mL). The solution was heated to 170 °C under an N_2 atmosphere for a time long enough to remove all volatile liquids (approximately 60 min) and then the temperature was decreased to 50°C. The protective atmosphere was disconnected, and the solution of NH_4F (711 mg, 19.2 mmol) and NaOH (480 mg, 12 mmol) in methanol (30 mL) was added to the intensely stirred solution. The N2 atmosphere was reconnected, and the solution was stirred for 30 min. The temperature was carefully increased up to 150 °C, avoiding extensive boiling to ensure the evaporation of methanol. After that, the solution was rapidly heated at the rate of ~10 °C per min. At 290 °C, the heating was carefully regulated to 300 °C within one or two minutes. The flask was kept under N_2 flow at 300 °C for 90 min. The fluctuation of temperature was ± 4 °C during this time. Finally, the flask was cooled down to room temperature. The resulting nanoparticles were precipitated by adding propan-2-ol (240 mL) and collected by centrifugation (1,000 *g*, 10 min). The pellet was washed with methanol (90 mL), centrifuged (1,000 *g*, 10 min), and dispersed in cyclohexane (20 mL). By adding methanol (100 mL), the nanoparticles precipitated rapidly without the need for centrifugation. The precipitate was dispersed in cyclohexane (30 mL) and slowly centrifuged (50 *g*, 20 min) to separate coarse particles from the final product.

6.7.3.2 UCNP growth

Under reflux, Y_2O_3 (1355 mg, 6.00 mmol), Yb2O3 (532 mg, 1.35 mmol) and Er_2O_3 (57.9 mg, 0.15 mmol) were dissolved in trifluoroacetic acid (12 mL) and water (12 mL) in a 250 mL three-necked flask. When dissolved, NaHCO3 (1260 mg, 15.00 mmol) was added releasing CO2 bubbles and dissolving rapidly, resulting in a clear solution. After removing the condenser, excessive trifluoroacetic acid and water were evaporated by heating at 110°C in a fume hood (overnight). The resulting white powder of trifluoroacetates was dissolved in oleic acid (45 mL, 40.3 g) and octadec-1-ene (45 mL, 35.5 g). This solution was diluted by 30 mL of methanol. The methanol together with oxygen and water were removed by heating at 110°C under the N_2 atmosphere for 20 min, resulting in a precursor solution. The precursor solution was enclosed in the flask by silicon septa and kept under an inert atmosphere. To decrease the viscosity, the precursor solution was kept at an elevated temperature (~50 °C), which facilitated its injection into the hot reaction mixture. The concentration of $Re(CF_3CO_2)_3$ in the precursor solution was 0.17 mmol mL^{-1} (Re for Y, Yb, Er in molar percentages 80%, 18% and 2.0%, respectively. The nanoparticles were grown by gradually adding the precursor solution to the solution of seed nanoparticles. The dispersion of seed nanoparticles (205 mg) in cyclohexane was mixed with oleic acid (5.5 mL, 4.9 g), octadec-1-ene (17 mL, 13.4 g), and 20 mL of methanol in a 100-mL three-necked flask. The mixture was heated at 150 °C for ~30 min under the N_2 atmosphere to remove oxygen and water. Then, the temperature was rapidly increased to 300 °C. Without decreasing the temperature, a calculated amount of precursor solution was repeatedly injected by a syringe with a long needle (120 mm length); the 9 subsequent addition volumes corresponded to 3.5, 4.0, 4.6, 5.6, 6.2, 7.1, 8.3, 9.6, and 10.1 mL; the time interval between injections was 10 min. The volume of the reaction mixture eventually reached the capacity of the 100-mL flask. Therefore, the reaction mixture was transferred to a 250-mL three-necked flask together with 30 mL of methanol. Under an inert N_2 atmosphere, the oxygen, methanol, and water were removed by heating at 150 °C for ~30 min. The temperature was rapidly increased to 300 °C, and the injection procedure was repeated. After the last injection, the temperature was kept at 300 °C for 10 min, eventually preparing nanoparticles of the desired size (reaction mixture volume ~82 mL), and the synthesis continued without decreasing the temperature by growing the inert shell of $NaYF_4$.

6.7.3.3 Inert shell growth

Under reflux, Y2O3 (1694 mg, 7.50 mmol) was dissolved in trifluoroacetic acid (12 mL) and water (12 mL) in a 250-mL three-necked flask. When dissolved, $NaHCO_3$ (1260 mg, 15.00 mmol) was added releasing CO_2 bubbles and dissolving rapidly to a clear solution. After removing the condenser, excessive trifluoroacetic acid and water were evaporated by heating at 110 °C in a fume hood (overnight). The resulting white powder of trifluoroacetates was dissolved in oleic acid (45 mL, 40.3 g) and octadec-1-ene (45 mL, 35.5 g). This solution was diluted by 30 mL of methanol. The methanol together with oxygen and water were removed by heating at 110 °C under an inert N_2 atmosphere for 20 min resulting in a precursor solution. The precursor solution was enclosed in the flask by silicon septa and kept under an inert atmosphere. To decrease the viscosity, the precursor solution was held at an elevated temperature (~50 °C), which facilitated its injection into the hot reaction mixture. The concentration of $Y(CF_3CO_2)_3$ in the precursor solution was 0.17 mmol mL^{-1}.

The shell was grown by gradually adding the precursor solution to the hot solution of grown nanoparticles from the previous step. A calculated amount of precursor solution was repeatedly injected by a syringe with a long needle (120 mm) without decreasing the temperature. The three additions were of 8.0, 9.0, and 10.0 mL; the time interval between the injections was 10 min. After the last injection, the temperature was kept at 300 °C for an additional 10 min, eventually preparing the desired nanoparticles (the volume of the reaction mixture ~95 mL). Finally, the flask was cooled to room temperature. The resulting nanoparticles were precipitated by adding propan-2-ol (190 mL) and collected by centrifugation (1,000 *g*, 10 min). The pellet was washed with methanol (109 mL), centrifuged (1,000 *g*, 10 min), and dispersed in cyclohexane (60 mL). After the last precipitation by methanol, the nanoparticles were dispersed in cyclohexane and slowly centrifuged (50 *g*, 20 min) to separate coarse particles from the final product.

6.7.4 Preparation of click-reactive streptavidin

For the preparation of click-reactive streptavidin-azide, 31.25 µL of NHS-dPEG$_8$-azide (200 mM, Sigma-Aldrich, St. Louis, MO, USA) in DMF were added to 150 µL of streptavidin (4.0 mg/mL) in DMF. The 187.5 µL of phosphate buffer (50 mM NaH_2PO_4/Na_2HPO_4, pH 7.4) were added, the reaction mixture was incubated for 2 h at room temperature, and then quenched by the addition of Tris-HCl (50 mM, pH 7.4). The streptavidin-azide was purified via 6 times centrifugation (14,000 *g*, 20 min) using Amicon ultra centrifugal filters (MW cut-off 10 kDa, Merck, Darmstadt, Germany), transferred to PBS, and stored at 4 °C in the concentration of 1 mg/mL.

6.7.5 Characterization of UCNPs and UCNP conjugates

6.7.5.1 Transmission electron microscopy (TEM)

Oleic acid-capped UCNPs ($NaYF_4$:Yb^{3+}, Er^{3+}) in cyclohexane were diluted and dispensed on carbon-coated copper grids. The excess dispersion was removed and the grids were allowed to dry on air. TEM images were recorded either on a Titan Themis (FEI, Czech Republic) or a JEM-1400 Plus (JEOL, Massachusetts, USA).

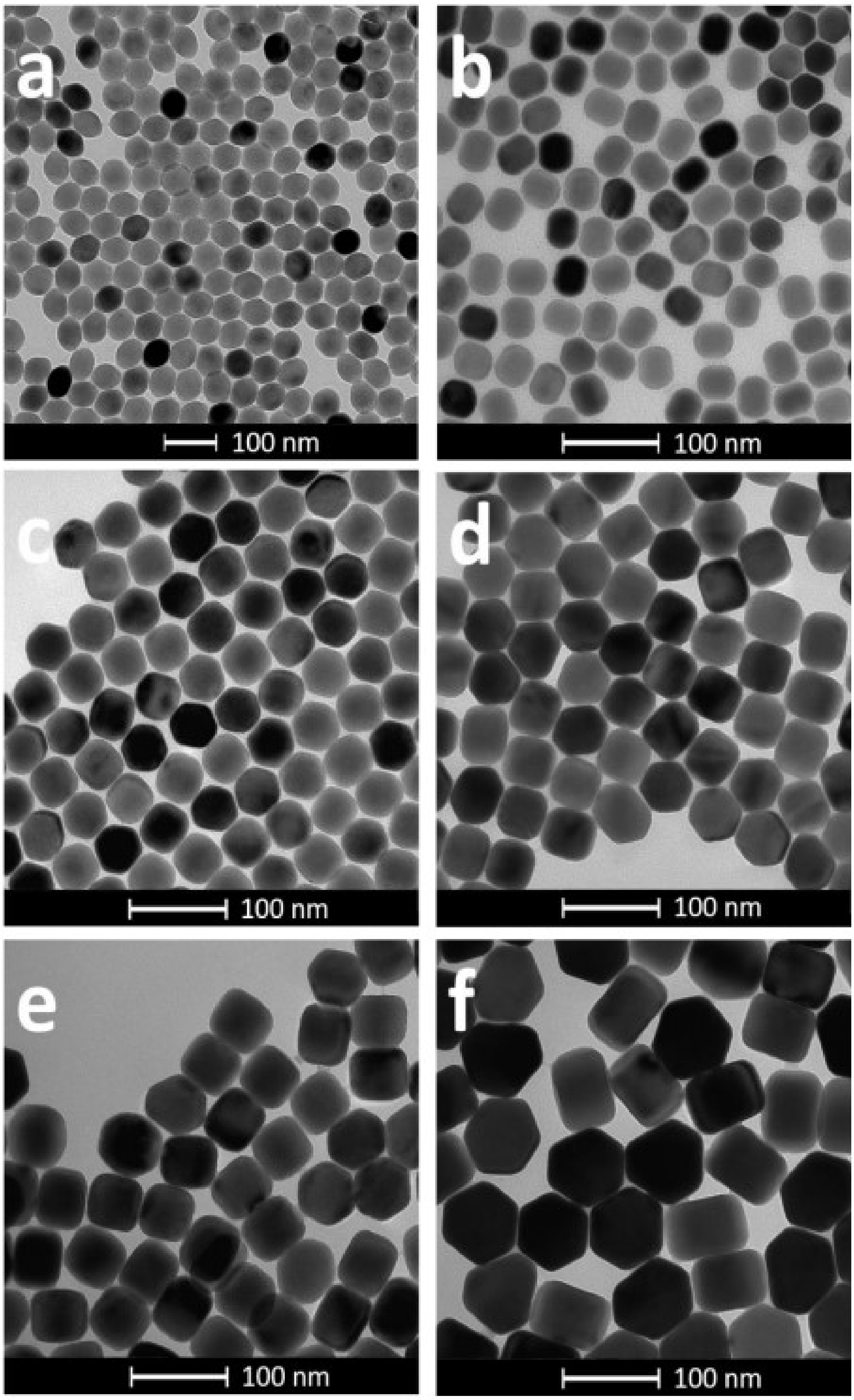

***Figure S1**. TEM-images of $NaYF_4$: Yb^{3+}, Er^{3+} -UCNPs of sizes (a) 63 nm (used for the SA-PEG-UCNP conjugates), and (b) 40 nm, (c) 48 nm, (d) 56 nm, (e) 64 nm, (f) 80 nm (used for the mAb-PAA-UCNP conjugates).*

6.7.5.2 Dynamic light scattering (DLS)

The hydrodynamic diameters of the UCNPs and their conjugates were determined by DLS using a Zetasizer Nano (Malvern, UK). A dispersion of 187 µg/mL for Er-doped oleic acid capped UCNPs (in cyclohexane) and 325 µg/mL (in 50 mM Tris) for their bioconjugates were used for the characterization.

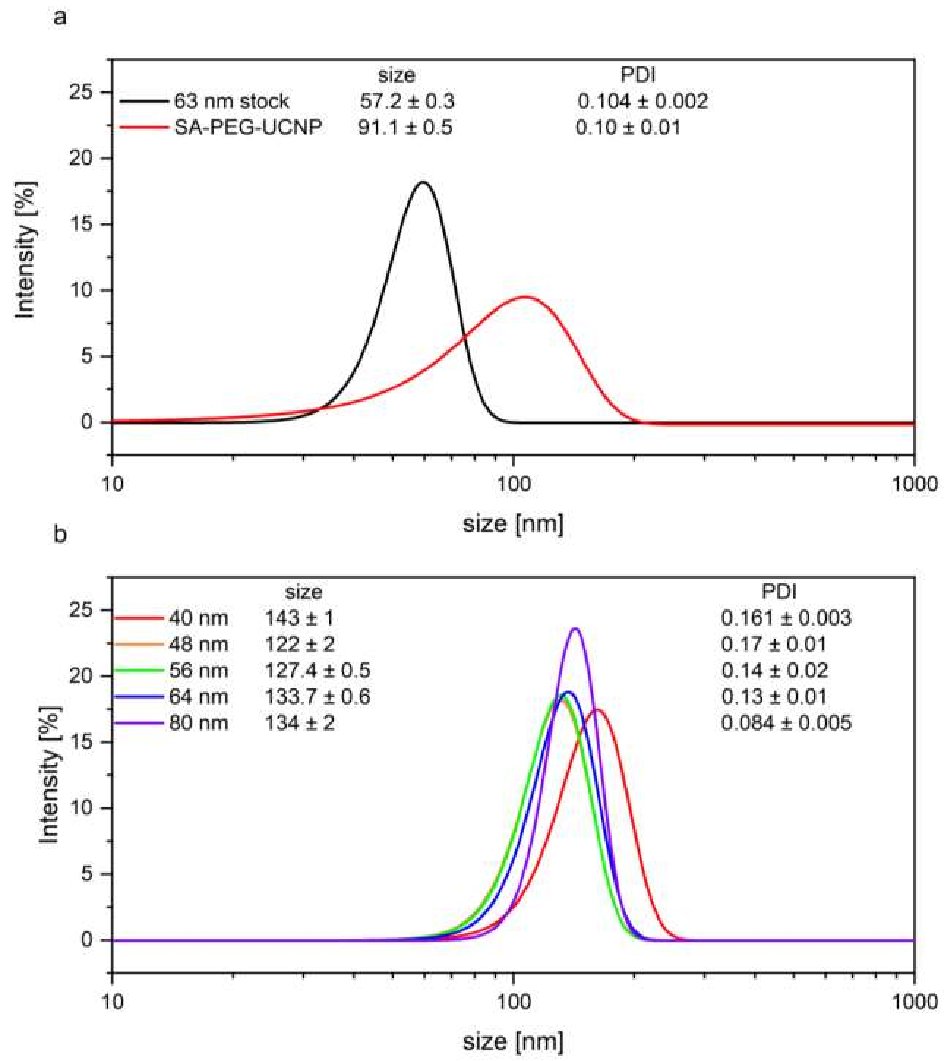

Figure S2. *DLS particle size distributions (by intensity) of (a) SA-PEG-UCNP with oleic acid coating (in cyclohexane) and after conjugation with streptavidin (in 25 mM Tris), and (b) mAb-PAA-UCNP conjugates (in water). The size distributions are summarized in Table S1.*

6.7.5.3 Upconversion emission spectra

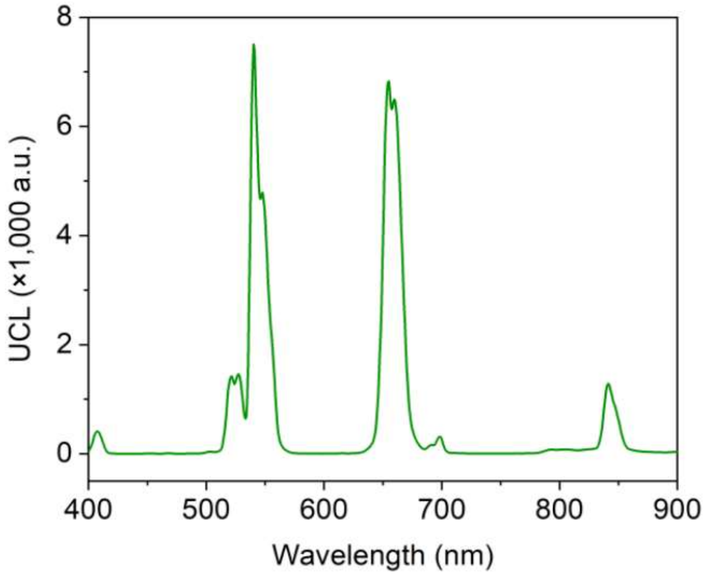

Figure S3. *Spectrum of UCNPs (NaYF$_4$:Yb^{3+},Er^{3+}, 63 nm in diameter) under 980-nm excitation.*

6.7.6 Optimization of the troponin detection system

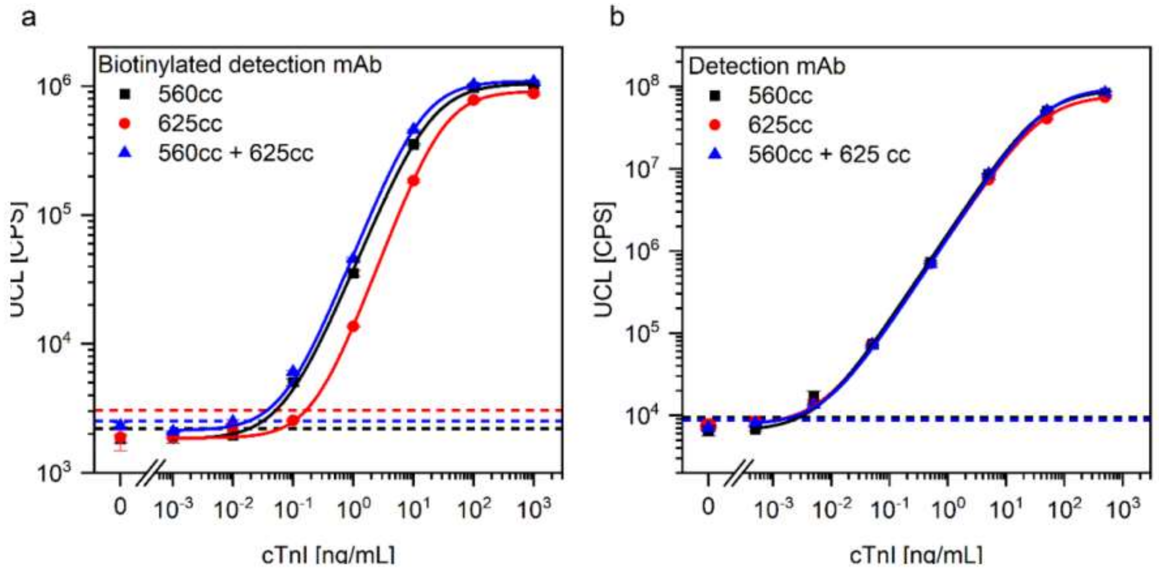

Figure S4. *Comparison of label combinations for the detection of cTnI in BSA/BGG buffer. (a) ULISA configuration with mAb-coated microtiter plates and SA-PEG-UCNP labels (63 nm in diameter) in combination with biotinylated detection antibodies. (b) ULISA configuration with streptavidin-coated microtiter plates and mAb-PAA-UCNP detection labels (25 nm in diameter). In further experiments, UCNPs of 40–80 nm in diameter were used to enable not only the optimization of the analog, but also of the digital readout.*

6.7.7 Digital ULISA based on single-particle upconversion microscopy

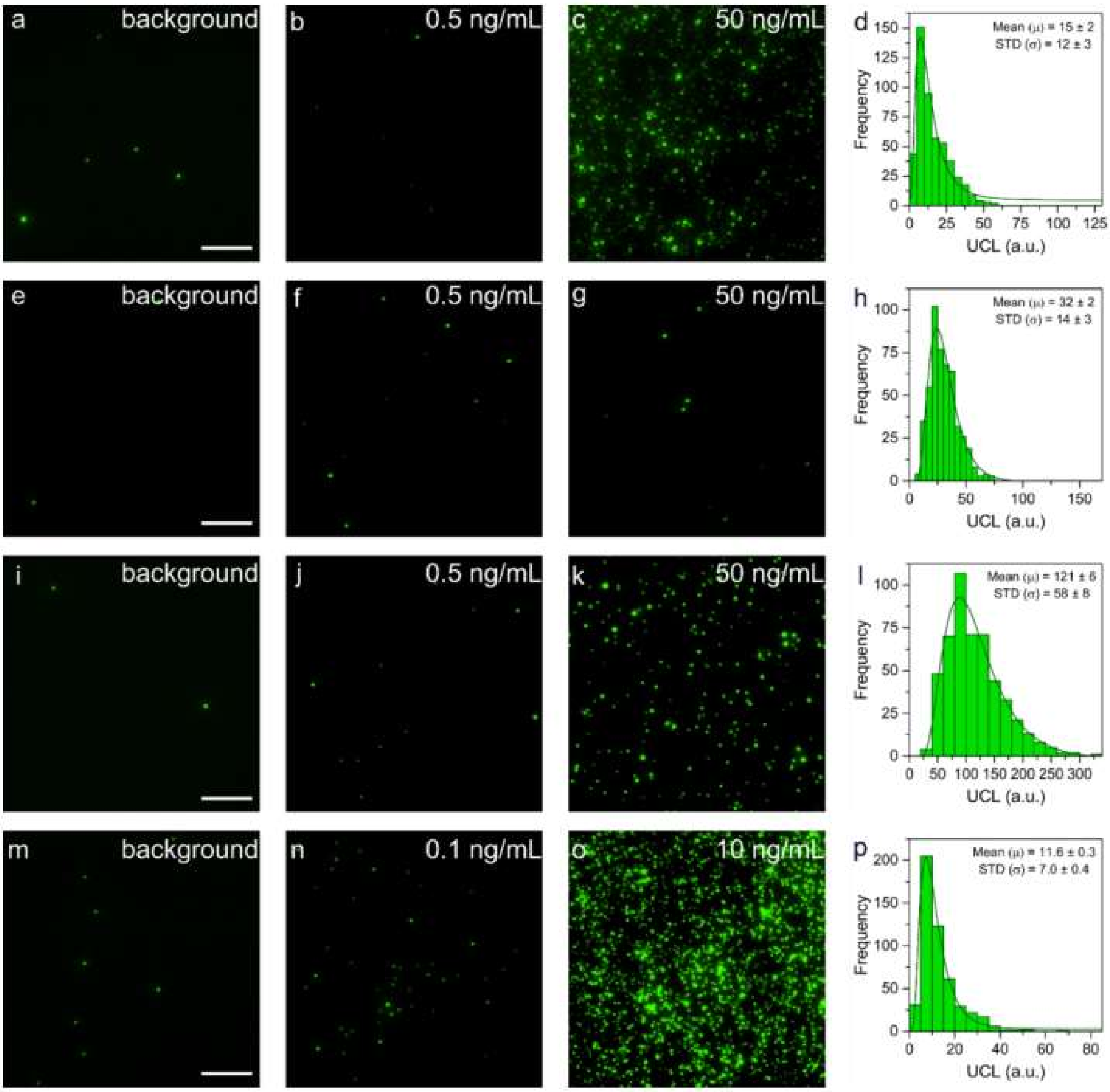

Figure S5. *Digital ULISA of troponin dilutions in buffer. (a–d) mAb-PAA-UCNP (48 nm in diameter). (e–h) mAb-PAA-UCNP (64 nm in diameter). (i–l) mAb-PAA-UCNP (80 nm in diameter). (m-p) SA-PEG-UCNP (63 nm in diameter). Wide-field upconversion microscopy images and brightness distribution histograms of 500 diffraction-limited spots. Scale bar: 10 µm.*

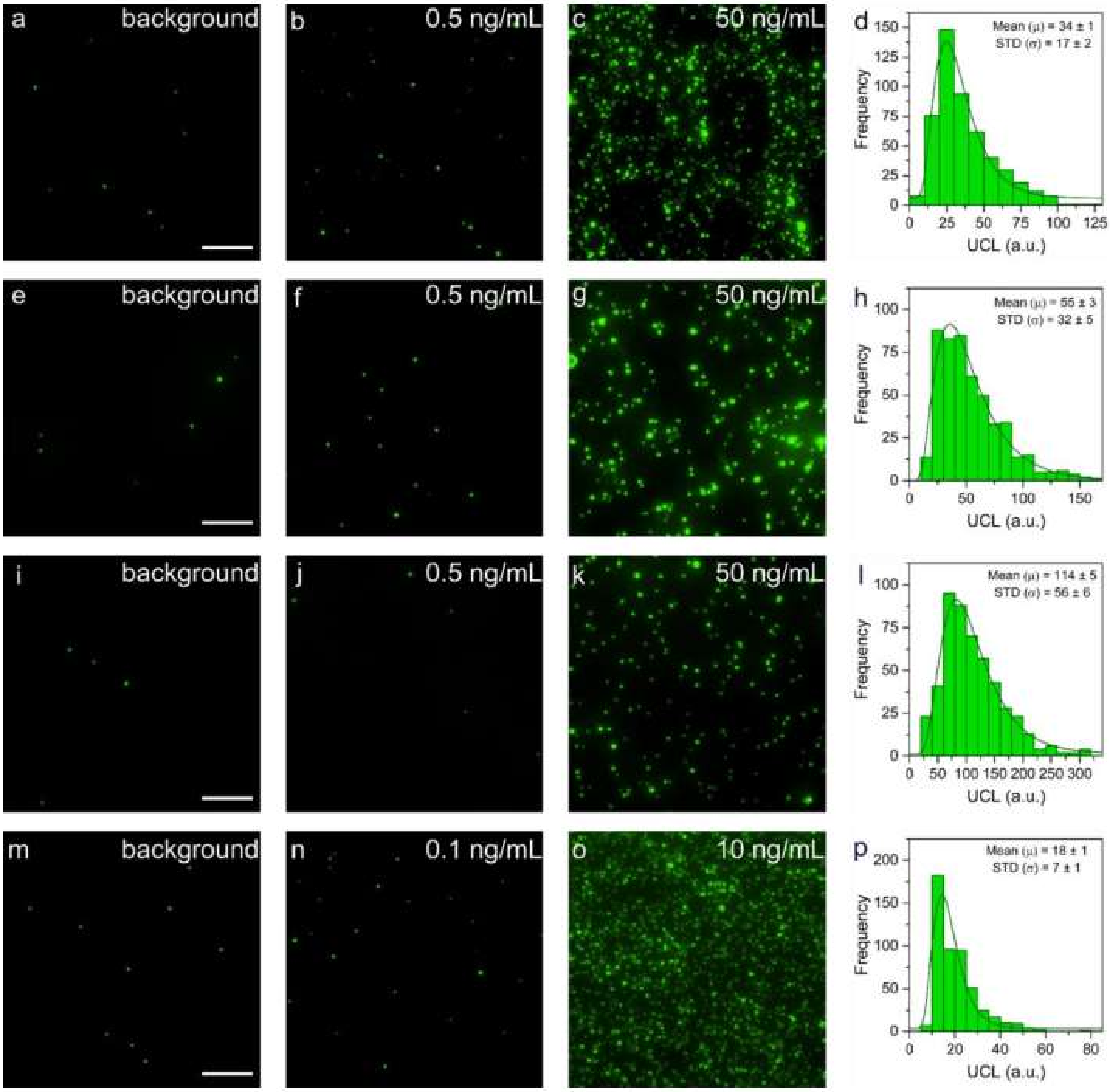

***Figure S6**. Digital ULISA of troponin dilutions in plasma. (a–d) mAb-PAA-UCNP (48 nm in diameter). (e–h) mAb-PAA-UCNP (64 nm in diameter). (i–l) mAb-PAA-UCNP (80 nm in diameter). (m–p) SA-PEG-UCNP (63 nm in diameter). Wide-field upconversion microscopy images and brightness distribution histograms of 500 diffraction-limited spots. Scale bar: 10 µm.*

***Table S1**. Homogeneity of UCNP labels*

Type of label/assay	Size[a] (nm)	Label brightness[b] in buffer	Label brightness[b] in plasma	Hydrodynamic size distribution[c]
mAb-PAA-UCNP	40	n.d.[d]	n.d.[d]	40
	48	15 ± 12	34 ± 1	41
	56	49 ± 30	63 ± 3	37
	64	32 ± 14	55 ± 32	42
	80	121 ± 58	114 ± 56	29
SA-PEG-UCNP	63	12 ± 7	18 ± 7	32

[a] Average UCNP diameter determined by TEM (**Figure S1**).

[b] Mean (μ) luminescence intensity ± standard deviation (σ) of diffraction-limited spots based on LogNormal fit (**Figures S5–S6**).

[c] Calculated as 100√PDI (**Figure S2**).

[d] Not determinable because smaller UCNPs are not bright enough for single nanoparticle detection.

6.7.8 Digital readout using SA-PEG-UCNP labels

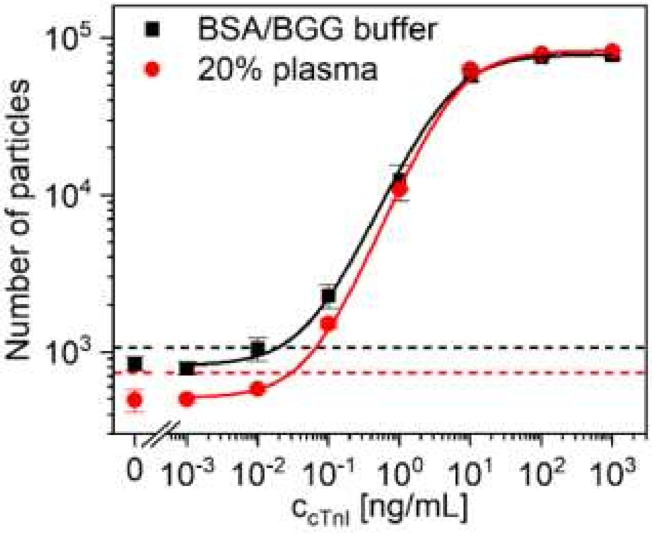

***Figure S7**. Calibration curves of the digital ULISA using biotinylated mAb 560cc and SA-PEG-UCNP labels. cTnI was serially diluted in either BSA/BGG buffer (LOD: 19.0 pg/mL) or 20% plasma (LOD: 31.0 pg/mL) in BSA/BGG buffer. The error bars show the standard deviation of three replicate measurements; the hatched lines indicate the LODs.*

7 Article II

Digital and analog detection of SARS-CoV-2 nucleocapsid protein via an upconversion-linked immunosorbent assay

Julian C. Brandmeier, Natalia Jurga, Tomasz Grzyb, Antonín Hlaváček, Radka Obořilová, Petr Skládal, Zdeněk Farka, and Hans H. Gorris

Reproduced with permission from:
Analytical Chemistry **2023**, *95*, 4753–4759.

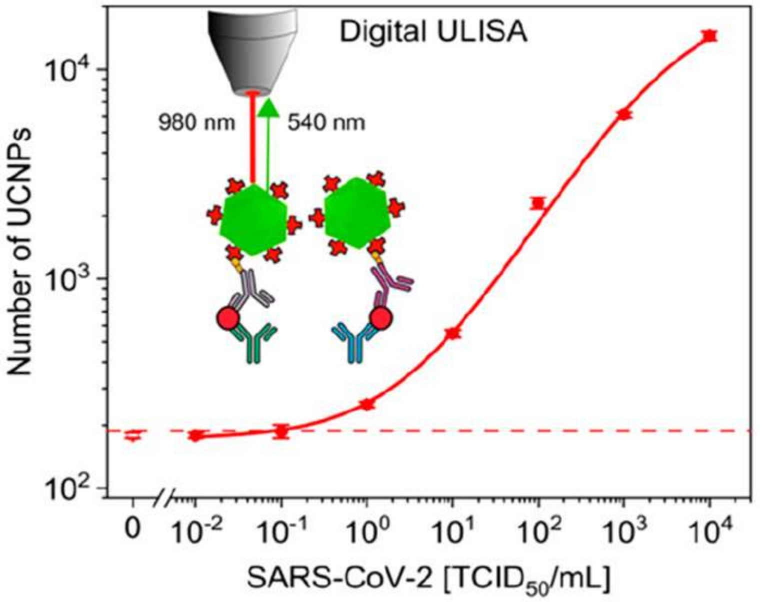

7.1 Abstract

The COVID-19 crisis requires fast and highly sensitive tests for the early stage detection of the SARS-CoV-2 virus. For detecting the nucleocapsid protein (N protein), the most abundant viral antigen, we have employed upconversion nanoparticles that emit short-wavelength light under near-infrared excitation (976 nm). The anti-Stokes emission avoids autofluorescence and light scattering

and thus enables measurements without optical background interference. The sandwich upconversion-linked immunosorbent assay (ULISA) can be operated both in a conventional analog mode and in a digital mode based on counting individual immune complexes. We have investigated how different antibody combinations affect the detection of the wildtype N protein and the detection of SARS-CoV-2 (alpha variant) in lysed culture fluid via the N protein. The ULISA yielded a limit of detection (LOD) of 1.3 pg/mL (27 fM) for N protein detection independent of the analog or digital readout, which is approximately 3 orders of magnitude more sensitive than conventional enzyme-linked immunosorbent assays or commercial lateral flow assays for home testing. In the case of SARS-CoV-2, the digital ULISA additionally improved the LOD by a factor of 10 compared to the analog readout.

7.2 Introduction

During the last three years of the COVID-19 pandemic, testing, social distancing, and finally vaccination have been the key factors in keeping the pandemic under control.[1] In particular testing has been essential to identify asymptomatic individuals, whose contribution to virus transmission was largely underestimated at the beginning.[2] Depending on the analyte, three types of SARS-CoV-2 assays can be distinguished: (1) Viral RNA tests based on PCR amplification are the most sensitive, but they have long turnaround times and are relatively expensive.[3] (2) Serological tests detect whether a person has raised antibodies against SARS-CoV-2. As there is a lag time between an infection and an immune response, however, such assays are not amenable to early stage disease diagnosis. (3) Viral antigen tests are fast, cheap, and suitable for point-of-care testing, but they are typically less sensitive than PCR.[4]

The nucleocapsid protein (N protein) is the most abundant protein antigen in SARS-CoV-2 and shows lower mutation rates among different variants compared to the spike protein.[5] As these features enable more sensitive measurements and a more reliable detection of different virus variants by the same antibodies, the N protein is commonly used as a target antigen in microtiter-plate enzyme-linked immunoassays (ELISA) and lateral flow immunoassays (LFA) intended for point-of-care testing.[6] Various other assay formats and detection schemes for the diagnosis of SARS-CoV-2 have been reviewed recently.[7,8]

The optical readout of an enzymatic product in standard ELISAs or of colloidal gold in LFAs, however, is affected by optical background interference. By contrast, photon-upconversion nanoparticles (UCNP) emit shorter-wavelength light under near-infrared excitation (anti-Stokes emission) and thus eliminate optical background interference due to autofluorescence and light scattering.[9,10] Consequently, immunoassays using UCNPs as a detection label (ULISA) have the potential to be >100-fold more sensitive compared to ELISA[11] and LFA[12] if nonspecific binding is efficiently avoided. Therefore, we developed water-dispersible and highly homogeneous UCNP labels that show a very low degree of nonspecific binding by employing a ligand exchange reaction with a neridronate poly(ethylene glycol) (PEG) conjugate (**Figure 1A**).[13]

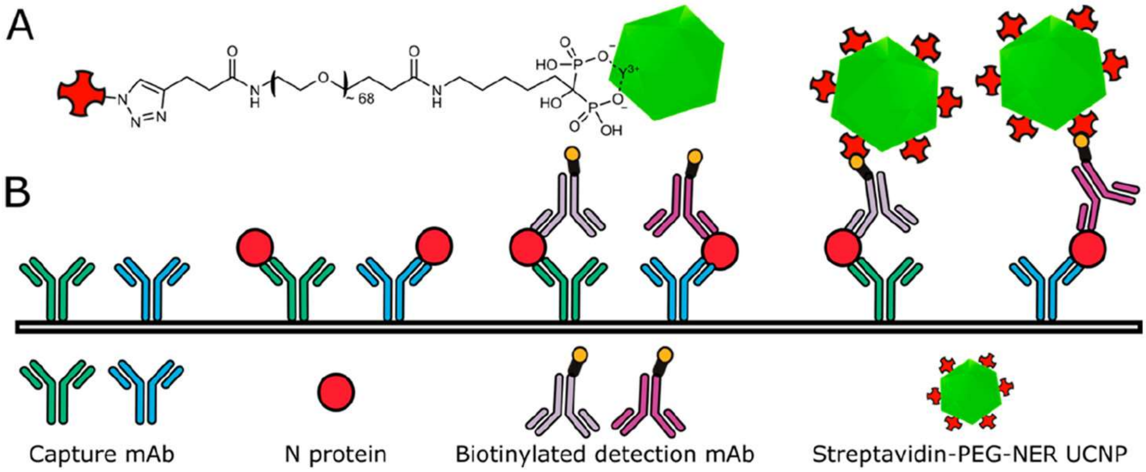

***Figure 1**. Detection of SARS-CoV-2 N protein. (A) UCNP label: Alkyne-PEG-neridronate strongly binds via two phosphonate groups to surface lanthanide ions of UCNPs, and a click reaction binds the conjugate to azide-modified streptavidin. (B) Scheme of sandwich ULISA: A microtiter plate is coated with two monoclonal antibodies that capture the N protein. Then, two biotinylated detection antibodies bind to the N protein. The sandwich immune complex is finally detected by using the UCNP label.*

The absence of optical background interference enables detecting and counting single UCNP-labeled immune complexes (digital mode) using a modified wide-field epiluminescence microscope.[14] The digital ULISA is, in principle, not affected by variations in nanoparticle brightness (as long as they are bright enough for an unambiguous detection), particle aggregation, and instrumental background.[15] We found, however, that the digital readout did not always result in a higher sensitivity compared to the conventional analog readout. While the detection of the cancer marker prostate-specific antigen (PSA) was 16-fold improved by using the digital readout,[11] no significant improvement of the sensitivity was observed for the detection of human cardiac troponin I (cTnI), the most important marker of myocardial infarction.[16] These experiments revealed that the sizes of UCNPs did not influence the assay sensitivity in the buffer but had a strong effect when plasma was used. For the detection of SARS-CoV-2, a UCNP-based test for viral oligonucleotides was reported,[17] and a UCNP-based antigen test awaits market introduction.[18] However, no original research report has been published, yet.

Here, we present a microtiter-based sandwich ULISA (**Figure 1B**) for the detection of N protein and SARS-CoV-2 and compare it to a conventional ELISA.[19] The ULISA can be operated both in the analog and digital mode. Our earlier studies indicated that the digital readout is a necessary but not sufficient condition to achieve the highest possible assay sensitivity.[15] The higher the antibody affinity is, the higher is the potential conferred by the digital readout. This is also in line with an earlier report that the LOD of the digital ELISA strongly depends on the antibody affinities.[20] We have thus investigated the effect of different antibody combinations on the assay performance.

7.3 Materials and methods

7.3.1 Reagents and buffers

Recombinant SARS-CoV-2 N protein (full-length wildtype protein (GenBank: QHD43423.2) including C-terminal GS linker and His10-tag, M_W 47.1 kDa) and monoclonal anti-N protein antibody (mAb) clones C518, C524, C706, and C715 that bind to the N-terminal part (N47-A173) of the N protein were purchased from HyTest (Turku, Finland). Antibodies were characterized by surface plasmon resonance (SPR) and biotinylated as described in the **Supporting Information**. SuperBlock in Tris-buffered saline (TBS) was obtained from Thermo Fisher (Waltham, MA, USA), streptavidin-conjugated horseradish peroxidase (SA-HRP) from Abcam (Cambridge, UK), and TMB-Complete 2 substrate solution from

TestLine Clinical Diagnostics (Brno, Czech Republic). Heat-inactivated SARS-CoV-2 culture fluid (alpha variant B.1.1.7, isolate USA/CA_CDC_5574/2020) was purchased from ZeptoMetrix (Buffalo, NY, USA) and used in a laboratory meeting BSL-2 standards.

Buffers were prepared using double-distilled water filtered through a 0.22-µm membrane (Magna Nylon, GVS, Zola Predosa, Italy). Buffers for the dilution of reagents included phosphate buffer (PB; 50 mM NaH_2PO_4/Na_2HPO_4, pH 7.4), phosphate-buffered saline (PBS; PB with 150 mM NaCl), and Tris-buffered saline (TBS; 50 mM Tris, 150 mM NaCl, pH 7.5). Coating buffer consisted of 50 mM $NaHCO_3/Na_2CO_3$, 0.05% NaN_3, and pH 9.6. Furthermore, washing buffer (50 mM Tris, 5 mM $CaCl_2$, 0.05% Tween 20, pH 7.5), blocking buffer (10% SuperBlock in TBS, 1 mM KF, 0.05% NaN_3, pH 7.5), and Tris assay buffer (10% SuperBlock in TBS, 1 mM KF, 0.05% Tween 20, 0.05% PEG, 0.05% NaN_3, pH 7.5) were used. KF increases the stability of UCNPs in diluted aqueous dispersions.[21] For the ELISA, the same buffers were prepared without NaN_3 to avoid interference with the enzymatic activity of horseradish peroxidase.

Two commercial buffers for the lysis of SARS-CoV-2 capsids were obtained from Hangzhou Singclean Medical Products (Zhejiang, China) and Lotus NL (Den Haag, The Netherlands), denoted as “Lysis-Sing” and “Lysis-Lotus”, respectively. Additionally, the “Lysis-Guan” buffer[22] containing guanidinium thiocyanate as a chaotropic reagent and Triton X-100 as a detergent and the “Lysis-X” buffer[23] containing only Triton X-100 were prepared as described in the **Supporting information.**

7.3.2 Preparation and characterization of UCNP labels

The syntheses of core/shell UCNPs ($NaYF_4$: 18% Yb, 2% Er/$NaYF_4$, 58 nm in diameter) and the alkyne-polyethylene(glycol)-neridronate linker (alkyne-PEG-ner) are described in the **Supporting information**. For the preparation of SA-PEG-UCNP labels, 311 µL (10 mg) of UCNPs dispersed in cyclohexane was mixed with the same volume of 200 mM aqueous HCl and incubated for 30 min at 38 °C under shaking. The solution was then sonicated for 15 min to remove oleic acid from the UCNP surface and mediate a phase transfer from cyclohexane to water. The lower HCl phase was taken and added to an approximately 2-fold excess of acetone, which led to the precipitation of UCNPs. After centrifugation at 1000*g* for 20 min, the UCNP pellet was redispersed in 500 µL of water and sonicated for 5 min. Then, 2 mg of the linker dissolved in 500 µL of water was added and shaken overnight at 38 °C. Excess amounts of linker were removed by dialysis of the UCNP conjugates in a Float-A-Lyzer G2 dialysis device (100 kDa M_W cutoff, Fisher Scientific, Waltham, MA, USA) for 72 h at 4 °C against 4 L of 1 mM KF in water, which was exchanged nine times.

The UCNP conjugates were functionalized with streptavidin using a click reaction. Tris-HCl (375 mM, pH 7.5; 100 µL) and an aqueous solution of $CuSO_4$ (25 mM; 10 µL) were added to 10 mg of alkyne-PEG-ner UCNPs dispersed in 1.4 mL of water. After purging the mixture for 45 min with argon, 100 µL of streptavidin azide (1 mg/mL) was added, and the mixture was purged for another 10 min. The click reaction was started by adding 20 µL of 100 mM sodium ascorbate in water. The dispersion was purged for 40 min with argon and then dialyzed for 72 h at 4 °C in a Float-A-Lyzer G2 dialysis device (100 kDa M_W cutoff) against 4 L of a dialysis buffer (50 mM Tris, 0.05% NaN_3, 1 mM KF, pH 7.5), which was exchanged nine times.

The UCNPs and their conjugates were characterized using transmission electron microscopy (TEM), dynamic light scattering (DLS), and emission spectroscopy under 976 nm excitation as described in the **Supporting information.**

7.3.3 Release of N protein from SARS-CoV-2 in culture fluid and nasopharyngeal swabs

The manufacturer provided the concentration of SARS-CoV-2 in heat-inactivated culture fluid as the median tissue culture infectious dose ($TCID_{50}$/mL = 1.05 × 10^6). The $TCID_{50}$/mL was also used to indicate the concentration of all further SARS-CoV-2 dilutions. For releasing the N protein from the virus, one part of culture fluid was mixed with nine parts of Lysis-Sing, Lysis-Lotus, Lysis-Guan, or Lysis-X, respectively, incubated under rotation for 20 min at room temperature and then diluted in Tris assay buffer. The virus lysate was prepared just before the immunoassay experiments.

Nasopharyngeal virus samples were collected by using cotton swabs. For the resuspension and lysis of the virus, cotton swabs were immersed and rotated in a vial containing Lysis-Sing, which was included with the LFA test kit. The virus lysate was prepared and 10-fold diluted in Tris assay buffer just before the LFA or immunoassay experiments.

7.3.4 Lateral flow assays

COVID-19 rapid antigen tests based on colloidal gold as a detection label were purchased from local retail stores and employed for reference experiments. (1) LFAs from Joinstar Biomedical Technology (Zhejiang, China) were used for the detection of SARS-CoV-2 in culture fluid. Culture fluid samples were 10-fold diluted in the supplied lysis buffer, and all further steps were performed according to the manufacturer’s instructions. (2) LFAs from New Gene Bioengineering (Hangzhou, China) were used for the detection of a volunteer’s active corona infection. After the onset of the first corona-related symptoms, nasopharyngeal swabs were collected daily as described above and stored at −20 °C until further use. All further steps were performed according to the manufacturer’s instructions. LFAs were considered positive when both the test (T) line and the control (C) line were detectable by eye and negative when only the C line showed a signal.

7.3.5 Microtiter-based immunoassays

The initial steps of ELISA and ULISA were carried out in the same way except for the following differences: (1) Standard high-binding 96-well microtiter plates (Greiner, Austria) were used for ELISA, while high-binding 96-well plates with a thin bottom foil (µClear, Greiner) were used for ULISA to allow for the digital readout under the microscope. (2) The ELISA reagents did not contain NaN_3.

A 96-well microtiter plate was coated with 100 µL of a mixture of two monoclonal anti-N protein antibodies (C715 and C518, each 0.5 µg/mL) in a coating buffer overnight at 4 °C. All subsequent steps were carried out at room temperature. The plate was washed four times with 200 µL of the washing buffer. The plate was blocked for 1 h with 150 µL of the blocking buffer, washed four times, and 100 µL of serial dilutions of either the recombinant N protein or the virus lysate in Tris assay buffer was added and incubated for 1 h. The microtiter plate was washed four times with 200 µL of the washing buffer and incubated for 1 h with 100 µL of a mixture containing two biotinylated anti-N protein antibodies (C706 and C524, each 0.5 µg/mL) in a Tris assay buffer. The microtiter plate was washed four times with 200 µL of the washing buffer before the protocol for ELISA and ULISA diverged:

ELISA: A streptavidin-HRP conjugate (100 µL, 0.03 µg/mL in Tris assay buffer) was added for 1 h. The plate was washed four times with 200 µL of the washing buffer, and 100 µL of TMB substrate solution was added. After 1 min, 1 M sulfuric acid was added to stop the signal development, and the absorbance at 450 nm was measured on a Synergy 2 plate reader (BioTek, Winooski, VT, USA). A four-parameter logistic function was used for data fitting (Origin 2020, OriginLab, Northampton, MA USA), and LODs were calculated by adding three times the standard deviation of the blank to the baseline of the regression curve.

ULISA: SA-PEG-UCNPs (100 µL, 6.5 µg/mL) were added for 1 h in Tris assay buffer. The plate was then washed four times (200 µL) and left to dry.

7.3.5.1 *Analog readout of ULISA*

An upconversion microtiter plate reader (UPCON, Labrox, Turku, Finland) equipped with a 976 nm laser excitation source was used for measuring the upconversion luminescence (UCL) of Er-doped UCNPs at 540 nm in units of counts per second (CPS).[13] In each well, 8 × 8 points were raster-scanned with a distance of 100 µm and a signal integration time of 1 s. The 16 highest and 16 lowest values were discarded, and the mean value was calculated, providing the truncated average of the intensity in a single well. The plotted averages and standard deviations were determined from three independent wells. The data was fitted by a four-parameter function. LODs were obtained by adding three times the standard deviation of the blank to the baseline of the regression curve.

7.3.5.2 *Digital readout of ULISA*

An inverted wide-field epifluorescence microscope (Eclipse Ti, Nikon, Tokyo, Japan) was connected to a continuous-wave 976 nm laser diode (4 W, Wavespectrum, Tianjin, China) via a multimode optical fiber (105 µm fiber core, 0.22 NA, Wavespectrum) and a motorized TIRF/epifluorescence illuminator unit (Eclipse Ti-E, Nikon). The filter cube for the detection of Er^{3+}-doped UCNPs consisted of a long-pass excitation filter ($\lambda_{cut\text{-}on}$ = 830 nm, Schott, Mainz, Germany), a dichroic mirror ($\lambda_{cut\text{-}on}$ = 875 nm, AHF Analysentechnik, Tübingen, Germany), and a band-pass filter (λ = 535 ± 70 nm, $OD_{980} \approx 6$, Chroma, Bellows Falls, VT, USA). The images were acquired on an sCMOS camera (5.5 megapixel; Neo, Andor Technology, Belfast, UK) and a 100× objective (1.49 NA; CFI HP Apochromat TIRF, Nikon), which resulted in a power density of 640 W/cm^2.[13]

In each well filled with 100 µL of D_2O for heat dissipation of the NIR laser beam, nine wide-field images of 166 µm × 144 µm were taken with a 100-fold objective and an exposure time of 7 s. The images were analyzed using NIS Elements 4.5 (Nikon). The total number of UCNPs in the nine images was counted automatically. The average and standard deviation were calculated from three wells, and the data were fitted using a four-parameter logistic function. LODs were obtained by adding three times the standard deviation of the blank to the baseline of the regression curve.

7.4 Results and discussion

7.4.1 Optimization of antibody combinations for the detection of wildtype N protein

The sensitivity of an immunoassay does not only depend on the assay design and labeling (**Figures S1–S3**) but also on the selection and combination of high-affinity antibodies, which need to be optimized for each analyte.[16] The manufacturer of the monoclonal anti-N protein antibodies recommended the pairwise combination of two capture and two detection antibodies (2 + 2) for LFAs, which increases the likelihood of efficiently recognizing different variants (in this study, the wildtype virus and the alpha variant).[24] They further tested and confirmed that the antibodies are not cross-reactive with other respiratory viruses including seasonal coronaviruses, which is important to prevent false-positive results.[25]

We tested all possible 2 + 2 combinations of four mAbs for the detection of recombinant wildtype N protein (**Figure 2**). The respective detection antibodies were biotinylated for subsequent binding of streptavidin-UCNP labels. These antibody combinations resulted in up to 100-fold differences in the LOD, which was strongly, but not only, dependent on the degree of nonspecific binding (baseline of the regression curve). The combination of C518 and C715 as capture antibodies and biotinylated C524 and C706 as detection antibodies resulted in the lowest LOD (0.33 pg/mL; blue curve in **Figure 2**).

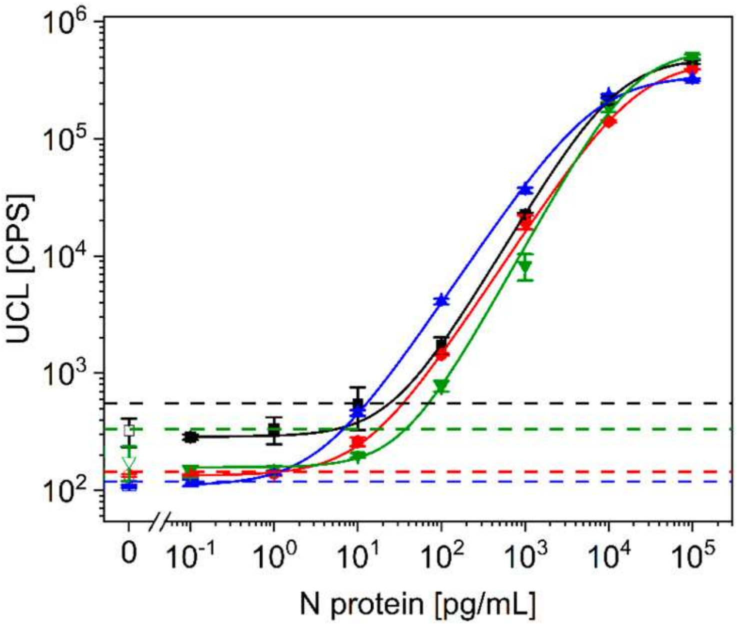

***Figure 2**. Calibration curves of the analog ULISA for the detection of wildtype N protein using different combinations of capture (c.a.) and biotinylated detection antibodies (d.a.). Black curve: c.a. 706, 524; d.a. 518, 715 (LOD 24 pg/mL). Green curve: c.a. 518, 706; d.a. 524, 715 (LOD 37 pg/mL). Red curve: c.a. 524, 715; d.a. 518, 706 (LOD 1.2 pg/mL). Blue curve: c.a. 518, 715; d.a. 524, 706 (LOD 0.33 pg/mL). The error bars represent the standard deviations of three replicate measurements. The hatched lines indicate three times the standard deviation of the background signal above the baseline of the regression curve.*

We discussed earlier that the association rates (k_{on}) of antibody binding are more relevant for the performance of immunoassay since the dissociation rates (k_{off}) are diminished by surface retention at the microtiter plate.[15] SPR measurements showed that the two capture antibodies C715 and C518 had higher relative k_{on} rates than the detection antibodies C524 and C706 (**Figure S2**), which indicates that the capture efficiency is more strongly dependent on the antibody affinities than the detection efficiency. This optimal antibody combination was used in all further experiments.

Under the same experimental conditions, we replaced the streptavidin-UCNP label by streptavidin-conjugated horseradish peroxidase to implement a conventional microtiter plate ELISA as a reference method. The ELISA was approximately 1000-fold less sensitive (LOD: 347 pg/mL; **Figure 3**) than the ULISA. The ELISA is also more laborious because it requires two additional steps for adding TMB substrate solution and stopping solution, which prolong the assay protocol and time.

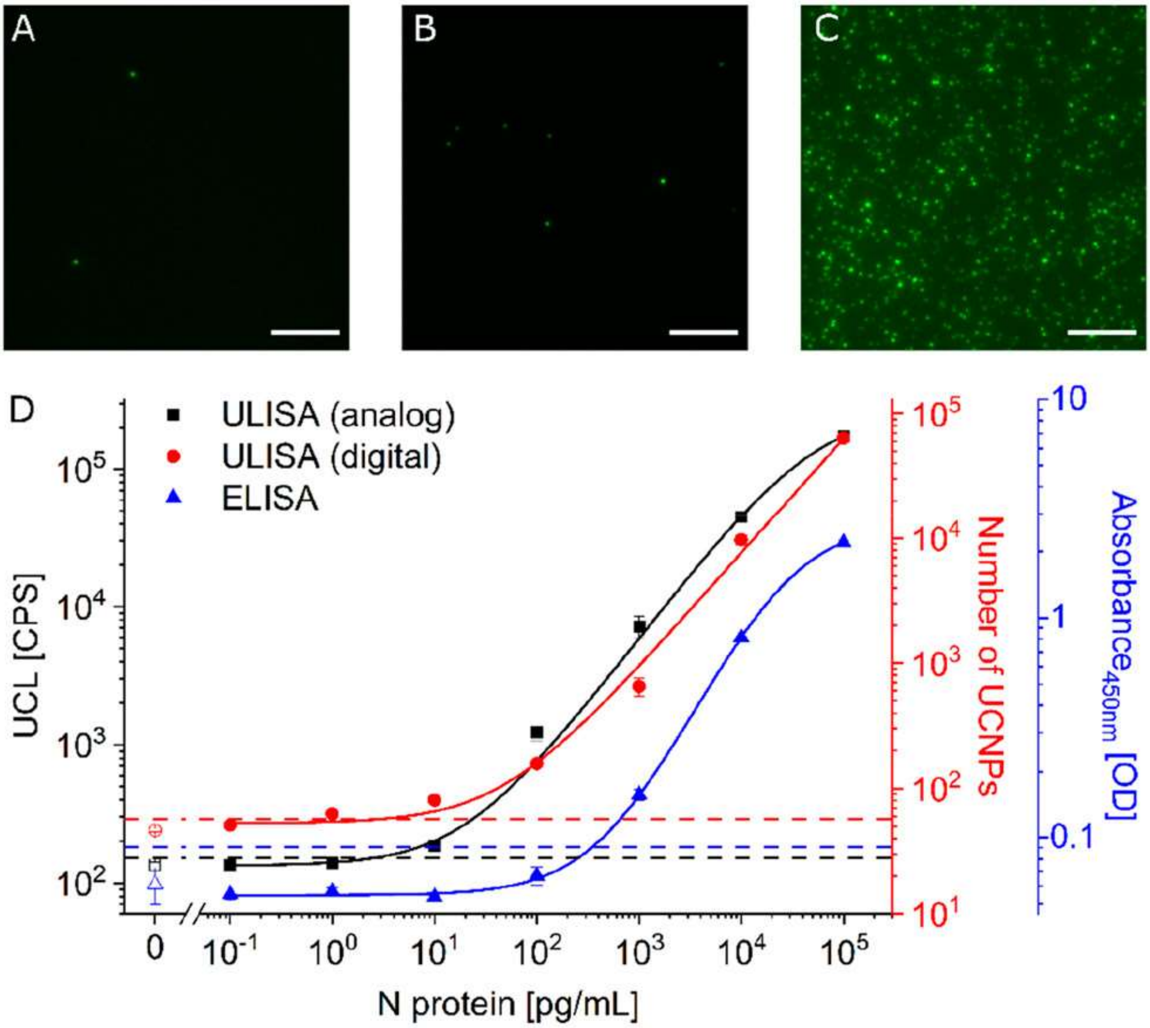

***Figure 3**. (A–C) Wide-field upconversion microscopy image sections (50 µm × 50 µm, scale bar: 10 µm) of the digital ULISA showing wildtype N protein concentrations of (A) 0 pg/mL, (B) 1000 pg/mL, and (C) 100,000 pg/mL. (D) Calibration curves of analog ULISA (black, LOD: 1.4 pg/mL), digital ULISA (red, LOD: 2.7 pg/mL), and ELISA (blue, LOD: 347 pg/mL). The error bars show the standard deviation of three replicate measurements. The hatched lines indicate three times the standard deviation of the background signal above the baseline of the regression curve.*

7.4.2 Comparison of analog and digital readouts

The ULISA and ELISA measurements described in the previous section are based on signal integration within the entire detection area, which is denoted as an analog readout. By contrast, so-called digital immunoassays rely on counting individual immune complexes. Enzyme labels generate large numbers of product molecules that typically diffuse within the whole volume of a microtiter plate well and, thus, are not amenable to a digital readout unless product diffusion is efficiently prevented. For example, a digital ELISA has been implemented by separating the diffusion volume of thousands of enzyme-labeled immune complexes in large arrays of femtoliter-sized reaction wells.[26] The digital ELISA achieved an LOD of 0.02 pg/mL for the detection of N protein,[20] which is more than 10 times lower than the LOD obtained with the ULISA utilizing the best antibody combination. The authors noted that the LOD of the digital ELISA mainly depended on differences in the affinities of capture and detection antibodies because there was a wide range of LODs when measuring other SARS-CoV-2 antigen concentrations (spike protein: 70 pg/mL; spike protein subunit S1: 5 pg/mL).[20]

In the ULISA, however, individual immune complexes are directly linked to signal-generating UCNP labels, which can be counted as diffraction-limited spots in a conventional 96-well microtiter plate format under a wide-field upconversion microscope. **Figure 3** shows examples of microscope images taken for the digital ULISA and the calibration curves of all three types of immunoassays.

Nonspecific binding of the UCNP label is detrimental for both the analog and the digital readout. Thus, we have optimized blocking conditions and the surface architecture of UCNPs to reduce nonspecific binding as efficiently as possible. **Figure 3A** shows a representative image of the blank sample with two nonspecific binding events, which adds up to 46 nonspecific binding events in the total area of nine images (0.2 mm^2). With this number of counting events, the Poisson noise is 15%, which is larger than the variation between repeated measurements (experimental error: 3%, **SI Table 1**).

Both the analog and digital readouts benefit from the detection of UCNP labels without optical background interference, which explains the much higher sensitivity of the ULISA compared to the ELISA. Compared to the analog readout, the digital

ULISA did not further improve the LOD, which we also observed earlier when developing a ULISA for the detection of troponin.[16] Independent of the analog or digital readout, however, the detection of the N protein was 5-fold more sensitive than the detection of troponin, which confirms the role of the antibody affinity and the importance of finding the best antibody combination to achieve an optimal assay performance.

7.4.3 Analysis of SARS-CoV-2 in cell culture fluid and in nasopharyngeal swabs

The N protein is, in principle, the optimal antigen for implementing COVID-19 immunoassays because it is the most abundant viral protein. This antigen, however, is not exposed on the viral surface and has to be released from the virus interior to be detectable. When testing different buffer compositions for the lysis of SARS-CoV-2 in culture fluid, we found that the lysis buffers strongly influenced the sensitivity of virus detection by the ULISA (**Figure S4A**). Among the two commercial buffers recommended for the use in LFA antigen tests, Lysis-Sing led to the most efficient release of the N protein and resulted in an LOD of 2 $TCID_{50}$/mL, whereas Lysis-X led to a 60-fold worse performance. The lysis buffers prepared according to the protocols in the literature (Lysis-Guan and Lysis-X) were originally developed for releasing RNA from the virus capsids and PCR detection and resulted in an intermediate performance between the commercial buffers. When we preincubated the recombinant N protein for 20 min either with the optimal buffer Lysis-Sing or with Tris assay buffer only, these samples showed the same ULISA results (**Figure S4B**), and no interference of the lysis buffer with the immunoassay components was observable. A commercial rapid antigen test was positive too, even though at relatively high virus concentrations of >1000 $TCID_{50}$/mL (**Figure S5**). Thus, we used Lysis-Sing for all further virus measurements.

Figure 4 shows that the ULISA measured N protein concentrations in the virus lysate (alpha variant) with a 2000-fold lower LOD than the ELISA, which is comparable to the difference observed in the detection of the recombinant N protein (**Figure 3**). In the case of the virus lysate, however, the digital readout further improved the virus detection by 1 order of magnitude (LOD: 0.08 $TCID_{50}$/mL). The antibody manufacturer reported that the antibodies have a higher specificity for the alpha variant of the N protein containing four amino acid mutations D3L/R203K/G204R/S235F (located outside the epitope binding regions N47-A173 of the antibodies) compared to the full-length wildtype N protein equipped with a C-terminal GS linker and a His10-tag.[24] This result supports our initial hypothesis that a strong antigen–antibody interaction is required in the first place before the digital readout can further improve the ULISA sensitivity.

Next, we measured the virus load in nasal swabs during an active infection with SARS-CoV-2, which was confirmed by parallel LFA measurements. Nasopharyngeal swabs were collected using cotton swabs and processed in Lysis-Sing 1 day after the first corona-related symptoms. **Figure 4E** shows the time course of convalescence. The virus load was highest on day 1 and gradually decreased in the following days. While the ULISA showed a clearly positive response (UCL) after 5 days (190 CPS vs background of 133 CPS), the LFA was already negative on days four and five (**Figure S6**). The higher sensitivity of the ULISA thus enables the surveillance of an infection over a longer time than commercial home tests. Additionally, quantitative information on the virus load can be obtained, while the LFA only allows for a yes/no decision on an infection.

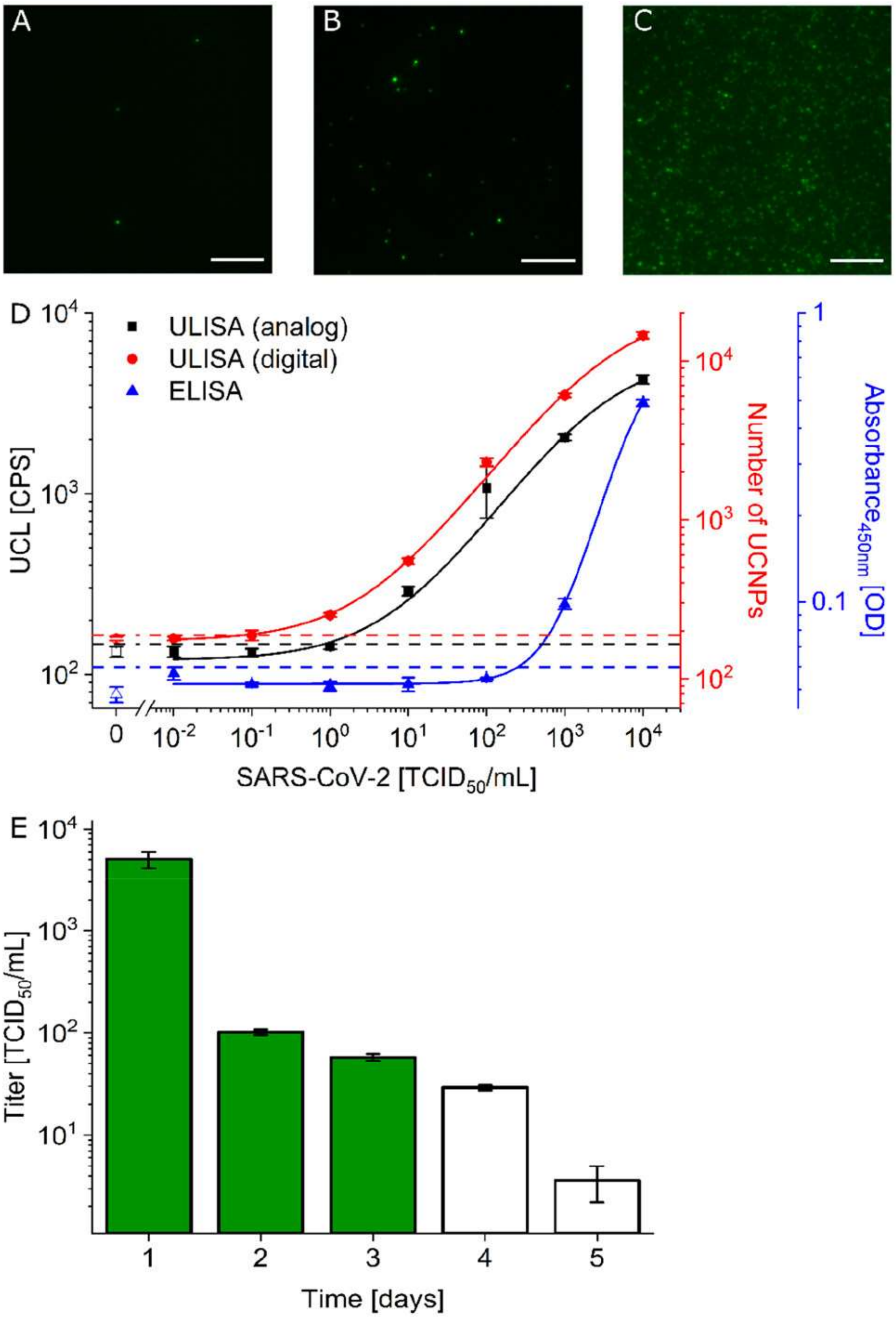

Figure 4. *(A–C) Wide-field upconversion microscopy image sections (50 µm × 50 µm, scale bar: 10 µm) of the digital ULISA showing SARS-CoV-2 (alpha variant) concentrations of (A) 0 TCID$_{50}$/mL, (B) 10^3 TCID$_{50}$/mL, and (C) 10^5 TCID$_{50}$/mL. (D) Calibration curves of the analog ULISA (black, LOD: 0.8 TCID$_{50}$/mL), digital ULISA (red, LOD: 0.08 TCID$_{50}$/mL), and ELISA (blue, LOD: 225 TCID$_{50}$/mL) for the detection of SARS-CoV-2. (E) Time course of virus load in nasopharyngeal swabs after the onset of COVID-19-related symptoms (day 0) as determined by the analog ULISA (based on black calibration curve in 4D). Full bars indicate that additionally the reference LFA was positive and empty bars that the LFA was negative. Error bars show the standard deviation of three replicate measurements.*

7.4.4 Comparison of ULISA with other SARS-CoV-2 tests

Table 1 summaries the LODs obtained by ULISA, ELISA, and LFA for the detection of both N protein and SARS-CoV-2 isolated from culture fluid. Compared to our assay results, standard electrochemical immunoassays feature similar sensitivities (LOD: 227 pg/mL)[27] as the ELISA. By contrast, the ULISA is more comparable to an immunoassay based on electroluminescence with an additional enhancement step (MSD S-PLEX SARS-CoV-2 N assay kit),[28] which was denoted as ultrasensitive (LOD: 0.16 pg/mL). The SIMOA platform, which includes an intrinsic preconcentration step on magnetic beads, enables the most sensitive N protein detection reported so far (LOD: 0.02 pg/mL).[20,29] As mentioned earlier, however, it should be noted that the LODs also depend on antibody affinities and do not purely reflect the performance of the assay platform.

***Table 1**. LODs of immunoassays for detection of N protein and SARS-CoV-2 in virus lysates*

Method	**N protein (pg/mL)**	**SARS-CoV-2 ($TCID_{50}$/mL)**
Analog ULISA	1.4	0.8
Digital ULISA	2.7	0.08
ELISA	347	225
Commercial LFA	*n.d.*[a]	>1000

[a]*n.d.*: not determined.

The comparison of different assay platforms based on the $TCID_{50}$/mL obtained with different virus preparations is even more difficult because the $TCID_{50}$ strongly depends on the virus inactivation process. As shown in **Figure S4**, the LOD varies additionally depending on how efficient the N protein is released from the virus. A capacitive biosensor using vertically paired electrodes reported a similar LOD as the ELISA (LOD: 147 $TCID_{50}$/mL).[30] Finally, an LFA for N protein detection was similar in sensitivity (650 pg/mL or 3030 pg depending on the source of N protein)[31] as the LFAs used for our reference experiments and enabled the detection of 4 $TCID_{50}$/swab, which was equivalent to 25,000 virus copies/swab.[32]

RT-PCR is typically more time consuming than optical detection assays and in principle can amplify a single RNA strand to a measurable signal, which may return a positive test result long after an individual has ceased to be infectious. The ULISA fills a niche because it is more sensitive than available LFAs but less sensitive than RT-PCR and thus may report on the acute status of patient infectivity more precisely.

7.5 Conclusions

Consistent with our earlier studies on PSA[11,33] and troponin,[16] the ULISA improved the detection of both N protein and SARS-CoV-2 by about 3 orders of magnitude. While the sensitivity of wildtype N protein detection was independent of the analog or digital readout, the digital ULISA improved the detection of SARS-CoV-2 in virus lysates further by a factor of 10. These different performance characteristics may result from the stronger antibody–antigen interaction of the alpha variant N protein compared to the recombinant wildtype N protein, which supports our hypothesis that a strong antigen–antibody interaction is a first requirement before the digital readout can further boost the ULISA sensitivity. However, even in the analog mode, the ULISA clearly outperforms the ELISA not only in terms of a much lower LOD, but also in terms of a wider signal-to-background ratio and fewer assay steps. The higher sensitivity of the ULISA enables early diagnosis and thus lowers the probability of further spreading an infection. Furthermore, the ULISA is relatively easy to perform and can be adapted to other diagnostically relevant biomarkers.

Acknowledgments

This study was supported by the German Research Foundation (DFG, GO 1968/6-2). A.H., Z.F., and P.S. acknowledge Grant 21-03156S from the Czech Science Foundation. We acknowledge CF Nanobiotechnology of CIISB, Instruct-CZ Centre, supported by MEYS CR (LM2018127). N.J. acknowledges the Operational Program Knowledge Education Development (POWR.03.02.00-00-I020/17), which is cofinanced by the European Union through the European Social Fund.

Notes

The authors declare no competing financial interest.

7.6 References

1. Perez-Reche F. J.; Forbes K. J.; Strachan N. J. C. Importance of untested infectious individuals for interventions to suppress COVID-19. *Sci. Rep*. **2021**, *11* (1), 20728. 10.1038/s41598-021-00056-5.

2. Fröberg J.; Gillard J.; Philipsen R.; Lanke K.; Rust J.; van Tuijl D.; Teelen K.; Bousema T.; Simonetti E.; van der Gaast-de Jongh C. E.; Bos M.; van Kuppeveld F. J.; Bosch B. J.; Nabuurs-Franssen M.; van der Geest-Blankert N.; van Daal C.; Huynen M. A.; de Jonge M. I.; Diavatopoulos D. A. SARS-CoV-2 mucosal antibody development and persistence and their relation to viral load and COVID-19 symptoms. *Nat. Commun*. **2021**, *12* (1), 5621. 10.1038/s41467-021-25949-x.

3. Lee J.; Song J. U.; Shim S. R. Comparing the diagnostic accuracy of rapid antigen detection tests to real time polymerase chain reaction in the diagnosis of SARS-CoV-2 infection: A systematic review and meta-analysis. *J. Clin. Virol*. **2021**, *144*, 104985. 10.1016/j.jcv.2021.104985.

4. van den Beld M. J. C.; Murk J. L.; Kluytmans J.; Koopmans M. P. G.; Reimerink J.; van Loo I. H. M.; Wegdam-Blans M. C. A.; Zaaijer H.; GeurtsvanKessel C.; Reusken C. Increasing the efficiency of a national laboratory response to COVID-19: a nationwide multicenter evaluation of 47 commercial SARS-CoV-2 immunoassays by 41 laboratories. *J. Clin. Microbiol*. **2021**, *59* (9), e0076721 10.1128/JCM.00767-21.

5. Li X. W.; Xiong M. Y.; Deng Q. L.; Guo X. B.; Li Y. R. The utility of SARS-CoV-2 nucleocapsid protein in laboratory diagnosis. *J. Clin. Lab. Anal*. **2022**, *36* (7), e24534 10.1002/jcla.24534.

6. Liotti F. M.; Menchinelli G.; Lalle E.; Palucci I.; Marchetti S.; Colavita F.; La Sorda M.; Sberna G.; Bordi L.; Sanguinetti M.; Cattani P.; Capobianchi M. R.; Posteraro B. Performance of a novel diagnostic assay for rapid SARS-CoV-2 antigen detection in nasopharynx samples. *Clin. Microbio. Infect*. **2021**, *27* (3), 487–488. 10.1016/j.cmi.2020.09.030.

7. Kabay G.; DeCastro J.; Altay A.; Smith K.; Lu H. W.; Capossela A. M.; Moarefian M.; Aran K.; Dincer C. Emerging biosensing technologies for the diagnostics of viral infectious diseases. *Adv. Mater*. **2022**, *34* (30), 2201085. 10.1002/adma.202201085.

8. Yuan H.; Chen P.; Wan C.; Li Y.; Liu B. F. Merging microfluidics with luminescence immunoassays for urgent point-of-care diagnostics of COVID-19. *Trends Anal. Chem*. **2022**, *157*, 116814. 10.1016/j.trac.2022.116814.

9. Resch-Genger U.; Gorris H. H. Perspectives and challenges of photon-upconversion nanoparticles - Part I: routes to brighter particles and quantitative spectroscopic studies. *Anal. Bioanal. Chem*. **2017**, *409* (25), 5855–5874. 10.1007/s00216-017-0499-z.

10. Gorris H. H.; Resch-Genger U. Perspectives and challenges of photon-upconversion nanoparticles - Part II: bioanalytical applications. *Anal. Bioanal. Chem*. **2017**, *409* (25), 5875–5890. 10.1007/s00216-017-0482-8.

11. Mickert M. J.; Farka Z.; Kostiv U.; Hlaváček A.; Horák D.; Skládal P.; Gorris H. H. Measurement of sub-femtomolar concentrations of prostate-specific antigen through single-molecule counting with an upconversion-linked immunosorbent assay. *Anal. Chem*. **2019**, *91* (15), 9435–9441. 10.1021/acs.analchem.9b02872.

12. Sedlmeier A.; Hlaváček A.; Birner L.; Mickert M. J.; Muhr V.; Hirsch T.; Corstjens P. L. A. M.; Tanke H. J.; Soukka T.; Gorris H. H. Highly sensitive laser scanning of photon-upconverting

nanoparticles on a macroscopic scale. *Anal. Chem*. **2016**, *88* (3), 1835–1841. 10.1021/acs.analchem.5b04147.

13. Hlaváček A.; Farka Z.; Mickert M. J.; Kostiv U.; Brandmeier J. C.; Horák D.; Skládal P.; Foret F.; Gorris H. H. Bioconjugates of photon-upconversion nanoparticles for cancer biomarker detection and imaging. *Nat. Prot*. **2022**, *17* (4), 1028–1072. 10.1038/s41596-021-00670-7.

14. Farka Z.; Mickert M. J.; Pastucha M.; Mikušová Z.; Skládal P.; Gorris H. H. Advances in optical single-molecule detection: En route to supersensitive bioaffinity assays. *Angew. Chem. Int. Edit* **2020**, *59* (27), 10746–10773. 10.1002/anie.201913924.

15. Gorris H. H.; Soukka T. What digital immunoassays can learn from ambient analyte theory: A perspective. *Anal. Chem*. **2022**, *94* (16), 6073–6083. 10.1021/acs.analchem.1c05591.

16. Brandmeier J. C.; Raiko K.; Farka Z.; Peltomaa R.; Mickert M. J.; Hlaváček A.; Skládal P.; Soukka T.; Gorris H. H. Effect of particle size and surface chemistry of photon-upconversion nanoparticles on analog and digital immunoassays for cardiac troponin. *Adv. Healthc. Mater*. **2021**, *10* (18), 2100506. 10.1002/adhm.202100506.

17. Alexaki K.; Kyriazi M. E.; Greening J.; Taemaitree L.; El-Sagheer A. H.; Brown T.; Zhang X. L.; Muskens O. L.; Kanaras A. G. A SARS-CoV-2 sensor based on upconversion nanoparticles and graphene oxide. *RSC Adv*. **2022**, *12* (29), 18445–18449. 10.1039/D2RA03599E.

18. Balinski B.Australian-made COVID-19 test returns results within minutes. Create. https://createdigital.org.au/australian-made-covid-19-test-results-within-minutes/.

19. Makhneva E.; Sklenárová D.; Brandmeier J. C.; Hlaváček A.; Gorris H. H.; Skládal P.; Farka Z. Influence of Label and Solid Support on the Performance of Heterogeneous Immunoassays. *Anal. Chem*. **2022**, *94* (47), 16376–16383. 10.1021/acs.analchem.2c03543.

20. Ogata A. F.; Maley A. M.; Wu C.; Gilboa T.; Norman M.; Lazarovits R.; Mao C. P.; Newton G.; Chang M.; Nguyen K.; Kamkaew M.; Zhu Q.; Gibson T. E.; Ryan E. T.; Charles R. C.; Marasco W. A.; Walt D. R. Ultra-sensitive serial profiling of SARS-CoV-2 antigens and antibodies in plasma to understand disease progression in COVID-19 patients with severe disease. *Clin. Chem*. **2020**, *66* (12), 1562–1572. 10.1093/clinchem/hvaa213.

21. Lahtinen S.; Lyytikäinen A.; Päkkilä H.; Hömppi E.; Perälä N.; Lastusaari M.; Soukka T. Disintegration of hexagonal $NaYF_4$:Yb^{3+},Er^{3+} upconverting nanoparticles in aqueous media: The role of fluoride in solubility equilibrium. *J. Phys. Chem. C* **2017**, *121* (1), 656–665. 10.1021/acs.jpcc.6b09301.

22. Boom R.; Sol C. J. A.; Salimans M. M. M.; Jansen C. L.; Wertheimvandillen P. M. E.; Vandernoordaa J. Rapid and simple method for purification of nucleic-acids. *J. Clin. Microbiol.* **1990**, *28* (3), 495–503. 10.1128/jcm.28.3.495-503.1990.

23. Shatzkes K.; Teferedegne B.; Murata H. A simple, inexpensive method for preparing cell lysates suitable for downstream reverse transcription quantitative PCR. *Sci. Rep*. **2014**, *4*, 4659. 10.1038/srep04659.

24. HyTest SARS-CoV-2 antibodies and detection of variants. HyTest. https://shop.hytest.fi/spree/products/4156/SARS-CoV-2_detection_of_variants.pdf?1648709822.

25. Hytest TechNotes: Reagents of SARS-CoV-2 antigen and antibody assays. HyTest. https://hytest.fi/sites/5cd13840ff4f702c0cbc4c8d/content_entry5cd13897ff4f702c0cbc4cb2/5f09b34cff4f703a3f35bdf3/files/SARS-CoV-2_TechNotes.pdf?1647263232.

26. Rissin D. M.; Kan C. W.; Campbell T. G.; Howes S. C.; Fournier D. R.; Song L.; Piech T.; Patel P. P.; Chang L.; Rivnak A. J.; Ferrell E. P.; Randall J. D.; Provuncher G. K.; Walt D. R.; Duffy D. C. Single-molecule enzyme-linked immunosorbent assay detects serum proteins at subfemtomolar concentrations. *Nat. Biotechnol*. **2010**, *28* (6), 595–599. 10.1038/nbt.1641.

27. Białobrzeska W.; Ficek M.; Dec B.ło.; Osella S.; Trzaskowski B.; Jaramillo-Botero A.; Pierpaoli M.; Rycewicz M.ł; Dashkevich Y.; Łega T.; Malinowska N.; Cebula Z.; Bigus D.; Firganek D.; Biega E.; Dziabowska K.; Brodowski M.; Kowalski M.; Panasiuk M.ła.; Gromadzka B.; Zołedowska S.; Nidzworski D.; Pyrc K.; Goddard W. A.; Bogdanowicz R. Performance of electrochemical immunoassays for clinical diagnostics of SARS-CoV-2 based on selective nucleocapsid N protein detection: Boron-doped diamond, gold and glassy carbon evaluation. *Biosens. Bioelectron*. **2022**, *209*, 114222. 10.1016/j.bios.2022.114222.

28. Pollock N. R.; Savage T. J.; Wardell H.; Lee R. A.; Mathew A.; Stengelin M.; Sigal G. B. Correlation of SARS-CoV-2 nucleocapsid antigen and RNA concentrations in nasopharyngeal samples from children and adults using an ultrasensitive and quantitative antigen assay. *J. Clin. Microbiol*. **2021**, *59* (4), e03077-20 10.1128/JCM.03077-20.

29. Cai Q.; Mu J.; Lei Y.; Ge J.; Aryee A. A.; Zhang X.; Li Z. Simultaneous detection of the spike and nucleocapsid proteins from SARS-CoV-2 based on ultrasensitive single molecule assays. *Anal. Bioanal. Chem*. **2021**, *413* (18), 4645–4654. 10.1007/s00216-021-03435-z.

30. Park J. H.; Lee G. Y.; Song Z.; Bong J. H.; Chang Y. W.; Cho S.; Kang M. J.; Pyun J. C. Capacitive biosensor based on vertically paired electrodes for the detection of SARS-CoV-2. *Biosens. Bioelectron*. **2022**, *202*, 113975. 10.1016/j.bios.2022.113975.

31. Grant B. D.; Anderson C. E.; Williford J. R.; Alonzo L. F.; Glukhova V. A.; Boyle D. S.; Weigl B. H.; Nichols K. P. SARS-CoV-2 coronavirus nucleocapsid antigen-detecting half-strip Lateral Flow Assay toward the development of point of care tests using commercially available reagents. *Anal. Chem.* **2020**, *92* (16), 11305–11309. 10.1021/acs.analchem.0c01975.

32. Grant B. D.; Anderson C. E.; Alonzo L. F.; Garing S. H.; Williford J. R.; Baughman T. A.; Rivera R.; Glukhova V. A.; Boyle D. S.; Dewan P. K.; Weigl B. H.; Nichols K. P. A SARS-CoV-2 coronavirus nucleocapsid protein antigen-detecting lateral flow assay. *PLoS One* **2021**, *16* (11), e0258819 10.1371/journal.pone.0258819.

33. Farka Z.; Mickert M. J.; Hlaváček A.; Skládal P.; Gorris H. H. Single molecule upconversion-linked immunosorbent assay with extended dynamic range for the sensitive detection of diagnostic biomarkers. *Anal. Chem*. **2017**, *89* (21), 11825–11830. 10.1021/acs.analchem.7b03542.

7.7 Supporting information

7.7.1 Synthesis of UCNPs

YCl_3 × 6 H_2O (874 mg, 2.88 mmol), $YbCl_3$ × 6 H_2O (251 mg, 0.648 mmol), and $ErCl_3$ × 6 H_2O (27.5 mg, 0.072 mmol) were dissolved in 30 mL of methanol and added into a 250-mL three-neck round-bottom flask containing 27 mL (24.2 g) of oleic acid and 63 mL (49.7 g) of 1- octadecene. The solution was heated to 170 °C under a protective nitrogen atmosphere until all volatile liquids were evaporated (ca. 60 min). After the temperature had decreased to 50 °C, the nitrogen atmosphere was disconnected, and a solution of 533 mg (14.4 mmol) of NH_4F and 360 mg (9 mmol) of NaOH in 30 mL of methanol was added under intense stirring. The nitrogen atmosphere was reconnected, and the solution was stirred for 30 min. The temperature was carefully increased up to 150 °C, avoiding extensive boiling to ensure the evaporation of methanol. After that, the solution was rapidly heated at the rate of ca. 10 °C/min. At 290 °C, the heating was carefully adjusted to 300 °C within one or two minutes. The flask was kept under nitrogen flow at 300 °C (± 4 °C) for 90 min and then let to cool down to RT. The emerging UCNPs were precipitated by adding 180 mL of propan-2-ol and collected by centrifugation (1,000 g, 10 min). The precipitate was washed with 90 mL of methanol, centrifuged (1,000 g, 10 min) and redispersed in 20 mL of cyclohexane. After adding 100 mL of methanol, the UCNPs precipitated rapidly without centrifugation. The precipitate was redispersed in 30 mL of cyclohexane and slowly centrifuged (50 g, 20 min) to separate solid compounds from the final UCNPs.

Under reflux, Y_2O_3 (1355 mg, 6.00 mmol), Yb_2O_3 (532 mg, 1.35 mmol) and Er_2O_3 (57.9 mg, 0.15 mmol) were dissolved in trifluoroacetic acid (12 mL) and water (12 mL) in a 250-mL three-necked flask. When dissolved, $NaHCO_3$ (1260 mg, 15.00 mmol) was added, releasing CO_2 bubbles and dissolving rapidly, resulting in a clear solution. After removing the condenser, excessive trifluoroacetic acid and water were evaporated by heating at 110 °C in a fume hood (overnight). The resulting white powder of trifluoroacetates was dissolved in oleic acid (45 mL, 40.3 g) and octadec-1-ene (45 mL, 35.5 g). This solution was diluted by 30 mL of methanol. The methanol together with oxygen and water were removed by heating at 110 °C under the N_2 atmosphere for 20 min, resulting in a precursor solution. The precursor solution was enclosed in the flask by silicon septa and kept under an inert atmosphere. To decrease the viscosity, the precursor solution was kept at an elevated temperature (ca. 50 °C), which facilitated its injection into the hot reaction mixture. The concentration of $Re(CF_3CO_2)_3$ in the precursor solution was 0.17 mmol/mL (Re for Y, Yb, Er in molar percentages 80%, 18% and 2.0%, respectively.

The nanoparticles were grown by gradually adding the precursor solution to the solution of seed nanoparticles. The dispersion of seed nanoparticles (205 mg) in cyclohexane was mixed with oleic acid (5.5 mL, 4.9 g), octadec-1-ene (17 mL, 13.4 g), and 20 mL of methanol in a 100-mL three-necked flask. The mixture was heated at 150 °C for ~30 min under the nitrogen atmosphere to remove oxygen and water. Then, the temperature was rapidly increased to 300 °C. Keeping this temperature, a syringe with a long needle was used to inject the precursor solution nine times (respective volumes: 3.5, 4.0, 4.6, 5.6, 6.2, 7.1, 8.3, 9.6 and 10.1 mL), each with a delay of 10 min. After this, the 100-mL flask was full, and the reaction mixture was transferred to a 250-mL three-necked flask together with 30 mL of methanol. The solution was heated to 150 °C for ~30 min under an inert nitrogen atmosphere to remove oxygen, methanol and water. The temperature was rapidly increased to 300 °C, and the 9-fold injection or precursor solution was repeated; the temperature was kept at 300 °C for 10 min, eventually preparing nanoparticles of the desired size (reaction mixture volume ~82 mL), and the synthesis continued without decreasing the temperature by growing the inert shell of $NaYF_4$.

Under reflux, Y_2O_3 (1694 mg, 7.50 mmol) was dissolved in trifluoroacetic acid (12 mL) and water (12 mL) in a 250-mL three-necked flask. When dissolved, $NaHCO_3$ (1260 mg, 15.00 mmol) was added, releasing CO_2 bubbles and dissolving rapidly to a clear solution. After removing the condenser, excessive trifluoroacetic acid and water were evaporated by heating at 110 °C in a fume hood (overnight). The resulting white powder of trifluoroacetates was dissolved in oleic acid (45 mL, 40.3 g) and octadec-1-ene (45 mL, 35.5 g). This solution was diluted by 30 mL of methanol. The methanol together with oxygen and water were removed by heating at 110 °C under an inert nitrogen atmosphere for 20 min, resulting in a precursor solution. The precursor solution was enclosed in the flask by a silicon septum and kept under an inert atmosphere. To decrease the viscosity, the precursor solution was held at ~50 °C, which facilitated its injection into the hot reaction mixture. The precursor solution contained 0.17 mmol/mL of $Y(CF_3CO_2)_3$.

The shell was grown by gradually adding the precursor solution to the hot solution of grown nanoparticles from the previous step. A calculated amount of precursor solution was repeatedly injected by a syringe with a long needle (120 mm) without decreasing the temperature. The three additions were of 8.0, 9.0, and 10.0 mL; the interval between the injections was 10 min. After the last injection, the temperature was kept at 300 °C for an additional 10 min, eventually preparing the desired nanoparticles (the volume of the reaction mixture was ~95 mL). Finally, the flask was cooled to room temperature. The resulting nanoparticles were precipitated by adding propan-2-ol (190 mL) and collected by centrifugation (1,000 *g*, 10 min). The pellet was washed with methanol (109 mL), centrifuged (1,000 *g*, 10 min), and dispersed in cyclohexane (60 mL). After the last precipitation by methanol, the nanoparticles were dispersed in cyclohexane and slowly centrifuged (50 *g*, 20 min) to separate coarse particles from the final product.

7.7.2 Synthesis of alkyne-PEG-neridronate (alkyne-PEG-ner)

First, 30 mg of neridronate (Merck, Darmstadt, Germany) was dissolved in a mixture of 898 µL of PB (50 mM, pH 7.4) and 128 µL of 1 M NaOH under sonication. Then, 75 mg of Alkyne-PEG-NHS (α-N-hydroxysuccinimide-ω-alkyne polyethylene glycol, MW 3000; Iris Biotech, Marktredwitz, Germany) was added and incubated overnight at 4 °C. The reaction mixture was dialyzed against 4 L of bidistilled H_2O in a Float-A-Lyzer G2 dialysis device (MW cutoff = 500– 1000 Da, Fisher Scientific, Germany) at 4 °C for 96 hours; H2O was exchanged 12 times. The purified, colorless Alkyne-PEG-ner was lyophilized (Alpha 1-2, Christ, Osterode am Harz, Germany) and stored at 4 °C.

7.7.3 Characterization of UCNPs

Oleic acid-coated UCNPs dispersed in 5 µL of cyclohexane were dispensed on a copper grid coated with a 12-nm continuous carbon foil. A paper tissue was used to remove excess amounts of fluid, and the grid was dried on air. TEM images were recorded on a Titan Themis (FEI, Czech Republic). SA-PEG-UCNPs dispersed in 2 µL of water were dispensed on a copper grid covered with a holey carbon film. A paper tissue was used to remove excess amounts of fluid, and the grid was dried on air. TEM images were recorded on a HT7700 TEM (Hitachi, Japan).

The hydrodynamic diameter of UCNPs was determined on a Zetasizer Nano (Malvern, UK) using dynamic light scattering (DLS). Dispersions of 187 µg/mL of oleic acid-capped UCNPs in cyclohexane and 325 µg/mL of SA-PEG-UCNPs in 50 mM Tris were analyzed.

The emission spectrum of 30 mg/mL of oleic acid-coated UCNPs dispersed in cyclohexane was recorded by a self-made epiluminescence detector equipped with a 979-nm laser module (400 mW) and an excitation intensity of ~200 W/cm2.

7.7.4 Surface plasmon resonance (SPR) measurements of antibody affinities

An MP-SPR Navi 210A SPR system (Bionavis, Tampere, Finland) equipped with a 670-nm laser was used to scan the spectral angle between 58° and 78°. The shift of the SPR angle was determined using a centroid fitting function. mAbs C715, C518, C524 or C706, respectively, were immobilized on a commercial CMD200M SPR chip coated with carboxymethyl dextran to measure the binding kinetics of the N protein label-free and in real-time.

The running buffer consisting of 10 mM HEPES (Carl Roth, Karlsruhe, Germany), 150 mM NaCl and 0.01% Tween20 (pH 7.4) was degassed before each measurement. The chip surface was rinsed continuously with running buffer at a flow rate of 20 µL/min until a stable SPR signal was reached. Then, the surface was activated by pumping 0.2 M EDC and 0.05 M NHS (1:1) in water into the channels for 10 min. The respective antibodies in 50 mM acetate buffer (pH 4.5) were pumped for 20 min into the measurement channel at a flow rate of 10 µL/min. No antibody was inserted into the control channel. Subsequently, the surface was blocked for 5 min by 1 M of an aqueous ethanolamine solution (pH 8). The N protein (concentrations of 0.1, 1, 10, 100, 1000 ng/mL) in running buffer was applied at a flow rate of 20 µL/min until a stable, high binding signal was reached. Finally, the surface was regenerated using 10-100 mM of HCl for 2 min.

7.7.5 Biotinylation of monoclonal antibodies

A solution of 5 mg/mL of NHS-LC-biotin (Merck/Sigma-Aldrich, St. Louis, MO USA) in dry DMF was prepared. A solution of 95.4 µg of mAb in PBS was mixed with 1.15 µL of NHS-LC-biotin, and PBS was added to obtain a final volume of 84.3 µL. After the solution had been shaken for 10 min, another 1.15 µL of NHS-LC-biotin was added, and the reaction mixture was shaken for 2 h at RT. The biotinylated antibody was purified six times via centrifugation (14,000 g, 20 min) using Amicon ultra centrifugal filters (MWCO 100 kDa, Merck KGaA, Darmstadt, Germany), transferred to PBS and stored at 4 °C at a concentration of 1 mg/mL.

7.7.6 Preparation of buffers for the lysis of SARS-CoV-2

Reagents: Tris-HCl (Carl Roth); guanidinium thiocyanate (Sigma Aldrich); $Na_2EDTA \times 2\ H_2O$ (Carl Roth); Triton X-100 (Sigma Aldrich)

Lysis-Guan[1] (contains guanidinium thiocyanate as a chaotropic reagent)

Tris-HCl (5 mM) was dissolved in bidistilled H_2O under continuous stirring and adjusted to pH 6.4 using 0.1 M NaOH. Guanidinium thiocyanate (5 M) was added under ultrasonication at 65 °C. In a separate flask, $Na_2EDTA \times 2\ H_2O$ (50 mmol) was mixed with bidistilled H_2O, and NaOH pellets were added under continuous stirring until the EDTA was completely dissolved. The EDTA solution was adjusted to pH 8.0 with 0.1 M NaOH, filtered, and finally added to the guanidinium thiocyanate solution to obtain a final concentration of 22 mM of EDTA. Triton X-100 (1.2 wt/v) was added to the solution under shaking until the solution was homogenous.

Lysis-X[2] (contains only Triton-X 100 as a detergent)

NaCl (150 mM) and Tris-HCl (10 mM) were dissolved in bidistilled H2O under constant stirring. After adding Triton X-100 (0.25 %), the solution was homogenized under ultrasonication and adjusted to pH 7.4 using 0.1 M NaOH.

References:

(1) R. Boom, C. J. Sol, M. M. Salimans, C. L. Jansen, P. M. Wertheim-van Dillen, J. van der Noordaa (1990). Rapid and Simple Method for Purification of Nucleic Acids. J. Clin. Microbiol. 28, 495-503.

(2) K. Shatzkes, B. Teferedegne, H. Murata (2014). A Simple, Inexpensive Method for Preparing Cell Lysates Suitable for Downstream Reverse Transcription Quantitative PCR. Sci. Rep. 4, 4659.

7.7.7 Additional results

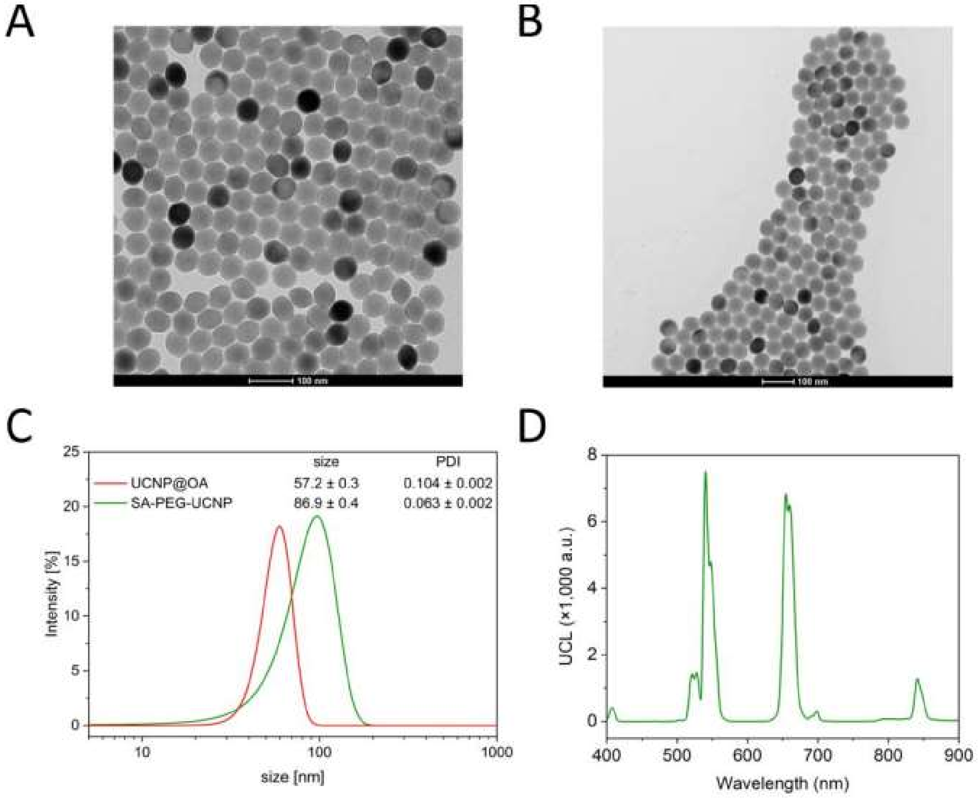

***Figure S1**. Characterization of UCNPs (NaYF4: 18% Yb, 2% Er / NaYF4, 58 nm in diameter): Transmission electron microscopy (TEM) images of (A) oleic acid-capped UCNPs and (B) SA-PEG-UCNPs, (C) dynamic light scattering (DLS), and (D) emission spectroscopy under 976-nm excitation.*

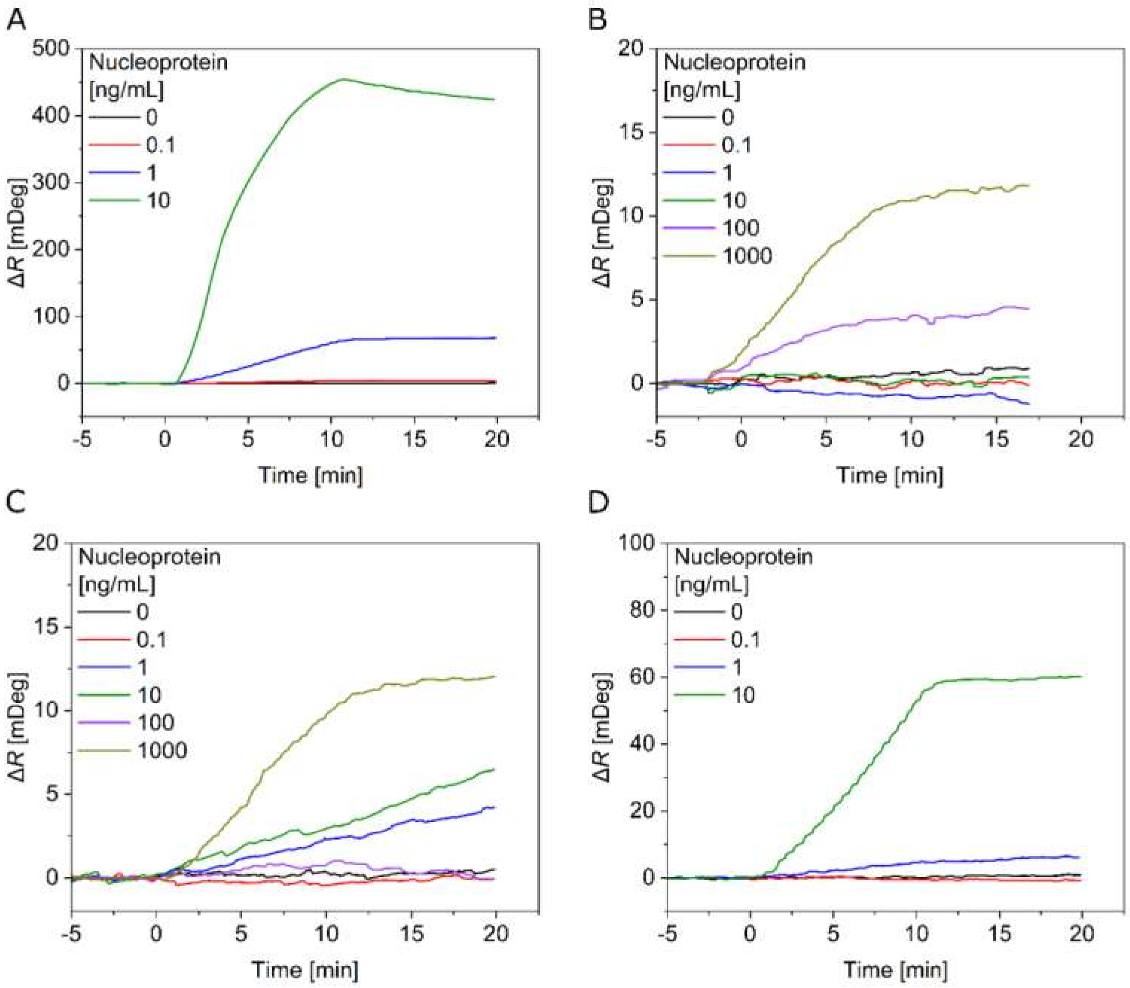

Figure S2*. SPR measurements of N protein binding by surface-immobilized mAbs A) C518, B) C524, C) C706 and D) C715. mAbs C518 and C715 show strong signal increases already at N protein concentrations of 10 ng/mL, while mAbs C524 and C706 require 100-fold higher N protein concentrations (1000 ng/mL) to show a similar signal response.*

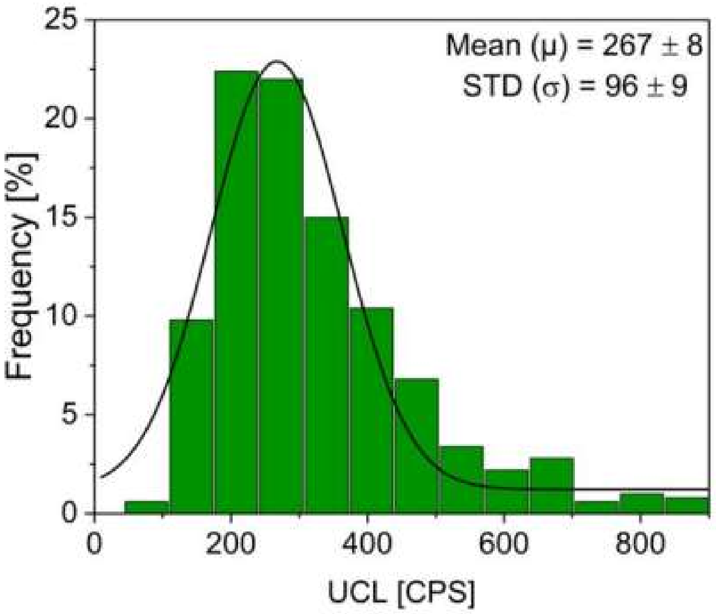

Figure S3. *Brightness distribution of individual diffraction limited spots taken at a viral concentration of 103 TCID50/mL under the wide-field upconversion microscope (Fig. 4).*

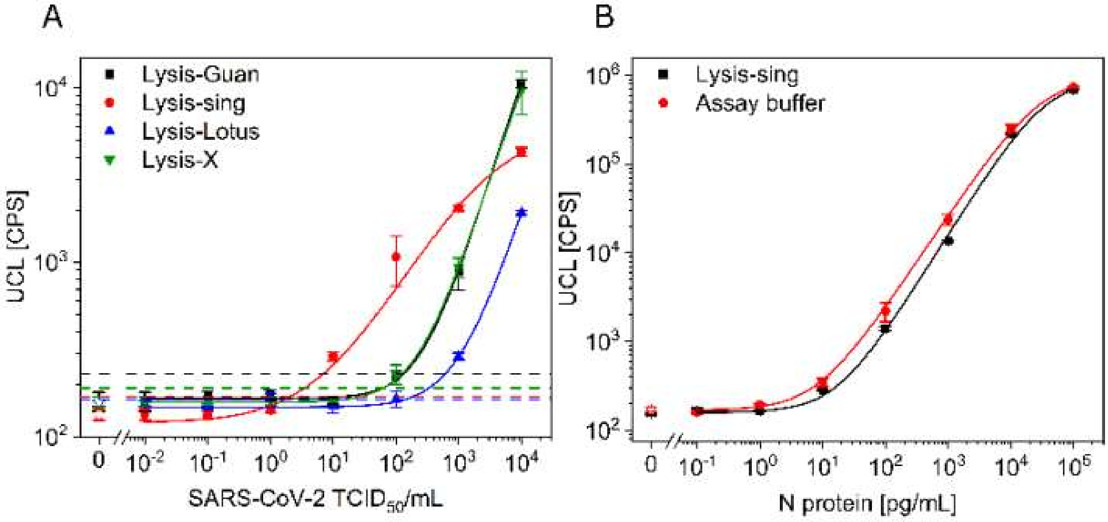

Figure S4. *A) Influence of different lysis buffers on the detection of SARS-CoV-2. Culture fluid was tenfold diluted in lysis buffers and further diluted in Tris assay buffer ($LOD_{Lysis\text{-}Guan}$: 131.8 $TCID_{50}$/mL; $LOD_{Lysis\text{-}Sing}$: 2.0 $TCID_{50}$/mL; $LOD_{Lysis\text{-}Lotus}$: 138.2 $TCID_{50}$/mL, $LOD_{Lysis\text{-}X}$: 63.3 $TCID_{50}$/mL). B) Influence of the optimal lysis buffer Lys-Sing on the detection of recombinant wildtype N protein. The N protein was tenfold diluted in Lysis-Sing (LOD: 1.2 pg/mL) or Tris assay buffer (LOD: 1.4 pg/mL), respectively, and further diluted in Tris assay buffer. Error bars represent the standard deviation of three replicate measurements.*

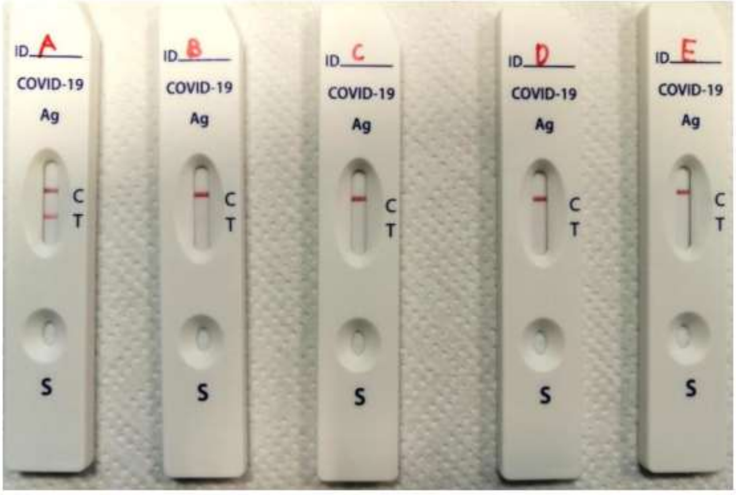

Figure S5. *Detection of SARS-CoV-2 using a commercial LFA for self-testing (Joinstar Biomedical Technology). Culture fluid was incubated with the supplied lysis buffer and dilutions of (A) 10^5 $TCID_{50}$/mL, (B) 10^3 $TCID_{50}$/mL, (C) 10^1 $TCID_{50}$/mL, (D) 10^{-1} $TCID_{50}$/mL, and (E) 0 $TCID_{50}$/mL were dispensed on the sample application pad (S). Viral concentrations of 10^5 $TCID_{50}$/mL led to a positive test result (red signal in T line), whereas lower concentrations remained undetected (no signal in T line).*

Figure S6. *Detection of SARS-CoV-2 using a commercial LFA for self-testing (New Gene Bioengineering). Nasopharyngeal swabs were collected and analyzed from day 1 to day 5 (from left to right) after the onset of symptoms. The LFA was negative after day 3.*

***Supporting Table 1**: Precision of the digital ULISA. The coefficient of variation (CV) was calculated by dividing the standard deviation of three wells by the average number of UCNPs per well. The Poisson noise was calculated by dividing the square root of the average number of UCNPs in an area of 0.2 cm^2 (9 images of 166 × 140 μm^2 combined) by the average number of UCNPs in that area ($\sqrt{n}/n$).*

	Concentration	*Average # of UCNPs*	*Experimental CV*	*Poisson noise*
blank	*0 pg/mL*	*46 ± 1*	*3.3%*	*14.7%*
N protein (wildtype) (Figure 3)	*0.1 pg/mL*	*51 ± 2*	*3.9%*	*14.0%*
	1 pg/mL	*70 ± 1*	*2.2%*	*12.0%*
	10 pg/mL	*92 ± 1*	*1.1%*	*10.4%*
	100 pg/mL	*160 ± 4*	*2.3%*	*8.0%*
	1,000 pg/mL	*690 ± 28*	*4.1%*	*3.8%*
	10,000 pg/mL	*9650 ± 28*	*9.0%*	*1.0%*
	100,000 pg/mL	*64000 ± 3800*	*5.9%*	*0.4%*
SARS-CoV-2 (alpha) (Figure 4)	*0.1 $TCID_{50}$/mL*	*178 ± 5*	*2.9%*	*7.5%*
	1 $TCID_{50}$/mL	*190 ± 13*	*7.4%*	*7.3%*
	10 $TCID_{50}$/mL	*250 ± 7*	*3.0%*	*6.3%*
	100 $TCID_{50}$/mL	*550 ± 23*	*4.3%*	*4.3%*
	1,000 $TCID_{50}$/mL	*2300 ± 140*	*6.0%*	*2.1%*
	10,000 $TCID_{50}$/mL	*6100 ± 170*	*2.8%*	*1.3%*
	100,000 $TCID_{50}$/mL	*14500 ± 690*	*4.7%*	*0.8%*

8 Article III

Upconversion-linked branched DNA hybridization assay for the detection of bacteriophage M13

Julian C. Brandmeier, Saara Kuusinen, Zdeněk Farka,
Tero Soukka, Hans H. Gorris

Reproduced with permission from:
Advanced Optical Materials. **2024**, *2402041*.

8.1 Abstract

The demand for highly sensitive methods of pathogen detection drives the development of new diagnostic assays. While nucleic acid amplification methods such as PCR are very sensitive and remain widely used, they may be limited in complex sample matrices due to the presence of polymerase inhibitors. On the other hand, the direct detection of nucleic acids by DNA hybridization assays is simple but typically less sensitive. This work combines a branched DNA (bDNA) hybridization assay with upconversion nanoparticle (UCNP) labels to enhance the sensitivity of DNA detection. The anti-Stokes emission of UCNP labels enables measurements without optical background interference. The bDNA assay relies on a series of oligonucleotide probes creating a branched structure with several binding sites for biotinylated amplification probes and streptavidin-conjugated UCNPs. We investigated several configurations of the bDNA assay to achieve the highest signal amplification and the lowest background signal. The optimal configuration of bDNA assay yielded a limit of detection (LOD) of 5.9×10^4 cfu/mL for the target DNA of the bacteriophage M13. The upconversion-linked bDNA assay is easily adaptable to other target DNAs by adjusting the oligonucleotide probes.

8.2 Introduction

The Covid-19 pandemic demonstrated that highly sensitive and easily adaptable bioanalytical methods are crucial to surveille, manage, and control the outbreak of viral diseases.[1] The demands of the method, including fast turnaround times, high specificity, exceptional sensitivity, and low cost, however, are very hard to achieve together. Conventional detection methods for viruses can be divided into two main classes:[1,2] The detection of viral proteins by immunoassays, such as enzyme-linked immunosorbent assay (ELISA) or lateral flow immunoassay, is fast, cheap, and suitable for point-of-care testing, but these assays are typically not sensitive enough for all applications.[4] On the other hand, the detection of viral RNA or DNA based on amplification by polymerase chain reaction (PCR) or other target amplification techniques is more sensitive, but also more complex, requires longer turnaround times, and is relatively expensive.[5,6]

The branched DNA assay (bDNA assay) for the direct - *i.e.* without target amplification - detection of viral RNA or DNA target strands is an important alternative for PCR-based methods.[7] bDNA assays are divided into three generations. In all cases, oligonucleotides (capture probes) immobilized on a solid surface capture the target DNA/RNA *via* hybridization.[8] First generation bDNA assays use label extender oligonucleotides that hybridize to the target and a branched DNA amplifier molecule. The amplifier then binds to several signal generation elements such as enzyme labels. Second generation bDNA assays involve an additional detection step after the label extenders: (1) a preamplifier that contains repeating hybridization sites for binding (2) several amplificant probes. This kind of branched detection system strongly amplifies the detection signal and improves the assay sensitivity. Finally, third generation bDNA assays employ non-natural nucleobases such as isoMeC and d-isoG for all oligonucleotides not involved in target hybridization to avoid nonspecific hybridization of the probes. The reduction of nonspecific hybridization together with a higher degree of signal amplification afforded by the second generation assay strongly improved the detection of HIV and HCV.[9,10]

For viral diagnostics, bDNA assays offer several advantages: Unlike PCR, bDNA assays do not require expensive equipment such as thermocyclers and avoid contamination issues related to target strand amplification and detection, as well as PCR inhibitors. They are also advantageous when amplification bias needs to be minimized.[11] As bDNA assays are a truly quantitative detection method, they provide accurate and reproducible information on the viral load, disease progression, and treatment, even in samples with a limited amount of starting material.[12] Their performance is robust even in complex biological matrices, including blood, serum, plasma or other body fluids, which are often encountered in clinical settings. This versatility has been useful for the detection of a wide range of viral diseases such as HIV, hepatitis viruses, herpesviruses, and respiratory viruses.[13–16] bDNA assays are particularly suitable for the detection of viruses with single-stranded genome because they only require a chemical rather than a thermal lysis. While bDNA assays are most common for the detection of viruses,[17] they have also been used for the detection of bacteria, parasites, and cancer cells.[7,18,19]

To further increase the sensitivity of bDNA assays, we took advantage of the unique optical properties of photon-upconversion nanoparticles (UCNPs). These lanthanide-doped nanocrystals emit shorter wavelength light under near-infrared (NIR) excitation light (anti-Stokes emission) and thus avoid autofluorescence and light scattering, which typically lead to a high optical background signal when using conventional labels.[20] As shown in our previous works, an up to 1,000-fold increase in assay sensitivity is possible by switching the detection label from conventional enzymes to UCNPs.[21–25]

Here, we present a bDNA assay using UCNPs for the detection of the filamentous bacteriophage M13. Bacteriophages are widespread bacterial viruses that have various biotechnological applications. One of the most commonly used bacteriophages is M13, which infects *Escherichia coli* and contains a circular single-stranded DNA (ssDNA, 6407 bases).[26–28] M13 thus serves as an ideal model analyte for the detection of other ssDNA viruses, such as human parvovirus B19 and human papillomavirus.

Figure 1 shows different configurations that are based on the second-generation bDNA assay. Configuration A involves only capture probes for the immobilization of the target DNA, which is then detected by three subsequent hybridization steps ((1) label extender, (2) preamplifier probe, and *3) amplification probe), and the final binding of streptavidin-modified UCNPs as detection labels. This detection scheme was gradually extended: configuration B involves two instead of one label extenders per preamplifier and configuration C target capture via capture extenders. The branched assay structure leads to a strong signal amplification because many UCNPs bind per target DNA molecule. Furthermore, the UCNP labels can be directly detected on the surface of the microtiter plate, avoiding another substrate incubation step, which is necessary for enzyme labels.

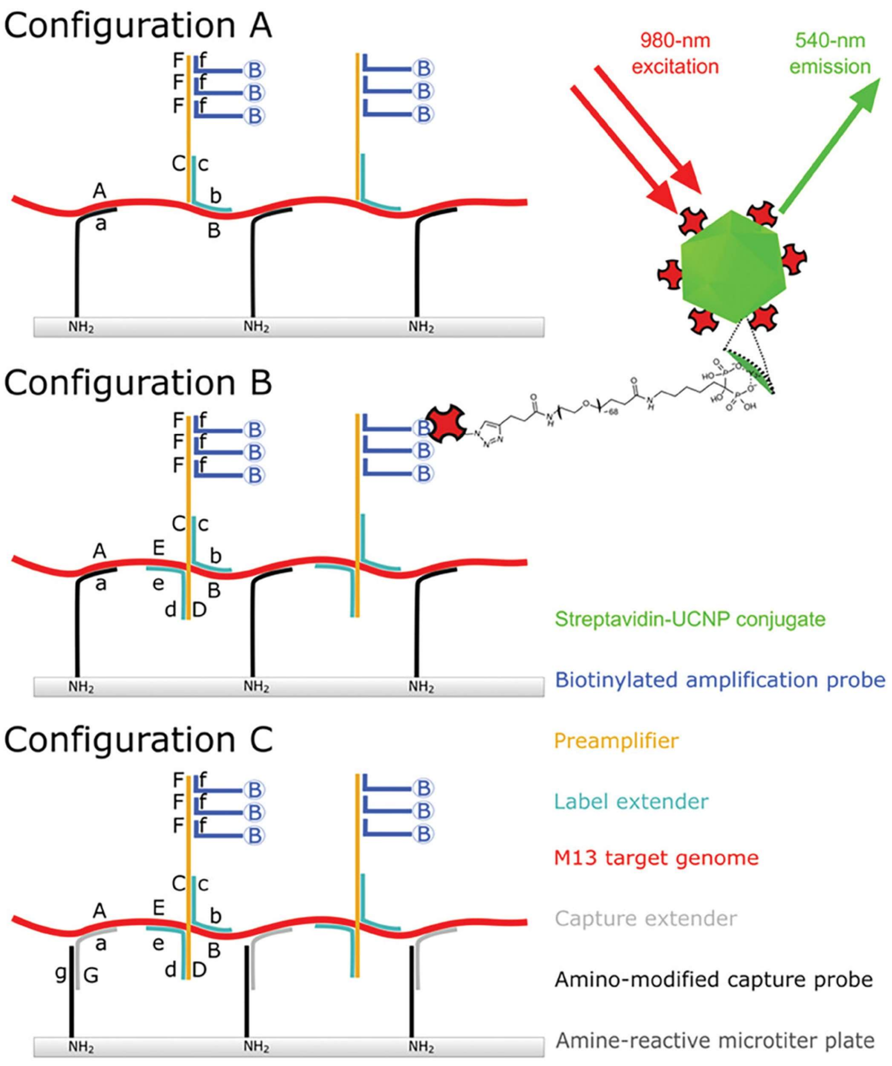

Figure 1. *Configurations of branched DNA assay: Configuration A) target capture via capture probe and a single label extender per preamplifier. Configuration B) target capture via capture probe and two label extenders per preamplifier. Configuration C) target capture via capture extender hybridizing to capture probe and two label extenders per preamplifier. Letter pairs A-a, B-b etc. indicate complementary sequences and each letter stands for a specific sequence.*

8.3 Materials and methods

8.3.1 Materials and buffers

DNA oligonucleotides were obtained from Integrated DNA Technologies (Coralville, IA, USA). Upon arrival, the lyophilized oligonucleotides were resuspended to a concentration of 100 µM in TE buffer (10 mM Tris, 0.1 mM EDTA, pH 7.5) and stored at 4°C. All oligonucleotide sequences are listed in the Supporting Information (SI). Polyethylene glycol, MW 3000, (PEG_{3000}) was from Carl Roth, Germany. SuperBlock in TBS and microtiter plates (Nunc Immobilizer Amino) were purchased from Thermo Fisher (Waltham, MA, USA). Kaivogen wash solution was obtained from Uniogen Oy (Turku, Finland). Core/shell UCNPs ($NaYF_4$: 18% Yb, 2% Er/$NaYF_4$, 58 nm in diameter) were synthesized, characterized and the UCNPs were further surface modified with click reactive streptavidin (SA-PEG-UCNPs) as described in our previous work and the SI (**Fig. S1**).[24] The conjugation of the Eu chelate to streptavidin is described in the SI. *Escherichia coli* XL-1 blue cells and VCS M13 phage were obtained from Agilent Technologies (Santa Clara, CA, USA).

All buffers were prepared using double-distilled water filtered through a 0.22-µm membrane (Magna Nylon, GVS, Zola Predosa, Italy) followed by sterilization *via* a steam autoclave. Buffers used in this work included phosphate-buffered saline (PBS; 50 mM NaH_2PO_4/Na_2HPO_4, 150 mM NaCl, pH 8.0), phosphate-buffered saline containing a higher salt concentration to promote DNA hybridization (hPBS; 50 mM NaH_2PO_4/Na_2HPO_4, 300 mM NaCl, pH 7.4), modified Kaivogen wash buffer (Kaivogen wash solution modified with 300 mM NaCl, 1 mM KF, and 0.1% (w/v) Tween 20), and blocking buffer (Kaivogen wash buffer modified with 2% (v/v) of ethanolamine). DELFIA enhancement solution was obtained from Revvity (Waltham, MA, USA).

8.3.2 Production of M13 phage

The phage stock (VCS M13) was prepared by amplifying the phage in *Escherichia coli*. First, *E. coli* XL-1 blue cells were inoculated from a glycerol preparation into 20 mL of SB medium (30 g/L tryptone, 20 g/L yeast extract, 10 g/L MOPS, pH 7.0) with 10 mg/L tetracycline, 0.2% glucose, and incubated at 37 °C (300 rpm shaking) until the optical density at 600 nm (OD_{600}) reached 0.4–0.6. Then, a 10-fold excess of VCS M13 phage was added to infect the cell culture. The culture was shaken and the incubation at 37 °C was continued for 30 min without shaking. The infected culture (20 mL) was then divided into six flasks, each containing 250 mL of prewarmed SB medium with 10 mg/L tetracycline and 0.2% glucose. After 1 h of incubation (37 °C, 300 rpm shaking) kanamycin was added to a final concentration of 70 µg/mL to select for the phagemid VCS M13. The culture was grown for 3 h at 37 °C under shaking (300 rpm) and then additionally for 15 h at 30 °C under the same shaking conditions.

The next day, the bacterial cells were collected by centrifugation (10,000g, 20 min, 4°C) and the phage-containing supernatant was transferred to new tubes. One sixth volume of 20% PEG_{8000} (Thermo Fisher, Waltham, MA, USA) in 2.5 M NaCl was added to the supernatant, and the phage was precipitated in a water-ice bath for 2 h. After centrifugation (10,000 *g*, 20 min, 4°C), the supernatant was carefully removed, and the resulting precipitated phage pellets were resuspended in 50 mL of TBS (50 mM Tris base, pH 7.5; 150 mM NaCl). The phage suspensions of three tubes were combined, followed by centrifugation (10,000 *g*, 20 min, 4°C) and transferring the supernatants to new tubes. For the second precipitation step, one sixth of the volume of PEG/NaCl was again added, and the suspension was incubated on ice for 15 min followed by centrifugation (10,000 *g*, 20 min, 4°C). The supernatant was discarded, and the pellet was resuspended in 10 mL of TSA/BSA (TBS with 1% (w/v) BSA and 0.02% (w/v) NaN_3) and transferred to new tube. After centrifugation (16,000 *g*, 5 min, 4°C) the supernatant was transferred to a new tube and the phage stock was stored at 4°C. *E. coli* cells infected with VCS M13 phage that confers antibiotic resistance were plated on selective agar (antibiotic selection). The colony forming units (cfu) of infected cells were counted according to Sambrook *et al.*[29] to determine the concentration of the phage stock solution.

8.3.3 Selection of oligonucleotide probes

Integrated DNA Technologies provided the OligoAnalyzer Tool for the design of oligonucleotide probes regarding melting temperatures, hybridization energies and the formation of hairpin structures, self and hetero dimers. To ensure none of the probes bind to other targets, in particular the genome of the M13 host organism

Escherichia coli, all sequences were run through BLAST using the blastn suite (https://blast.ncbi.nlm.nih.gov/Blast.cgi; National Library of Medicine, Bethesda, MD, USA).

8.3.4 bDNA assay

Configuration A: A 96-well microtiter plate (Nunc immobilizer amino, Thermo Fisher) was coated for 1 h at room temperature (RT) with 40 µL of amine-modified capture probes (0.1 µM each, probes *1–6*; Table 2) in PBS according to the manufacturer's instructions. The plate was washed twice with 200 µL of modified Kaivogen wash buffer, blocked for 1 h with 150 µL of blocking buffer, and again washed twice. Serial dilutions of bacteriophage M13 were prepared in microtubes containing hPBS and label extender probes (0.1 µM each; probes *13-16*), and lysed for 5 min at 95°C under shaking in a thermomixer. After the lysis, the samples were cooled to RT using a thermomixer, and 100 µL of each sample was added to the wells and incubated for 1 h under shaking at RT. After two washing steps, either the biotinylated preamplifier (probe *29,* 0.4 µM) in hPBS (100 µL) or a mixture of preamplifier (probe *25;* 0.2 µM) and amplification probe (probe *28*, 0.8 µM) in hPBS (100 µL) were added for 1 h. The microtiter plate was washed twice, and SA-PEG-UCNPs (100 µL, 6.5 µg/mL) in hPBS were added and incubated for 1 h. The plate was then washed twice and left to dry before the readout.

Configuration B: The Nunc immobilizer amino microtiter plate was coated for 1 h at RT with 40 µL of amine-modified capture probes (0.1 µM each, probes *1–6*; Table 2) in PBS. The plate was washed twice with 200 µL of modified Kaivogen wash buffer, blocked for 1 h with 150 µL of blocking buffer, and again washed twice. Serial dilutions of bacteriophage M13 were prepared in microtubes containing hPBS and two sets of label extenders (probes *13-16* and *17-20*; 0.1 µM each). After lysis at 95°C for 5 min under shaking, the samples were cooled to RT, and 100 µL of each sample was added to the wells and incubated for 1 h under shaking at RT. The microtiter plate was washed twice and incubated for 1 h with 100 µL of a mixture of preamplifier probe (0.2 µM, probe *26*) and amplification probe (0.8 µM, probe *28*) in hPBS at RT. The preamplifier (probe *26*) contained an additional sequence for the binding for the second set of label extenders. The microtiter plate was washed twice, and SA-PEG-UCNPs (100 µL, 6.5 µg/mL) in hPBS were added and incubated for 1 h. The plate was then washed twice and left to dry before the readout.

Configuration C: The Nunc immobilizer amino microtiter plate was coated with an amine-modified capture probe (probe *30*, 0.5 µM in 40 µL PBS). After two washing steps the plate was blocked for 1 h with 150 µL of blocking buffer and washed again twice. Serial dilutions of bacteriophage M13 were prepared in microtubes containing hPBS (with 1% (w/v) PEG_{3000})*, capture extender (probes *7–12*, 0.1 µM each) and two sets of label extender (probes *13-16* and *17-20*; 0.1 µM each). After lysis at 95°C for 5 min under shaking, the samples were cooled to RT, and 100 µL of each sample was added to the wells and incubated for 1 h under shaking at RT. After two washing steps, either a mixture of preamplifier (probe *26;* 0.2 µM) and amplification probe (probe *28*, 0.8 µM) in hPBS (with 1% (w/v) PEG_{3000})* or the biotinylated preamplifier (probe *29,* 0.4 µM) in hPBS (with 1% (w/v) PEG_{3000})* were added. Both preamplifier probes contained an additional sequence for the binding for the second set of label extender. The microtiter plate was washed twice, and SA-PEG-UCNPs (100 µL, 6.5 µg/mL) in hPBS were added and incubated for 1 h. The plate was then washed twice and left to dry before the readout.

*PEG_{3000} was added only in the final optimized protocol.

Reference assay: The reference was conducted as described for configuration C, but the SA-PEG-UCNP label was replaced by an SA-Eu label (100 µL, 1.5 nM). After the preamplifier/amplification probes and two washing steps, 100 µL of the SA-Eu label (1.5 nM) in hPBS was added and incubated for 1h at RT. After two washing steps, 100 µL of DELFIA enhancement solution was added and incubated for 15 min under shaking.

8.3.5 Luminescence readout and data analysis

A multi-mode microtiter plate reader (UPCON S-Pro, Labrox, Turku, Finland) served for the readout of upconversion luminescence and time-resolved fluorescence.

Upconversion luminescence (UCL): Er-doped UCNPs were excited by a 976-nm laser (dichroic mirror cut-on: 950 nm) and the emission was recorded using a 540 ± 30 nm emission filter. Each well was raster-scanned in an 8 × 8 matrix with a step size of 300 µm between the spots and a signal integration time of 0.5 s. The truncated average of the signal intensity for each well was calculated by discarding the 8 highest and the 8 lowest values.

Time-resolved fluorescence (TRF): The Eu chelate was excited by a xenon flash lamp using a 340 ± 40 nm excitation filter, and after a delay time of 400 µs, the emission was recorded for 400 µs using a 616 ± 4.25 nm emission filter.

For data regression (Origin 2021, OriginLab, Northampton, MA USA), average signals and standard deviations from three independent wells were determined, and a four-parameter logistic function was applied to the data:

$$Y = \frac{Y_{\mathrm{max}} - Y_{\mathrm{bg}}}{1 + \left(\frac{[\mathrm{Target}]}{\mathrm{EC}_{50}}\right)^{s}} + Y_{\mathrm{bg}}$$

where [Target] is the target concentration, Y the UCL or TRF, respectively, Y_{max} the maximum signal and Y_{bg} the background signal. The EC_{50} value is the target concentration that reduces Y_{max} - Y_{bg} by 50% and s is the slope at the inflection point of the fitted curve. The limits of detection (LODs) were calculated by adding three times the standard deviation of the blank to the baseline of the regression curve.

8.4 Results and discussion

8.4.1 Selection of oligonucleotides for the detection of bacteriophage M13

We combined a second-generation bDNA assay with an upconversion readout for the detection of bacteriophage M13 as a model analyte. Oligonucleotide probes were designed to allow for a substantial degree of freedom in the optimization of the assay setup. First, the OligoAnalyzer Tool was used to screen the genomic single-stranded DNA of the phage for appropriate capture sequences minimizing nonspecific hybridization and hairpin formation.

Sequences for target capture were designed to be 16-20 nucleotides long with similar melting temperatures in the range of 60-68°C. Six capture sequences were selected to enable an efficient capture of the target DNA. Based on these sequences the capture probes *1-6* (**Table 2**) were designed with the terminal amino group coupled via a C_6-linker for immobilizing to the microtiter well plate. Furthermore, four label extenders (probes *13-16,* length of 16-19 nucleotides) were designed to bind simultaneously to different sites of the phage genome (**Fig. 2**) and thus amplifying the detection. With a consensus binding site, all four label extenders hybridized to a preamplifier (probe *25*), which also included three repeating sequences complementary to the amplification probe. Thus, up to three molecules of the biotinylated amplification probe (probe *28*) hybridized to one molecule of preamplifier (probe *25*, *26* or *27*, respectively). The amplification probe contained a long (72 nucleotides) random sequence as a spacer to prevent steric hindrance during the final binding step of UCNP labels. To highlight the difference to the first-generation bDNA assay, we also designed a biotinylated version of the preamplifier (probe *29*) that was directly detectable by streptavidin-coated UCNPs.

For assay configuration B, label extenders from configuration A (probes *13*-*16*) were combined with a second set of label extenders (probes *17-20*) specifically designed to bind to an elongated preamplifier (probe *26*) in a cross junction (**Fig. 1** B and C), which increases the specificity and stability of the preamplifier probe. Another set of label extenders (probes *21-24)* was designed similarly as probes *17-20*, but binding with a distance of four nucleotides to the first set of label extender (probes *13*-*16*) on the target genome. To compensate for the four nucleotides replaced by the spacer (TTTT) between the sequence hybridizing to the target and the one hybridizing to the preamplifier, label extenders were elongated by four target-complementary nucleotides at the 3’ end. In this way, we aimed for the same hybridization efficiency and for increasing the binding flexibility to the preamplifier (probe *27*). The label extenders with TTTT spacer bind to the target DNA and the preamplifier with a distance of eight nucleotides.

For assay configuration C, a different capture probe (probe *30*) was used for the hybridization of a capture extender (probes *7-12*). The combination of a capture probe with a capture extender allowed more freedom in target binding due to an increased distance to the solid surface resulting in less steric hindrance. Moreover, the capture extender can hybridize freely to the target in solution prior to hybridizing to the capture probe immobilized on the solid surface.[30]

The combination of multiple capture and label extender probes ensured a highly specific detection of the target genome. Four target sequences were selected on the target genome for the label extenders and each preamplifier contained three binding sites for the biotinylated amplification probes with a long spacer to minimize steric hindrance. This branched assay design achieved a signal amplification effect by binding up to 12 UCNP labels for each target genome.

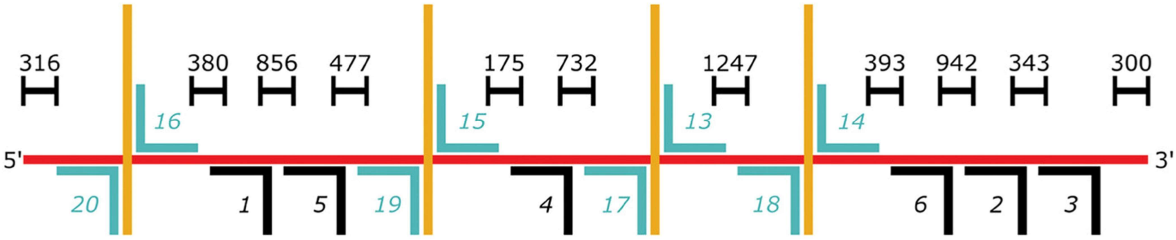

***Figure 2**. Schematic overview of the hybridization sites of label extender (blue) and capture (extender) (black) to the M13 target genome (red). Numbers between the different hybridization sites indicate the distance given in number of nucleotides. Numbers in italics indicate the oligonucleotide probes, whose sequences are provided in the SI.*

8.4.2 Implementation of the bDNA assay configurations A and B

Six amine-modified capture probes (probes *1-6*) were immobilized on an amine-reactive microtiter plate. We chose small coating volumes of 40 µL per well to increase the density of the capture probe and immobilize the target DNA only on the bottom of the well surface. The detection of the target DNA was first established without the branched amplification system using only four label extenders (probes *13-16*), a biotinylated preamplifier (probe *29*) and streptavidin-UCNP label, which resulted in an LOD of 1.9×10^8 cfu/mL and a relatively high background signal of 3961 CPS (**Fig 3**. blue curve). The complete (branched) detection system of four label extenders, preamplifier (probe *25*), amplification probe (probe 28) and streptavidin-UCNP label improved the LOD 13-fold to 1.5×10^7 cfu/mL and strongly reduced the background signal below 1000 CPS (**Fig. 3**, black curve).

Configuration B was designed to improve the binding strength of the detection system to the target DNA: Each of the four label extenders (probes 13-16) was supplemented by a second label extender (probes 17-20), which resulted in a cross junction between the target DNA, a set of two label extenders and an elongated preamplifier (probe 26). Although the detection system included again the amplification probes, the overall signal at higher concentrations (10^9 cfu/mL) was two orders of magnitude lower ($8×10^3$ CPS) compared to configuration A ($1×10^6$ CPS). The higher number of label extender probes involved in configuration B may not allow all probes to access the target DNA for specific hybridization reactions. Consequently, also the LOD ($2.1×10^8$ cfu/mL, **Fig. 3**, red curve) was 14-fold higher than in configuration A. The very low background signal of less than 1000 CPS indicates that nonspecific hybridization events or binding of the UCNP label to the microtiter plate surface did not affect the assay performance.

The overall low assay performance of configurations A and B may be a consequence of a limited accessibility of detection oligonucleotides and UCNP label because the target DNA is located too closely to the microtiter plate surface. This leads to a crowded environment on the surface of the microtiter plate.

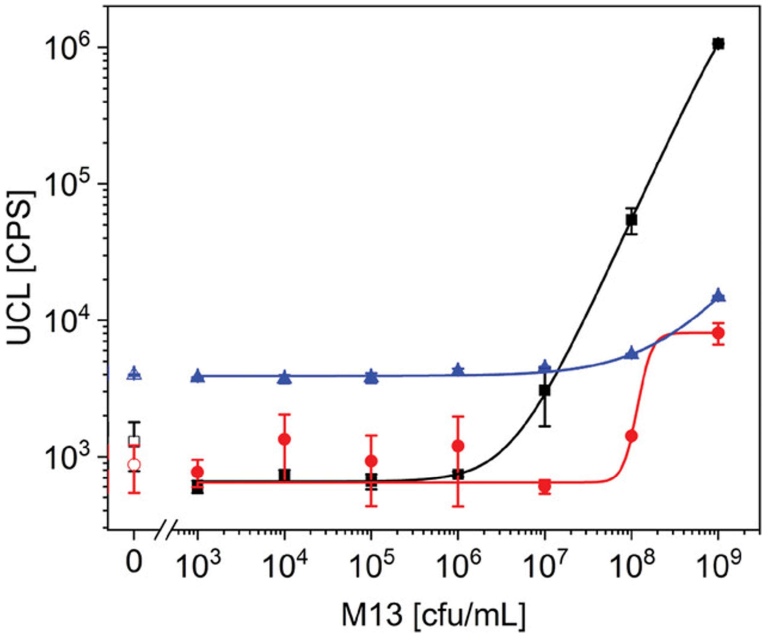

Figure 3. Calibration curves of the bDNA assays using different detection modes. Blue triangles: configuration A with biotinylated preamplifier probes (LOD: $1.9×10^8$ cfu/mL), black squares: configuration A with preamplifier and biotinylated amplification probes (LOD: $1.5×10^7$ cfu/mL), and red circles: configuration B with preamplifier and biotinylated amplification probes (LOD: $2.1×10^8$ cfu/mL). The error bars represent the standard deviations of three replicate measurements.

8.4.3 Final assay configuration C

For configuration C, the direct capture of the target DNA by the capture probe was replaced by a two-step hybridization process. Initially, an amine-reactive microtiter plate well was coated with an amine-modified capture probe (probe *30*), which subsequently hybridized to the capture extender binding the target sequence (probes *7-12*). In the detection system, again a set of two label extender probes hybridized to a single preamplifier probe as in configuration B. But here we additionally tested two different label extender designs (1) without spacer between the oligonucleotide sequence binding to the target DNA and the preamplifier and (2) with a short spacer of four oligonucleotides (TTTT) between these two hybridization regions. The spacer may potentially reduce steric hindrance and improve the binding efficiency due to its higher flexibility. **Figure 4**, however, shows that the spacer in the label extenders also increased the background signal, which indicates a higher degree of nonspecific hybridization to capture probes and/or label extenders. This phenomenon may occur if two shorter oligonucleotides rather than a single longer oligonucleotide bind with higher energy due to π-π-stacking.[31] The higher background also led to a relatively high LOD of 9.8×10^6 cfu/mL. By contrast, without a spacer, the LOD of 2.5×10^5 cfu/mL was 60 times lower (**Fig. 4**, black curve) as compared to configuration A.

When the label extenders including the TTTT spacer were combined with the biotinylated preamplifier (**Fig. 4**, blue curve), the background signal was the highest of all tested combinations. Thus, the nonspecific hybridization effects of the TTTT spacer in the label extenders and the biotinylated preamplifier seem to add up. Additionally, the overall signals were lower and the LOD was only 3.1×10^7 cfu/mL. Therefore, all subsequent experiments were carried out using configuration C and label extenders without spacer.

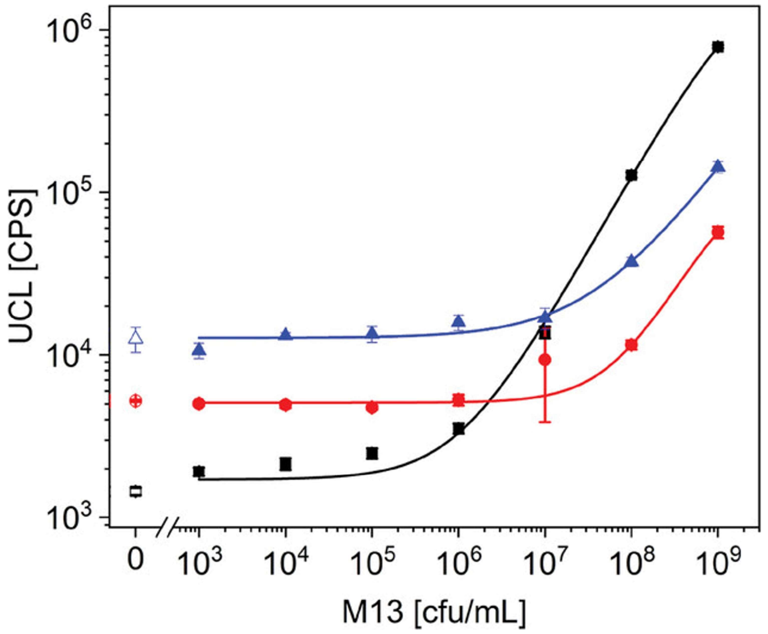

Figure 4. *Calibration curves of assay configuration C. Black squares: with label extenders (no spacer), preamplifier and biotinylated amplification probes (LOD: 2.5×10^5 cfu/mL), red circles: with label extenders (with TTTT spacer), preamplifier and biotinylated amplification probes (LOD: 9.8×10^6 cfu/mL), and blue triangles: with label extenders (with TTTT spacer) and biotinylated preamplifiers (LOD: 3.1×10^7 cfu/mL). The error bars represent the standard deviations of three replicate measurements.*

8.4.4 Influence of assay buffers

The assay sensitivity is not only limited by the assay design, the specific binding of DNA oligomers, and the labeling, but also by the degree of non-specific binding and the buffer selection. Lahtinen et al.[32] have previously shown that the addition of polymers such as polyethylene glycol (PEG) and polyacrylic acid (PAA) improves the sensitivity of immunoassays. PEG may prevent nonspecific binding and also act as a crowding agent, which reduces the available volume for oligonucleotides and thereby increases the rate of specific hybridization.[33–35] Therefore, we added PEG_{3000} to the buffers in different steps of the bDNA assay to test its effect on the assay performance (**Fig. 5, Table 1**). Unexpectedly, the background signal was highest when PEG was added in all assay steps and decreased with less incubation steps containing PEG.

In our previous immunoassay experiments, Kaivogen was buffer supplemented with 10% SuperBlock efficiently prevented nonspecific binding of UCNPs to the microtiter plate.[24] This effect was also observable in the bDNA assay, because nonspecific binding decreased by nearly 20% (**Fig. 5**, green curve).

Additionally, (weakly bound) nonspecifically hybridized oligonucleotides likely dissociated during the incubation in Kaivogen wash buffer/SuperBlock without PEG during the incubation of the UCNP label and subsequent washing steps, which reduced nonspecific binding while maintaining (strongly bound) specifically hybridized oligonucleotides.

The LOD of 1.1×10^5 cfu/mL obtained with Kaivogen wash buffer/SuperBlock was, however, worse compared to the incubation when PEG was only added to the target DNA and the preamplifier/amplification probe and the UCNP label was only incubated in hPBS without PEG (red curve, LOD: 5.9×10^4 cfu/mL). To further reduce the background, the incubation temperatures, number of washing steps and the temperature of wash buffer was varied. This had, however, only marginal effects on the assay performance. Consequently, all subsequent assays were carried out with these buffer combinations at RT and with two washing steps after each incubation step.

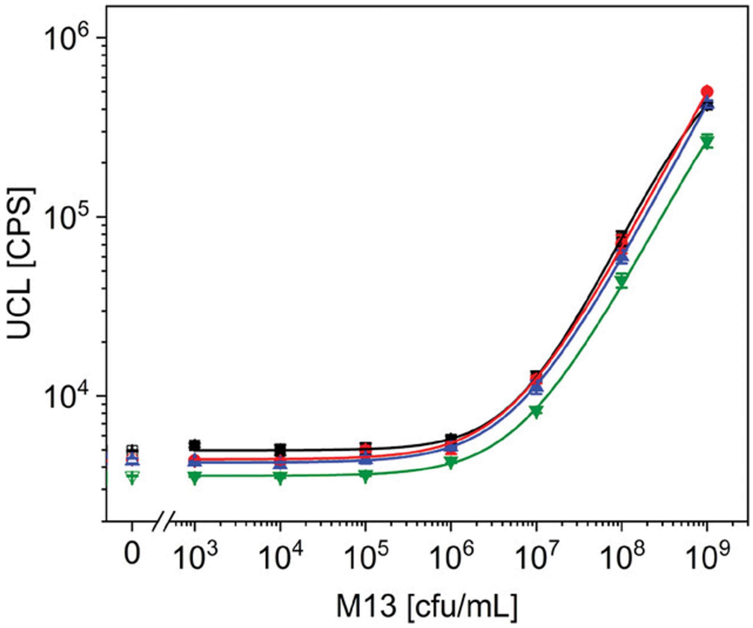

Figure 5. *Influence of the combination of assay buffers (shown in* ***Table 1****) on configuration C of the bDNA assay. The error bars represent the standard deviations of three replicate measurements.*

Table 2: *Variation of the buffer combination used for the optimization shown in Figure 4.*

Assay setup	**Incubation step**			Background signal [CPS]	LOD [cfu/mL]
	Target DNA	Preamplifier and amplification probe	UCNP label		
Black curve	hPBS + 1% (w/v) PEG	hPBS + 1% (w/v) PEG	hPBS + 1% (w/v) PEG	4938	3.2×10^5
Red curve	hPBS + 1% (w/v) PEG	hPBS + 1% (w/v) PEG	hPBS	4423	5.9×10^4
Blue curve	hPBS + 1% (w/v) PEG	hPBS	hPBS	4337	8.3×10^6
Green curve	hPBS + 1% (w/v) PEG	hPBS	Modified Kaivogen wash buffer + 10% SuperBlock	3559	1.1×10^5

8.4.5 Optimal assay parameters, reference assay and cross reactivity

The optimized detection protocol for configuration 3 (**Fig. 6,** black curve), involving the amplification probe as a representative of second-generation bDNA assays, was compared to the detection using only the biotinylated preamplifier (**Fig. 6,** blue curve, similar as the first-generation bDNA assay) and a reference assay based on time-resolved detection of Eu chelates (**Fig. 6**, red curve). The amplification probes in combination with UCNP labels increased the signal intensity at the highest target concentration tested almost fourfold (5.0×10^5 CPS vs. 1.4×10^4 CPS). Even more important, the LOD increased over 500-fold because the biotinylated preamplification probes again led to a high nonspecific hybridization and a high background signal, which obscures the assay response at lower concentrations.

By contrast, the reference assay involving preamplifier, amplification probe and Eu chelate resulted in a very low background signal, indicating that nonspecific binding was in general not a problem when the amplification probes were used. The overall signal of the reference assay, however, was also relatively low leading to an LOD of only 1.25×10^7 cfu/mL. Consequently, the second-generation bDNA assay in combination with UCNP labels strongly improved the LOD in comparison to the time-resolved readout or other DNA hybridization assays using lanthanide luminescence (**Table 2**).

Finally, the cross reactivity was tested using a non-target genome from an unrelated bacteriophage (**SI, Fig. S2**). The cross-reactivity of the non-target genome was only 1% as compared to the M13 target genome, and there was only a weak signal increase at very high non-target DNA concentrations (>10^{10} cfu/mL).

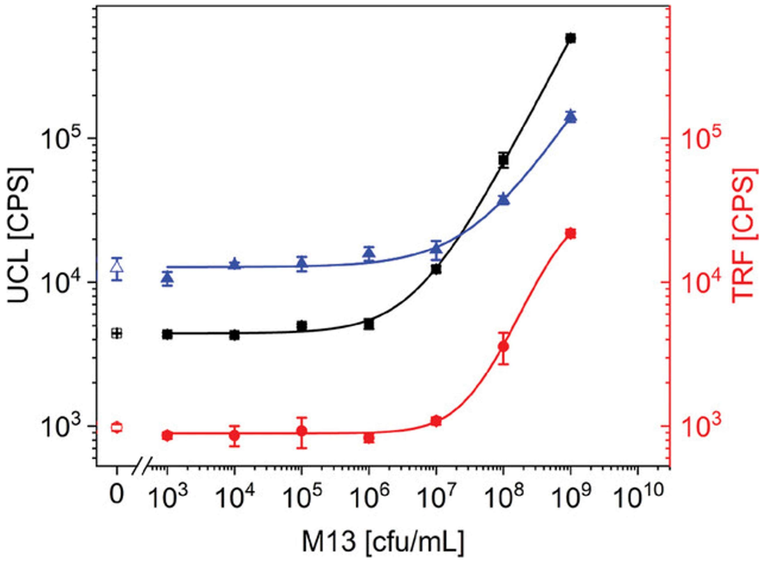

Figure 6. *Calibration curves obtained with the optimized bDNA assay (configuration C) using preamplifier and amplification probe (black squares LOD 5.9 × 10^4 cfu/mL) or biotinylated preamplifier (blue triangles, LOD 3.1×10^7 cfu/mL) in comparison to the reference assay using streptavidin-labeled Eu-chelates (red circles, LOD 1.25×10^7 cfu/mL).*

Table 2: *Comparison of DNA hybridization assays and immunoassays for the detection of M13 bacteriophage.*

Method	**Detection labels**	**LOD**	**Reference**
Hybridization assay (bDNA)	UCNPs	5.9×10^4 cfu/mL	This work
Hybridization assay (bDNA)	Eu chelates	1.25×10^7 cfu/mL	This work
Hybridization assay	Switchable lanthanide fluorescence	1.14×10^9 cfu/mL	[36]
Lateral flow immunoassay	Gold nanoparticles	5.0×10^7 *pfu/mL**	[37]
Capillary immunoassay	Enzyme-catalyzed chemiluminescence	5.0×10^5 *pfu/mL**	[38]

*Plaque-forming units

8.5 Conclusions

In this work, we have combined the second-generation bDNA assay using a branched amplification probe and UCNP label for the detection of the M13 bacteriophage. Choosing a wide genomic range of the target sequence for the capture extender decreased the assay susceptibility toward mutations as compared to or immunoassays or PCR. Unlike target amplification based on PCR, the amplification of the signal enables a more quantitative detection.

As in our previous works on immunoassays, the UCNP labels strongly improved the LOD to 5.9×10^4 cfu/mL, which is an almost 20,000-fold improvement over previously reported DNA hybridization assays. The background signal was very low as compared to the first-generation bDNA assay that we simulated by using a biotinylated amplifier. The low background signal can be explained by a very low degree of non-specific hybridization reactions. Consequently, there was no need to proceed to the third-generation bDNA assay, which involves more expensive non-natural nucleotides to reduce nonspecific hybridization. Furthermore, the bDNA assay is easily adaptable to other target DNAs/RNAs by only adjusting the part of the oligonucleotide sequences of label extenders and capture extenders that bind to the target.

Acknowledgments

This work was supported by grant NU22-05-00042 from the Ministry of Health of the Czech Republic. We thank Antonín Hlaváček from the Institute of Analytical Chemistry of the Czech Academy of Sciences in Brno for providing UCNPs, Tuomas Huovinen from the Department of Life Technologies at the University of Turku for preparing the M13 phage stocks, and Ivana Mašlaňová from the Department of Experimental Biology at Masaryk University for providing the phage phi812K1/420.

8.6 References

1. W. R. de Araujo, H. Lukas, M. D. T. Torres, W. Gao, C. de La Fuente-Nunez, *ACS Nano* 2024, 18, 1757.
2. A. Cassedy, A. Parle-McDermott, R. O'Kennedy, *Front. Mol. Biosci*. 2021, 8, 637559.
3. M. M. El-Daly, *Diagnostics* 2024, 14, 519.
4. M. J. C. van den Beld, J.-L. Murk, J. Kluytmans, M. P. G. Koopmans, J. Reimerink, I. H. M. van Loo, M. C. A. Wegdam-Blans, H. Zaaijer, C. GeurtsvanKessel, C. Reusken, *Journal of Clinical Microbiology* 2021, 59, e0076721.

5. A. Cassedy, A. Parle-McDermott, R. O'Kennedy, *Front. Mol. Biosci*. 2021, 8, 637559.

6. J. Lee, J.-U. Song, S. R. Shim, Journal of clinical virology the official publication of the Pan American Society for Clinical Virology 2021, 144, 104985.

7. G. J. Tsongalis, *Am J Clin Pathol* 2006, 126, 448.

8. D. L. Wiedbrauk, D. H. Farkas (Eds.), Molecular methods for virus detection, Academic Press, San Diego 1995.

9. M. L. Collins, B. Irvine, D. Tyner, E. Fine, C. Zayati, C. Chang, T. Horn, D. Ahle, J. Detmer, L. P. Shen, J. Kolberg, S. Bushnell, M. S. Urdea, D. D. Ho, Nucleic Acids Res 1997, 25, 2979.

10. MyBioSource Learning Center, Branched DNA (bDNA) Technology - MyBioSource Learning Center 2023, https://www.mybiosource.com/learn/branched-dna-bdna-technology/.

11. M. Sidstedt, P. Rådström, J. Hedman, Anal Bioanal Chem 2020, 412, 2009.

12. M. Urdea, L. Wuestehube, in Nonradioactive Analysis of Biomolecules, Springer Berlin Heidelberg. Berlin, Heidelberg 2000, p. 388.

13. J. C. Wilber, M. S. Urdea, in Molecular methods for virus detection (Eds.: D. L. Wiedbrauk, D. H. Farkas), Academic Press. San Diego 1995, p. 131.

14. K. Sun, X. Wang, Y. Qu, H. Wang, J. Cheng, *Analytical Chemistry* 2023, 95, 13605.

15. J. Detmer, R. Lagier, J. Flynn, C. Zayati, J. Kolberg, M. Collins, M. Urdea, R. Sánchez-Pescador, Journal of clinical microbiology 1996, 34, 901.

16. R. S. Ross, S. Viazov, S. Sarr, S. Hoffmann, A. Kramer, M. Roggendorf, *Journal of virological methods* 2002, 101, 159.

17. DiaCarta, Inc., isobDNA™ isoC-isoG Branched DNA Technology 2023, https://www.diacarta.com/technology/isobdna.

18. Y. Li, X. Qi, C. Lei, Q. Yue, S. Zhang, *Chemical communications* (Cambridge, England) 2014, 50, 9907.

19. E. Harris, J. Detmer, J. Dungan, F. Doua, T. White, J. A. Kolberg, M. S. Urdea, N. Agabian, *Journal of clinical microbiology* 1996, 34, 2401.

20. J. C. Brandmeier, K. Raiko, Z. Farka, R. Peltomaa, M. J. Mickert, A. Hlaváček, P. Skládal, T. Soukka, H. H. Gorris, *Advanced Healthcare Materials* 2021, 10, e2100506.

21. U. Resch-Genger, H. H. Gorris, *Anal Bioanal Chem* 2017, 409, 5855.

22. H. H. Gorris, U. Resch-Genger, *Anal Bioanal Chem* 2017, 409, 5875.

23. [C. Chen, C. Li, Z. Shi, *Advanced Science* 2016, 3, 1600029.

24. J. C. Brandmeier, N. Jurga, T. Grzyb, A. Hlaváček, R. Obořilová, P. Skládal, Z. Farka, H. H. Gorris, *Analytical Chemistry* 2023, 95, 4753.

25. F. van de Rijke, H. Zijlmans, S. Li, T. Vail, A. K. Raap, R. S. Niedbala, H. J. Tanke, *Nat Biotechnol* 2001, 19, 273.

26. R. Peltomaa, E. Benito-Peña, R. Barderas, M. C. Moreno-Bondi, *ACS Omega* 2019, 4, 11569.

27. J. W. Kehoe, B. K. Kay, *Chemical Reviews* 2005, 105, 4056.

28. Elizabeth Kutter, in Practical Handbook of Microbiology, CRC Press 2008, p. 733.

29. Molecular cloning: a laboratory manual 1989.

30. S. P. Tsai, A. Wong, E. Mai, P. Chan, G. Mausisa, M. Vasser, P. Jhurani, M. H. Jakobsen, W. L. T. Wong, J.-P. Stephan, *Nucleic Acids Res* 2003, 31, e25.

31. P. Yakovchuk, E. Protozanova, M. D. Frank-Kamenetskii, *Nucleic Acids Res* 2006, 34, 564.

32. S. Lahtinen, A. Lyytikäinen, N. Sirkka, H. Päkkilä, T. Soukka, *Microchim Acta* 2018, 185, 220.

33. L. E. Baltierra-Jasso, M. J. Morten, L. Laflör, S. D. Quinn, S. W. Magennis, *Journal of the American Chemical Society* 2015, 137, 16020.

34. R. M. Amasino, *Analytical Biochemistry* 1986, 152, 304.

35. S. Nakano, H. Karimata, T. Ohmichi, J. Kawakami, N. Sugimoto, *Journal of the American Chemical Society* 2004, 126, 14330.

36. A. Lehmusvuori, J. Manninen, T. Huovinen, T. Soukka, U. Lamminmäki, *BioTechniques* 2012, 53, 301.

37. F. Mashayekhi, R. Y. T. Chiu, A. M. Le, F. C. Chao, B. M. Wu, D. T. Kamei, *Anal Bioanal Chem* 2010, 398, 2955.

38. E. Yacoub-George, W. Hell, L. Meixner, F. Wenninger, K. Bock, P. Lindner, H. Wolf, T. Kloth, K. A. Feller, *Biosensors and Bioelectronics* 2007, 22, 1368.

8.7 Supporting Information

8.7.1 Preparation of streptavidin-UCNP labels

Core / shell UCNPs ($NaYF_4$: 18% Yb, 2% Er / $NaYF_4$, 58 nm in diameter) were synthesized using a high temperature coprecipitation method and the same batch of UCNPs as in our previous work was used (Brandmeier *et al*. 2023). The synthesis of alkyne-PEG-neridronate and the preparation of SA-PEG-UCNP conjugates was carried out as described earlier (Brandmeier et al. 2023) with the only exception that THPTA was added during the copper catalyzed click-reaction.

8.7.1.1 Synthesis of alkyne-PEG-neridronate

First, 30 mg of neridronate (Merck, Darmstadt, Germany) was dissolved in a mixture of 898 µL of PB (50 mM, pH 7.4) and 128 µL of 1 M NaOH under sonication. Then, 75 mg of Alkyne-PEG-NHS (α-N-hydroxysuccinimide-ω-alkyne polyethylene glycol, MW 3000; Iris Biotech, Marktredwitz, Germany) was added and incubated overnight at 4 °C. The reaction mixture was dialyzed against 4 L of double-distilled water in a Float-A-Lyzer G2 dialysis device (500–1000 Da M_W cut-off; Fisher Scientific, Germany) at 4 °C for 96 hours; water was exchanged 12 times. The purified, colorless Alkyne-PEG-neridronate was lyophilized (Alpha 1-2, Christ, Osterode am Harz, Germany) and stored at 4 °C.

8.7.1.2 Preparation of streptavidin-PEG-UCNP conjugates

For the preparation of SA-PEG-UCNP labels, 10 mg (311 µL) of UCNPs dispersed in cyclohexane were mixed with the same volume of 200 mM aqueous HCl and incubated for 30 min at 38 °C under shaking. The solution was then sonicated for 15 min to remove oleic acid from the UCNP surface and mediate a phase transfer from cyclohexane to water. The lower HCl phase was taken and added to an approximately twofold excess of acetone, which led to the precipitation of UCNPs. After centrifugation at 1,000 *g* for 20 min, the UCNP pellet was redispersed in 500 µL of water and sonicated for 5 min. Then, 2 mg of the linker dissolved in 500 µL of water were added and shaken overnight at 38 °C. Excess linker was removed by dialysis of the UCNP conjugates in a Float-A-Lyzer G2 dialysis device (100 kDa M_W cut-off; Fisher Scientific, Waltham, MA, USA) for 72 h at 4 °C against 4 L of 1 mM KF in water, which was exchanged nine times.

The UCNP conjugates were functionalized with streptavidin using a click reaction. Tris-HCl (375 mM, pH 7.5; 100 µL) and an aqueous solution of 25 mM $CuSO_4$ and 125 mM THPTA (10 µL) were added to 10 mg of alkyne-PEG-neridronate UCNPs dispersed in 1.4 mL of water. After purging the mixture for 45 min with argon, 100 µL of streptavidin azide (1 mg/mL) were added, and the mixture was purged for another 10 min. The click reaction was started by adding 20 µL of 100 mM sodium ascorbate in water. The dispersion was purged for 40 min with argon and then dialyzed for 72 h at 4 °C in a Float-A-Lyzer G2 dialysis device (100 kDa M_W cut-off) against 4 L of dialysis buffer (50 mM Tris, 0.05% NaN_3, 1 mM KF, pH 7.5), which was exchanged nine times.

8.7.2 Characterization of UCNP labels

UCNPs were characterized by transmission electron microscopy (TEM) on a Titan Themis electron microscope (FEI, Czech Republic) and dynamic light scattering (DLS) on a Zetasizer Nano (Malvern, UK) (**Figure S1**). Compared to the original DLS measurement of 87 nm (Brandmeier *et al*. 2023, red curve), the hydrodynamic diameter of the SA-PEG-UCNP conjugates increased only slightly to 90 nm (blue curve), which confirms their long-term stability of the over a period of almost two years.

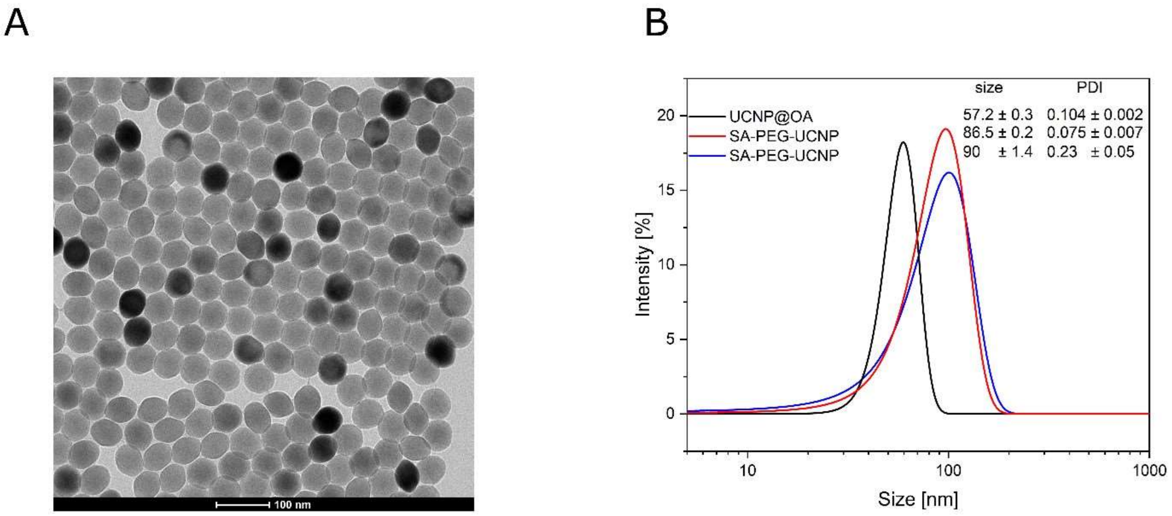

***Figure S1:** Characterization of UCNPs and their conjugates. (A) TEM image of oleic acid-capped UCNPs and (B) DLS of oleic acid-capped UCNPs (black curve), and SA-PEG-UCNPs shortly after conjugation (red curve) and remeasured after 22 months (blue curve).*

8.7.3 Reference

1. Brandmeier, JC, Jurga, N, Grzyb T, Hlaváček A, Obořilová R, Skládal P, Farka Z, Gorris HH (2023): Digital and Analog Detection of SARS-CoV-2 Nucleocapsid Protein via an Upconversion-Linked Immunosorbent Assay. *Analytical Chemistry* 95 (10) 4753–4759.

8.7.4 Cross-reactivity study

The cross-reactivity was tested with bacteriophage phi812K1/420 from the family of *Myoviridae* (containing double-stranded DNA) using assay configuration C under optimal lysis and assay conditions (**Figure S2**). At a phage concentration of 1×10^9 cfu/mL the targe genome of M13 yielded a signal of 606482 UCL and the non-target genome phi812K1 a signal of only 6188 UCL, which is in the range of the assay background. The cross-reactivity was only 1%. Even though there is a small assay response at very high concentrations of non-target DNA (>10^{10} cfu/mL), the overall UCL remains very low as compared to the target DNA.

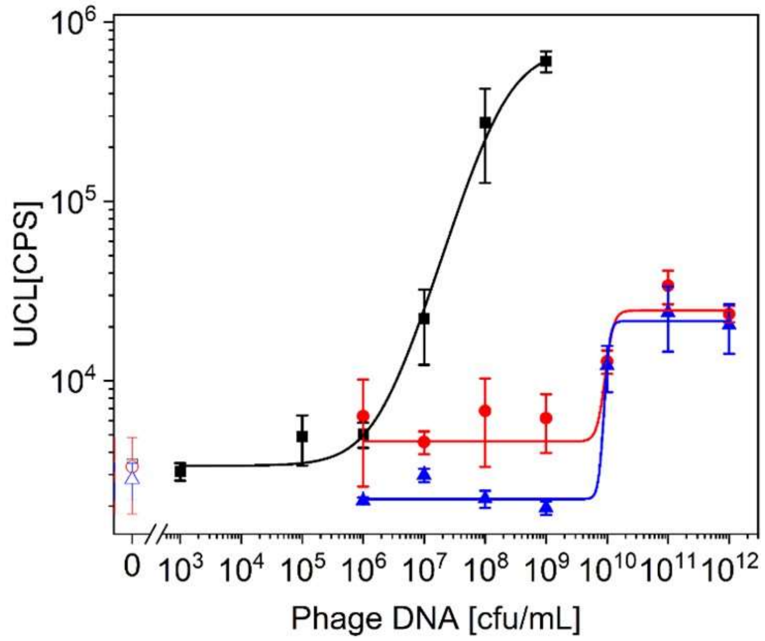

Figure S2: *Calibration curves of target phage M13 and non-target phage phi812K1 using configuration C of the bDNA assay. Black squares: detection of target phage M13. Red curve: detection of non-target phage phi812K1 using preamplifier and biotinylated amplification probes. Blue curve: detection of non-target phage phi812K1 using biotinylated preamplifier. The error bars represent the standard deviations of three replicate measurements.*

8.7.5 Preparation of Eu-labeled streptavidin

Streptavidin was labeled with a 50-fold molar excess of europium(III) chelate of N^1-(p-isothiocyanatobenzyl)diethylenetriamine-N^1, N^2, N^3, N^3-tetraacetic acid (University of Turku, Finland). The labeling reaction (45 µM streptavidin and 2.25 mM chelate in 50 mM sodium carbonate buffer (pH 9.3), was incubated overnight at 4 °C. The labeled streptavidin was purified *via* 6 times centrifugation (14,000 g, 20 min) using Amicon ultra centrifugal filters (30 kDa M_W cut-off; Merck, Darmstadt, Germany), transferred to 50 mM Tris-HCl, 150 mM NaCl, pH 7.75 and stored at 4 °C.

8.7.6 List of oligonucleotide probes

Probe	**Sequence 5’ → 3’**
Capture probe version A and C	
1	NH$_2$-C6-AACAACATTATTACAGGT
2	NH$_2$-C6-ACCGTCTATCAGGGCGA
3	NH$_2$-C6-TATTTTTGAGAGGTCTAC
4	NH$_2$-C6-ACCACCCTCAGAGCCGCC
5	NH$_2$-C6-TAGAAAGGAACAACTA
6	NH$_2$-C6-TAGAAAGGAATTGAGG
Capture extender version B	
7	AACAACATTATTACAGGTTTTTATCGAACCCCTATCTCTAC
8	ACCGTCTATCAGGGCGATTTTATCGAACCCCTATCTCTAC
9	TATTTTTGAGAGGTCTACTTTTATCGAACCCCTATCTCTAC
10	ACCACCCTCAGAGCCGCCTTTTATCGAACCCCTATCTCTAC
11	TAGAAAGGAACAACTATTTTATCGAACCCCTATCTCTAC
12	TAGAAAGGAATTGAGGTTTTATCGAACCCCTATCTCTA
Label extender version A	
13	TTAGACGGGAGAATTAACTTTTCATACGCGCGACGATACGGC
14	TTTTACATCGGGAGAAACTTTTCATACGCGCGACGATACGGC
15	TACTGGTAATAAGTTTTATTTTCATACGCGCGACGATACGGC
16	ATCGCGTTTTAATTCGAGTTTTCATACGCGCGACGATACGGC
Label extender version B without spacer	
17	CGGACTTCGGACGGACTGAACACCCTGAACAA
18	CGGACTTCGGACGGACAATAACGGATTCGCCTGAT
19	CGGACTTCGGACGGACACGGGGTCAGTGCCTTGA
20	CGGACTTCGGACGGACCTTCAAAGCGAACCAGAC
Label extender version B with spacer	
21	CGGACTTCGGACGGACTTTTCACCCTGAACAAAGTC
22	CGGACTTCGGACGGACTTTTACGGATTCGCCTGATTGCT
23	CGGACTTCGGACGGACTTTTGGTCAGTGCCTTGAGTAA
24	CGGACTTCGGACGGACTTTTAAAGCGAACCAGACCGGA
Preamplifier	
25	AGGTGCCGGGATCCCTGTTGCTTTAGGTGCCGGGATCCCTGTTGCTTTAGGTGCCGGGATCCCTGTTGCTTTGCCGTATCGTCGCGCGTATG
26	AGGTGCCGGGATCCCTGTTGCTTTAGGTGCCGGGATCCCTGTTGCTTTAGGTGCCGGGATCCCTGTTGCTTTGCCGTATCGTCGCGCGTATGGTCCGTCCGAAGTCCG
27	AGGTGCCGGGATCCCTGTTGCTTTAGGTGCCGGGATCCCTGTTGCTTTAGGTGCCGGGATCCCTGTTGCTTTGCCGTATCGTCGCGCGTATGTTTTGTCCGTCCGAAGTCCG
Amplification probes	
28	GCAACAGGGATCCCGGCACCTTTTCGTGAACCATGCCGCGACTGATTTCGTGAACCATGCCGCGACTGATTTCGTGAACCATGCCGCGACTGA-biotin
Biotinylated preamplifier	
29	Biotin-AGGTGCCGGGATCCCTGTTGCTTTAGGTGCCGGGATCCCTGTTGCTTTAGGTGCCGGGATCCCTGTTGCTTTGCCGTATCGTCGCGCGTATGTTTTGTCCGTCCGAAGTCCG
Capture probe version B	
30	NH$_2$-C6-GTAGAGATAGGGGTTCGAT

9 Summary and conclusions

The main focus of this thesis lies on the use of photon upconversion nanoparticles (UCNPs) as labels in bioaffinity assays. UCNPs are inorganic nanoparticles with unique optical properties compared to other optical labels such as quantum dots or fluorophores. Under near infrared (NIR) excitation UCNPs absorb two or more photons and emit a photon of shorter wavelength (higher energy), so called anti-Stokes emission. The excitation under NIR light has several advantages, such as the drastic reduction in background signal due to autofluorescence and reduced light scattering. Another advantage of UCNPs is their high photostability, constant emission and low toxicity which makes them ideal labels for a wide variety of bioanalytical applications. The lack of background signal is particularly beneficial for digital readout methods.

The first part of this thesis describes the fundamentals of bio-assays with particular focus on different assay setups and readout methods explained. This is followed by a discussion of various biorecognition elements and introduction of the most important label types. The introduction part concludes with an overview of UCNPs, detailing the upconversion mechanism and emphasizing the surface modification of UCNPs. The second part of this thesis contains three original publications made during the PhD time.

The first research article focuses on the effect of surface chemistry and particle size on the assay sensitivity. Cardiac troponin I was selected as highly relevant biomarker for the early detection of myocardial infarction using a sandwich ULISA format with two capture and two detection antibodies. Two different UCNP surface modifications were tested using either PEG or PAA. Coating the UCNPs with alkyne-PEG-neridronate was followed by a modification with click reactive streptavidin-azide and the use of biotinylated detection antibodies in the assay. The PAA-coated UCNPs, on the other hand, were used and further modified with detection antibodies using EDC/NHS chemistry while biotinylated capture antibodies were immobilized on streptavidin coated microtiterplate. Furthermore, for PAA modified UCNPs the influence of nanoparticle size on assay performance was evaluated. For all tested UCNP surface modifications and sizes, the assay readout was performed in the analogue (using a microtiterplate reader) and the digital (with the upconversion microscope) mode. The particle size and surface modification of the used labels had much larger influence than the readout method. With the optimal surface modification and particle size, PAA coated UCNPs (48 nm in size) an LOD of 10 pg/mL of cTnI in human plasma, for both readout methods was achieved.

The second article concentrates on the analogue and digital detection of SARS-CoV-2 nucleocapsid protein (N protein) using an upconversion linked immunosorbent assay. The N protein was selected due to its abundance and low rate of mutation, making it the optimal target antigen. In this work, we employed UCNPs modified with SA-PEG in combination with biotinylated detection antibodies in a conventional 2+2 sandwich assay format. We investigated the influence of the readout method and antibody selection on the assay sensitivity. The selection of capture and detection antibodies had a significant influence on assay performance, improving the assay sensitivity nearly 100-fold, and with the optimal antibody combination, an LOD of 1.4 pg/mL for the detection of the recombinant N protein was achieved. By changing from the analogue to the digital readout method no changes in assay sensitivity were observed for the detection of the recombinant N protein while the digital redout improved the detection of SARS-CoV-2 in virus lysate by a factor of 10 (0.8 $TCID_{50}$/mL analogue and 0.08 $TCID_{50}$/mL digital). This observation supports our previous hypothesis that a high antibody affinity is needed before the digital readout can further improve the assay sensitivity.

The third research article focuses on the development of a highly sensitive assay for pathogen detection using bacteriophage M13 as a model analyte. To combine the simplicity of nucleic acid hybridization assays with the sensitivity amplification-based assays, we developed an upconversion branched DNA (bDNA) hybridization assay. The signal amplification stems from a series of oligonucleotide probes hybridizing in a branched structure with several hybridization sites for biotinylated amplification probes binding up to twelve SA-PEG modified UCNPs to a single target sequence. Different generations of bDNA assays and configurations were tested to achieve the best assay sensitivity. A setup similar to the second-generation assay, using branched amplification probes paired with label and capture extenders to minimize steric hindrance achieved a LOD of 5.9 × 10^4 CFU/mL. The assay susceptibility towards mutations of the target genome was reduced by selecting a wide genomic range for the capture probes and extenders. Furthermore, compared to assays based on target amplification, such as PCR, the bDNA assay enables quantitative detection and is more robust regarding complex sample matrices. By exchanging the capture probes the presented upconversion-linked bDNA assay can be easily adapted to other target DNAs.

Overall, the work conducted in this thesis showed that UCNPs are highly versatile labels for sensitive bio-assays. The wide range of target analyte sizes, from nucleic acids to viral particles, demonstrated the applicability of UNCPs in different assay setups. Furthermore, the digital readout methods proved its potential to increase the assay sensitivity drastically, although it was also seen to be limited by the antibody affinity and particle brightness. Further improvements could be achieved with smaller and brighter particles and a better understanding of their behaviour in different assay formats. Nevertheless, further research is essential to fully harness the exceptional properties of UCNPs for real-world applications and improved diagnostics.

10 Zusammenfassung und Fazit

Der Fokus dieser Arbeit liegt auf der Verwendung von Photonen-Aufkonvertierenden Nanopartikeln (UCNPs) als Marker in Bioaffinitätsassays. UCNPs sind anorganische Nanopartikel mit einzigartigen optischen Eigenschaften im Vergleich zu anderen optischen Markern wie Quantenpunkten oder Fluorophoren. Unter Nahinfrarot-Anregung (NIR) absorbieren UCNPs zwei oder mehr Photonen und emittieren ein Photon kürzerer Wellenlänge (höhere Energie), sogenannte Anti-Stokes-Emission. Die Anregung durch NIR-Licht bietet mehrere Vorteile, wie die drastische Reduzierung des Hintergrundsignals aufgrund von Autofluoreszenz und verringerter Lichtstreuung. Ein weiterer Vorteil von UCNPs ist ihre hohe Photostabilität, konstante Emission und geringe Toxizität, was sie zu idealen Markern für eine Vielzahl bioanalytischer Anwendungen macht. Insbesondere das Fehlen von Hintergrundsignalen macht sie zu einem idealen Marker für digitale Auslesemethoden.

Im ersten Teil dieser Arbeit werden die Grundlagen und allgemeinen Prinzipien von Bioanalytischen-Assays erklärt. Zunächst werden verschiedene Assay-Aufbauten zusammen mit zwei unterschiedlichen Auslesemethoden beschrieben. Darauf folgt eine Diskussion über eine Vielzahl von Bioerkennungselementen, und die wichtigsten Markertypen werden vorgestellt. Der Einleitungsteil schließt mit einem Überblick über UCNPs und dem Aufkonvertierungs-Mechanismus ab, wobei ein besonderer Fokus auf die Oberflächenmodifikation von UCNPs gelegt wird. Der zweite Teil dieser Arbeit umfasst drei Originalpublikationen, die während der Promotionszeit entstanden sind.

Der erste Forschungsartikel konzentriert sich auf den Effekt der Oberflächenmodifikation und der Partikelgröße auf die Assay Sensitivität. Kardiales Troponin I wurde als hochrelevanter Biomarker für die Früherkennung von Myokardinfarkten ausgewählt. Hierbei wurde das Sandwhich-ULISA-Format mit zwei Fänger- und zwei Detektionsantikörpern verwendet. Zwei verschiedene UCNP-Oberflächenmodifikationen wurden getestet. Die erste bestand darin, die

UCNPs mit Alkin-PEG-Neridronat zu beschichten und anschließend mit klick-reaktiven Streptavidin-Azid zu modifizieren. Hierbei wurden biotinylierte Detektionsantikörper verwendet. Bei der zweiten Oberflächenmodifikation wurden PAA-beschichtete UCNPs verwendet und mit Detektionsantikörpern unter Verwendung von EDC/NHS-Chemie modifiziert. Bei Verwendung dieser Antikörper-PAA-UCNP Konjugaten wurden die Fängerantikörper biotinyliert und auf einer streptavidin-beschichteten Mikrotiterplatte immobilisiert. Zudem wurden bei PAA-modifizierten UCNPs der Einfluss der Partikelgröße auf die Assay-Leistung untersucht. Für alle getesteten UCNP-Oberflächenmodifikationen und -Größen wurde die Assayauslesung sowohl im analogen (über Mikrotiterplattenleser) als auch im digitalen (über Aufkonversions-Mikroskop) Modus durchgeführt. Die Partikelgröße und Oberflächenmodifikation der verwendeten Marker hatten einen weitaus größeren Einfluss auf die Assay Sensitivität als die Auslesemethode. Mit der optimalen Oberflächenmodifikation und Partikelgröße wurde eine Nachweisgrenze (LOD) von 10 pg/mL cTnI im menschlichen Plasma für beide Auslesemethoden erreicht.

Der zweite Artikel konzentriert sich auf den analogen und digitalen Nachweis des SARS-CoV-2-Nukleokapsidproteins (N-Protein) unter Verwendung eines Aufkonversions-gekoppelten Immunosorbens-Assays. Das N-Protein wurde aufgrund seiner Häufigkeit und der niedrigen Mutationsrate als optimales Zielantigen ausgewählt. In dieser Arbeit wurden UCNPs modifiziert mit SA-PEG in Kombination mit biotinylierten Detektionsantikörpern im herkömmlichen 2+2-Sandwich-Assay-Format eingesetzt. Wir untersuchten den Einfluss der Auslesemethode und der Antikörperauswahl auf die Assay Sensitivität. Die richtige Auswahl der Fänger- und Detektionsantikörper zeigte einen signifikanten Einfluss auf die Assayleistung und verbesserte die Sensitivität des Assays um fast das 100-fache. Mit der optimalen Antikörperkombination wurde eine Nachweisgrenze von 1,4 pg/mL für den Nachweis des rekombinanten N-Proteins erreicht. Durch den Wechsel von der analogen zur digitalen Auslesemethode wurden keine Änderungen der Assaysensitivität für den Nachweis des rekombinanten N-Proteins beobachtet, während die digitale Auslesung die Detektion von SARS-CoV-2 im Virenlysat um das Zehnfache verbesserte (0,8 TCID50/mL analog und 0,08 TCID50/mL digital).

Diese Beobachtung stützt unsere vorherige Hypothese, dass eine hohe Antikörperaffinität erforderlich ist, bevor die digitale Auslesung die Assay Sensitivität weiter verbessern kann.

Der dritte Forschungsartikel konzentriert sich auf die Entwicklung eines hochempfindlichen Assays zum Pathogennachweis unter Verwendung von Bakteriophage M13 als Modellanalyten. Um die Einfachheit von Nukleinsäure-Hybridisierungsassays mit der Sensitivität von amplifikationsbasierten Assays zu kombinieren, entwickelten wir einen Aufkonversions-basierten, verzweigten DNA (bDNA)-Hybridisierungsassay. Die Signalverstärkung resultiert aus einer Reihe von Oligonukleotidsonden, die sich in einer verzweigten Struktur mit mehreren Hybridisierungsstellen für biotinylierte Amplifikationssonden hybridisieren. Diese verzweigten biotinylierten Amplifikationssonden können bis zu 12 SA-PEG-modifizierte UCNPs an eine einzelne Zielsequenz binden. Verschiedene Generationen von bDNA-Assays und Konfigurationen wurden getestet, um die beste Assay Sensitivität zu erreichen. Ein Setup, das dem Assay der zweiten Generation ähnelt, bei dem verzweigte Amplifikationssonden mit Label- und Fängerextendern gepaart wurden, um sterische Hinderungen zu minimieren, erreichte eine Nachweisgrenze von 5,9 × 10^4 CFU/mL. Die Anfälligkeit der Assays gegenüber Mutationen des Zielgenoms wurde durch die Auswahl eines breiten genomischen Bereichs für die Fängersonden und Extender reduziert. Im Vergleich zu Assays basierend auf Amplifikation der Ziel-DNA, wie z. B. PCR, ermöglicht der bDNA-Assay eine quantitative Detektion und ist robuster gegenüber komplexen Probenmatrizes. Durch den Austausch der Fängersonden kann der präsentierte Upconversion-verknüpfte bDNA-Assay leicht an andere Ziel-DNAs angepasst werden.

Insgesamt zeigt die in dieser Arbeit durchgeführte Forschung, dass UCNPs höchst vielseitige Marker für empfindliche Bio-Assays sind. Die breite Vielfalt an Zielanalyten, die von Nukleinsäuren bis hin zu Viruspartikeln reicht, demonstriert die Anwendbarkeit von UNCPs in verschiedenen Assay-Aufbauten. Darüber hinaus hat sich die digitale Auslesung als potenziell äußerst wirksam zur Erhöhung der Assay Sensitivität, jedoch auch als stark eingeschränkt durch die Antikörperaffinität und Partikelhelligkeit erwiesen. Weitere Verbesserungen könnten möglicherweise durch kleinere und hellere Partikel sowie ein besseres Verständnis ihres Verhaltens in verschiedenen Assay-Formaten erreicht werden. Nichtsdestotrotz ist weitere Forschung entscheidend, um das volle Potenzial der außergewöhnlichen Eigenschaften von UCNPs für reale Anwendungen und bessere Diagnostik zu erschließen.

11 Acknowledgements

First and foremost, I want to express my deepest gratitude to my supervisor Assoc. Prof. Dr. Hans-Heiner Gorris. His exceptional support helped me become a better scientist. Furthermore, I want to thank him for the exciting topic and his trust in me during all those years.

Exceptional thanks go to Assoc. Prof. Zdenek Farka whose support and knowledge made many highly sensitive assays only possible. I also want to thank Zdenek for the immense amount of knowledge I gained thanks to him, ranging from handy tricks in Origin to shopping at CEITEC on a Friday afternoon. At last, I want to thank him also for the great time we had at and outside of work and his constant support for me.

I wish to extend my gratitude to Prof. Dr. Petr Skladal, who welcomed us in Brno, helped us improve our publications and supported us throughout the years.

Furthermore, I thank all the amazing and special friends I made during this time. Starting with Eliska Machacova, Dorota Sklenarova and Dr. Natalia Jurga for the great time together in Brno. Wherever we were, at work, the office, fireworks, or buying green balls, it was always fun with you. I also want to thank Carlos Fernandez and all the great time we had during your two stays. Also, special thanks go to Dr. Satu Lahtinen and Prof. Dr. Tero Soukka who supported me during my stay in Turku with their knowledge about the wide range of projects we had running. Additionally, I want to thank Saara Kuusinen who made the stay in Turku and also the last months in Brno fun and who taught me the preparation of polymer nanoparticles.

My sincerest gratitude goes to my family and Riikka who always supported and encouraged me and without whom none of this would have been possible.

12 Eidesstattliche Erklärung

Ich erkläre hiermit an Eides statt, dass ich die vorliegende Arbeit ohne unzulässige Hilfe Dritter und ohne Benutzung anderer als der angegebenen Hilfsmittel angefertigt habe; die aus anderen Quellen direkt oder indirekt übernommenen Daten und Konzepte sind unter Angabe des Literaturzitats gekennzeichnet.

Weitere Personen waren an der inhaltlich-materiellen Herstellung der vorliegenden Arbeit nicht beteiligt. Insbesondere habe ich hierfür nicht die entgeltliche Hilfe eines Promotionsberaters oder anderer Personen in Anspruch genommen. Niemand hat von mir weder unmittelbar noch mittelbar geldwerte Leistungen für Arbeiten erhalten, die im Zusammenhang mit dem Inhalt der vorgelegten Dissertation stehen.

Die Arbeit wurde bisher weder im In- noch im Ausland in gleicher oder ähnlicher Form einer anderen Prüfungsbehörde vorgelegt.

Ort, Datum

Unterschrift